

Beam heat load investigations with a cold vacuum chamber for diagnostics in a synchrotron light source

Zur Erlangung des akademischen Grades eines
DOKTORS DER NATURWISSENSCHAFTEN
von der Fakultät für Physik
des Karlsruher Instituts für Technologie (KIT)

genehmigte

DISSERTATION

von

Dipl.-Phys. Robert Voutta
aus Leipzig

Tag der mündlichen Prüfung: 22.04.2016
Referent: Prof. Dr. Tilo Baumbach
Korreferent: Prof. Dr. Anke-Susanne Müller

Contents

1	Introduction	1
2	Theoretical background	3
2.1	Synchrotron light sources	3
2.1.1	Electron storage rings	3
2.1.2	Sources of synchrotron radiation	4
2.2	Beam heat load sources	9
2.2.1	Synchrotron radiation	9
2.2.2	Longitudinal impedance	11
2.2.3	Electron/Ion bombardment	19
2.3	Network analysis	20
2.3.1	The scattering matrix	20
2.3.2	TEM resonator	21
2.3.3	Loaded and unloaded quality factor	21
2.3.4	Attenuation, impedance and surface resistivity	23
3	Experimental setups	25
3.1	DLS beam parameters and operation modes	25
3.2	A COLD vacuum chamber for DIAGnostics (COLDDIAG)	29
3.2.1	Vacuum layout	29
3.2.2	Cryogenic layout	30
3.2.3	Diagnostics	32
3.2.4	Control for constant liner temperature measurements	35
3.2.5	Offline calibration	37
3.3	Longitudinal wire method for impedance determination	39
3.3.1	Resonator method	39
3.3.2	Vector network analyzer	40
3.3.3	Reference measurements	40
3.3.4	Measurements on COLDDIAG	41

4	Measurements with COLDDIAG at the Diamond Light Source (DLS)	45
4.1	Beam heat load	45
4.1.1	Calibration	45
4.1.2	Measurements	47
4.1.3	Bunch length	48
4.1.4	Bunch spacing and number of bunches	49
4.1.5	Bunch charge	50
4.1.6	Heat load models	52
4.1.7	Liner temperature	53
4.1.8	Warm sections	54
4.2	Pressure	55
4.2.1	Total pressure	55
4.2.2	Gas composition	59
4.2.3	Effect on heat load	63
4.3	Electron and ion bombardment of the chamber walls	66
4.3.1	Total flux	66
4.3.2	Energy spectrum	67
4.3.3	Beam parameters	70
4.3.4	Heat load from low energy electrons	70
4.4	Beam displacement	72
4.5	Temperature distribution on the liner	75
4.5.1	Static temperature distribution at 20 K	75
4.5.2	Static temperature distribution without heaters	77
4.5.3	Dynamic temperature distribution at 20 K	78
4.5.4	Dynamic temperature distribution without heaters	80
4.5.5	Heat transfer simulations	84
4.6	Summary	86
5	Impedance measurements	87
5.1	Reference measurements	90
5.2	COLDDIAG warm part	93
5.3	COLDDIAG cold part and thermal transitions	95
5.4	RF power and beam heat load	100
6	Summary	105
	Bibliography	107

CHAPTER 1

Introduction

The discovery of synchrotron radiation in 1947 [1] has provided a source of high energy X-rays and led to the development of a specific type of particle accelerator, the synchrotron light source. In contrast to particle colliders, where the goal is to create colliding particle beams, synchrotron light sources store the beam (typically electrons) in a closed orbit and produce synchrotron radiation for diffraction, imaging and spectroscopy experiments, when the beam is deflected by a magnetic field. The first synchrotrons only used bending magnets necessary to keep the electrons in a closed orbit to generate synchrotron radiation. In order to reach larger intensities of synchrotron radiation, a more collimated photon beam and higher photon energies modern machines (third generation synchrotron light sources) make use of undulators and wigglers (insertion devices consisting of an array of alternating dipole magnets) between the bending magnets.

The experiments conducted with synchrotron radiation, e.g. in the fields of nanoscience and soft matter physics, put increasing demands on insertion devices. Studying of small structures and time-resolved spectroscopy require insertion devices with high magnetic fields and short period lengths. A well developed and widely used technology is the permanent magnet undulator. But since the technology is already very mature, the room for improvement is limited. An even better performance can be achieved by using superconducting wire for the generation of the magnetic fields. Compared to the state of the art permanent magnet undulators, superconducting undulators can reach higher magnetic fields for a given gap and period length, and provide a photon beam with a higher flux and a larger spectral range. One open issue for the development of superconducting undulators is the cryogenic design and an important input parameter is the beam heat load from the electron beam to the cold vacuum chamber.

A significantly higher beam heat load than expected from theoretical calculations and simulations has been observed in several superconducting insertion devices, including the superconducting wiggler at the MAX-II storage ring at MAX-lab [2], the first superconducting undulator at the Ångströmquelle Karlsruhe (ANKA) [3], the two superconducting

wigglers at the Diamond Light Source (DLS) [4] and more recently the superconducting undulator at the Advanced Photon Source of Argonne National Laboratory [5]. However, these devices were not specifically built for precise beam heat load measurements. For this reason it was decided at ANKA to build a dedicated cold vacuum chamber for beam heat load diagnostics (COLDDIAG). After it has been designed, built and commissioned [6, 7], it was installed at the Diamond Light Source in 2011. Due to a failure in one of the thermal transitions it had to be removed after one week of operation. With an improved design of the thermal transitions a second installation at DLS was possible in August 2012 and measurements were taken for roughly one year. In addition to the beam heat load COLDDIAG can also measure the residual gas content and pressure, as well as the flux and spectrum of low energy charged particles hitting the chamber walls. This allows to investigate several possible beam heat load sources, including geometric and resistive wall impedance, electron/ion bombardment and synchrotron radiation.

A complementary device has been installed in the storage ring of the Shanghai Synchrotron Radiation Facility (SSRF) in 2012 [8]. While COLDDIAG is equipped with a wide range of diagnostic instrumentation, this device has the ability to measure the beam heat load at different vertical vacuum gaps of the beam chamber. First measurements indicate a higher than expected beam heat load, but cryogenic design issues prevent definite conclusions. In this thesis the measurements with COLDDIAG during the second installation at the DLS and a subsequent offline calibration of the beam heat load measurements are presented and a detailed analysis is given. Impedance measurements on the COLDDIAG structure complement the beam heat load measurements and allow further insight. A major challenge is the interaction between several effects from different fields of physics, ranging from thermodynamics and solid-state physics to electrodynamics.

The next chapter gives an overview of the theoretical background relevant to the thesis, namely the basic working principle of synchrotron light sources and insertion devices, possible beam heat load sources in an electron storage ring and some fundamentals about network analysis.

The third chapter deals with the experimental setups. First the beam parameters and operation modes of the DLS are introduced. Then the setup and instrumentation of COLDDIAG, as well as the wire measurement setup for impedance determination are presented.

In the fourth chapter a detailed analysis of the measurements at the Diamond Light Source is carried out, covering beam heat load, pressure, electron/ion bombardment of the chamber walls, beam displacement and temperature distribution.

In chapter five impedance measurements on reference setups and different parts of the COLDDIAG structure are analysed and related to the beam heat load.

The thesis is closed by a summary of the main results obtained by beam heat load and impedance measurements, and by the conclusions that can be drawn from the obtained results for the development of superconducting undulators.

CHAPTER 2

Theoretical background

2.1 Synchrotron light sources

Synchrotron light sources are facilities that produce electromagnetic radiation (synchrotron radiation) by deflecting charged particles at relativistic energies. There are different types of synchrotron light sources, like electron storage rings and free electron lasers; in the scope of this work only electron storage rings are described in the following. More details can be found in the standard textbooks, e.g. [9, 10].

2.1.1 Electron storage rings

The basic working principle of an electron storage ring is shown schematically in Figure 2.1. Electrons generated in an electron gun are accelerated to typically 100 MeV in a linear accelerator and fed into a booster synchrotron, where the energy is ramped up to the injection energy, e.g. 3 GeV. Then the electrons get transferred to the storage ring through injection magnets, which have to be timed precisely to deposit the electrons at predefined places (buckets) in the time structure of the beam. This process is repeated until the nominal beam current is reached.

The stored electrons are kept on a closed orbit by bending magnets (dipoles). Focusing of the electron beam is achieved by quadrupole magnets, and sextupole magnets are used to compensate for focusing errors. The synchrotron radiation used for experiments is produced in the bending magnets and in the straight sections in between, by insertion devices (undulators or wigglers). Since the electrons lose energy when generating synchrotron radiation they have to be accelerated back to the nominal energy. This happens in the RF (radiofrequency) section, where RF cavities create oscillating electromagnetic fields. The frequency of the fields is timed to the bunch structure of the beam in order to accelerate electrons, which are falling behind, and decelerate electrons, which are too far ahead. The

frequency of the RF system determines the minimal distance between two bunches. For example, a RF frequency of 500 MHz leads to a bunch spacing of 2 ns.

During each turn some electrons get lost completely from the beam due to gas scattering and intrabeam scattering, resulting in a decreasing beam current over time. For experiments it is often desirable to have a high and steady intensity of the photon beam. Therefore in most machines a top-up mode is used to inject new electrons in a certain time interval to get the beam current back to its nominal value.

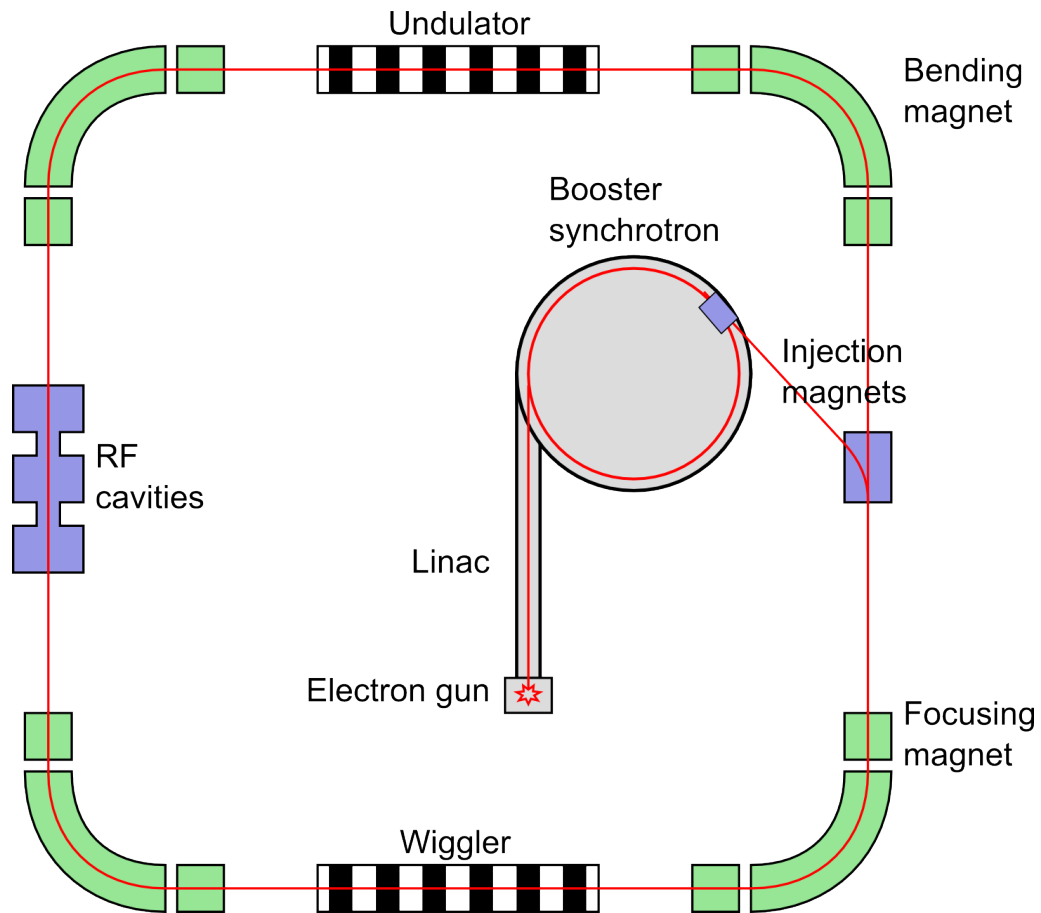


Figure 2.1: Simplified schematic of the main parts of an electron storage ring, including acceleration and injection.

2.1.2 Sources of synchrotron radiation

The purpose of a synchrotron light source is to provide synchrotron radiation to beamlines for experiments using spectroscopy, imaging and diffraction techniques. The different source types, i.e. bending magnets, undulators and wigglers, have unique properties. However their common principle is the radiation profile of a relativistic, charged particle in a transverse magnetic field. This is shown in Figure 2.2 compared to the classic case

of non-relativistic particles. Whereas in the non-relativistic case the angular radiation distribution has the shape of a dipole field, in the relativistic case the emitted radiation is compressed into a cone tangential to the moving direction of the charged particle (in the laboratory frame of reference). The half opening angle of the cone (Ψ in Figure 2.2) gets smaller with increasing velocity and is inversely proportional to the relativistic gamma factor.

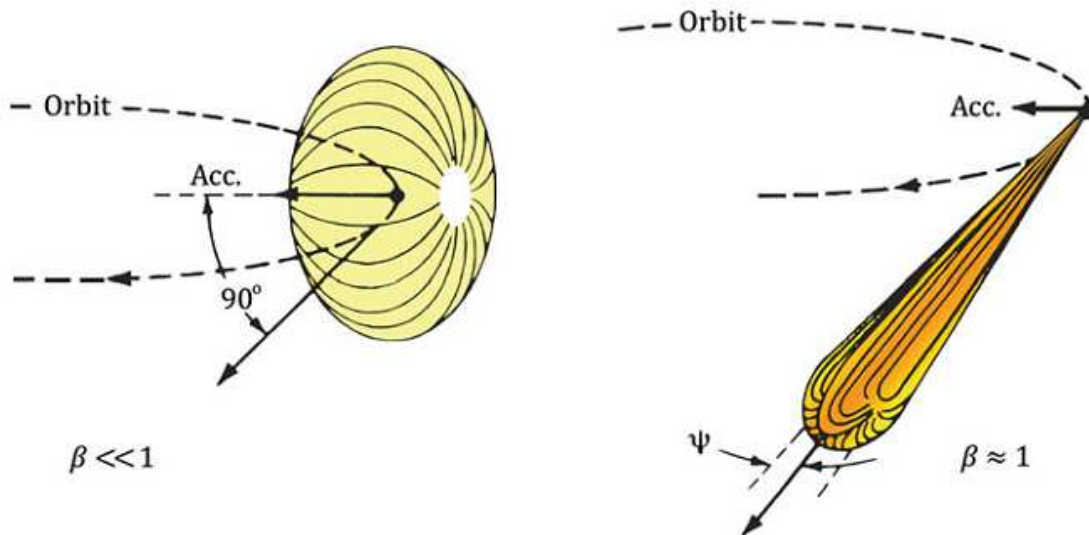


Figure 2.2: Comparison between the radiation profile of a slow ($\beta = v/c \ll 1$) and a relativistic ($\beta = v/c \approx 1$) charge in a magnetic field perpendicular to the moving plane (from [9]).

Bending magnets

In a bending magnet synchrotron radiation is produced along the circular trajectory in the bending arc creating a radiation fan in the horizontal plane (see Figure 2.3). Only a small amount of the radiation fan is used in the beamline for experiments. In the vertical plane the radiation profile is dominated by the beam emittance, i.e. the electron distribution in the phase space for position and momentum, resulting in a much narrower angular distribution.

Insertion devices

In a straight section between two bending magnets an insertion device can be put to create an additional and more powerful source of synchrotron radiation. It consists of consecutive, opposing dipole magnets creating an alternating magnetic field in the vertical direction. When the electron beam passes through the magnetic field it performs an undulating path in the horizontal plane with the period length λ_u (see Figure 2.4). The radiation is generated mainly in the middle of the poles at the peak field and is therefore strongly collimated in the forward direction, resulting in a high brilliance that increases with the

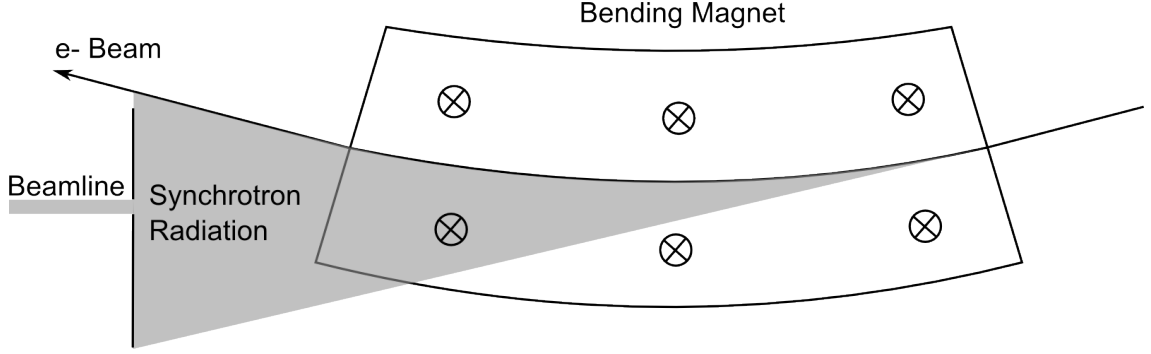


Figure 2.3: Top-down view of the synchrotron radiation fan produced by a bending magnet.

number of poles. The brilliance B of a photon beam emitted by an undulator is defined as:

$$B = \frac{\dot{N}}{4\pi^2 \Sigma_x \Sigma_y \Sigma'_x \Sigma'_y} , \quad (2.1)$$

where \dot{N} is the photon flux in the central cone, Σ_x and Σ_y is the effective horizontal and vertical source size and Σ'_x and Σ'_y is the effective horizontal and vertical divergence [11]. Furthermore the energy distribution of the emitted radiation can be controlled with the intensity of the magnetic field.

If the bending angle α is much larger than the angular divergence of the synchrotron radiation, the insertion device produces an energy spectrum similar to that of a bending magnet and is called wiggler. The photon flux is given by the sum of the flux produced at each pole.

If the bending angle α is similar to the angular divergence of the synchrotron radiation or smaller, the synchrotron radiation from different points along the trajectory interferes constructively for certain energies, strongly increasing the photon flux, and the device is called undulator.

The differentiation between wigglers and undulators is done through the K value, which is the product of α and γ , or for sinusoidal magnetic fields:

$$K = \frac{e}{2\pi m_e c} \lambda_u B , \quad (2.2)$$

where B is the peak magnetic field at the electron trajectory, e is the electron charge, m_e is the electron mass and c is the speed of light. There is a smooth transition between the

undulator regime ($K \leq 1$) and the wiggler regime ($K \gg 1$). Furthermore, the angular divergence of the synchrotron radiation increases with its wavelength, and therefore the transition between undulator and wiggler regime depends on the photon energy, meaning that every wiggler is an undulator below a certain photon energy. The differentiation through the K value only holds true near photon energies, where the angular divergence is approximately $1/\gamma$ [11].

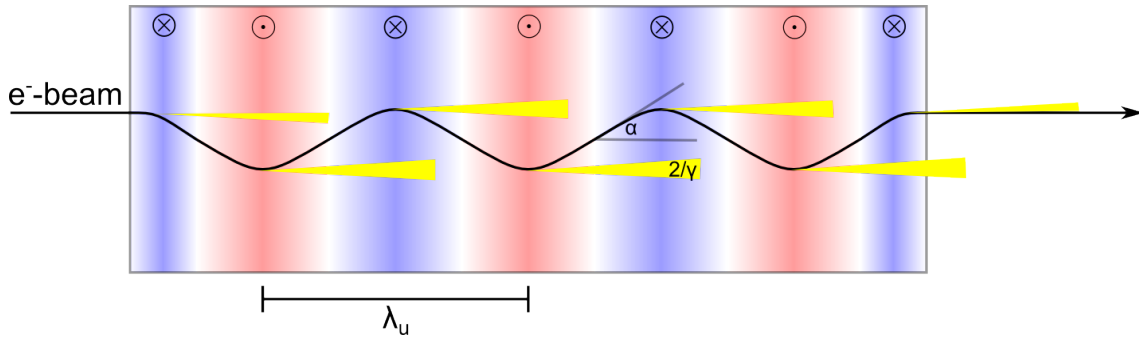


Figure 2.4: Top-down view of an electron beam passing through an insertion device and producing synchrotron radiation.

Comparison of the performance

The different sources of synchrotron radiation vary in performance. Bending magnets, since their main purpose is the deflection of the electron beam, give a limited performance in terms of intensity and flexibility, because they lack the horizontal collimation of insertion devices and their magnetic field strength cannot be varied.

Insertion devices have the principal advantage over bending magnets that the synchrotron radiation is collimated in the horizontal plane due to the alternating magnetic fields, the collimation in undulators being stronger than in wigglers. The intensity scales with the length of the device and is substantially larger for typical device lengths, compared to bending magnets. Moreover a larger maximum photon energy can be achieved by applying higher magnetic fields.

A comparison of the photon spectra from different sources of synchrotron radiation is illustrated in Figure 2.5. While wigglers have the same type of broad photon spectrum as the bending magnets, undulators achieve an enhanced brilliance at specific energies due to constructive interference between the synchrotron radiation emitted from different magnetic poles. The position of these peaks depends on the angle between the undulator axis and the observation axis Θ and can be shifted along the tuning curve (solid red lines) by changing the magnetic field of the undulator. The harmonic wavelengths, at which the constructive interference occurs, are expressed in the undulator equation:

$$\lambda = \frac{\lambda_u}{2\gamma^2} \left(1 + \frac{K^2}{2} + \gamma^2 \Theta^2 \right) \quad (2.3)$$

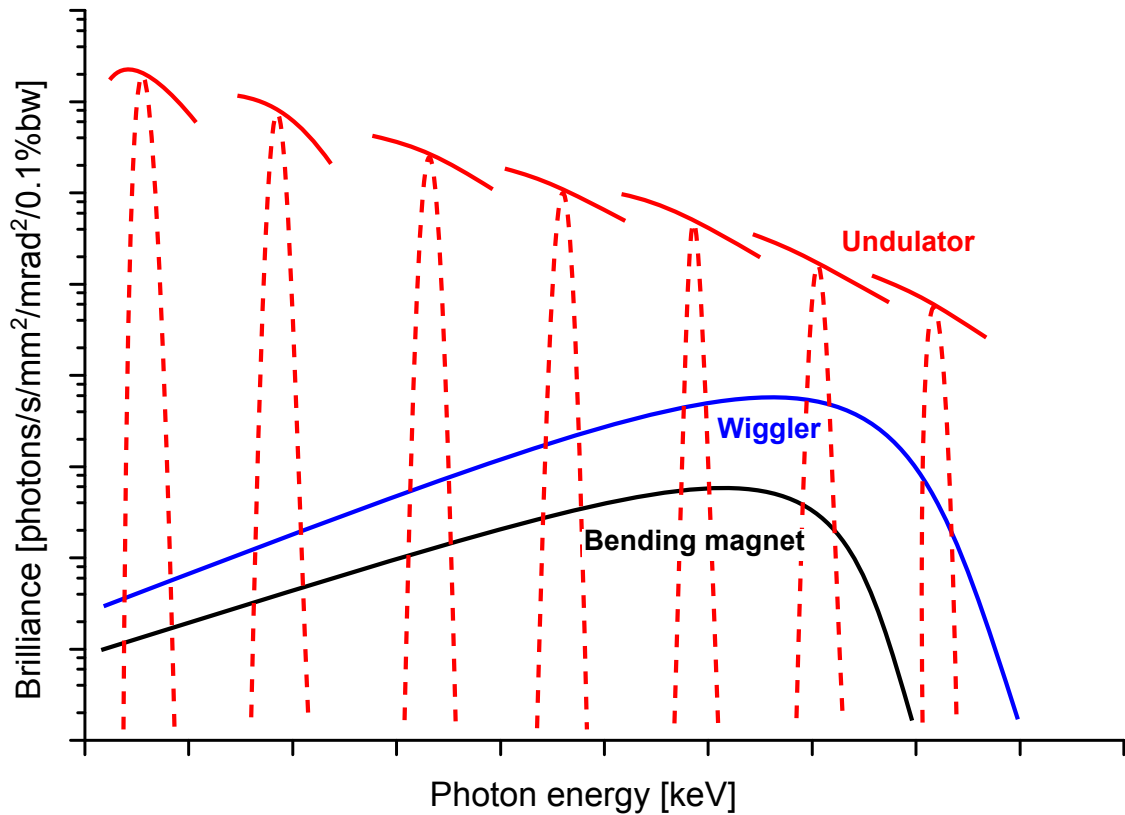


Figure 2.5: Comparison of the photon spectra from bending magnets, wigglers and undulators. The dashed line illustrates a specific undulator spectrum and the solid line its tuning curve, i.e. the dependence of the peak brilliance on the peak magnetic field.

Superconducting undulators

The first undulators for synchrotron light sources used permanent magnets for generating the magnetic field (PMU). This technology is technically mature. New devices are typically in-vacuum to reduce the magnetic gap (IVU). To reach higher peak fields on axis, with the same geometry as for an IVU, the magnets can be cooled to cryogenic temperatures (CPMU).

A further improvement of undulators is possible by switching to superconducting wire for generating the magnetic field. Superconducting undulators (SCU) promise a higher magnetic field for a given gap and period length than it is possible with CPMUs, as well as a higher brilliance and a broader spectral range. Figure 2.6 shows the comparison of the photon beam brilliance as a function of the photon energy between different types of undulators.

One open issue in the development of SCUs is the knowledge of the beam heat load to the cold vacuum chamber, which is needed for the cryogenic design.

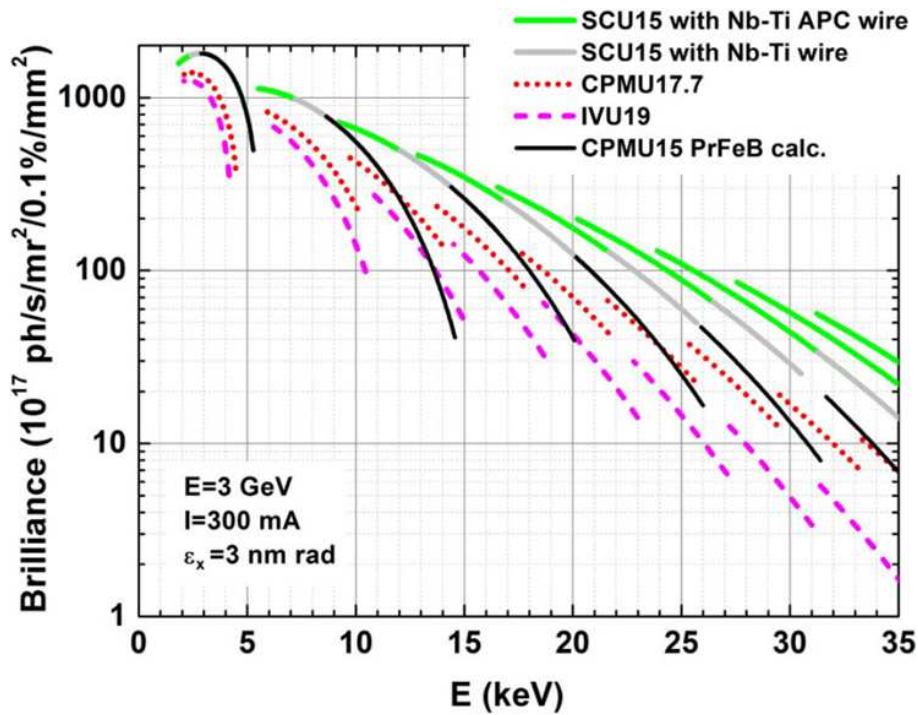


Figure 2.6: Comparison of the photon energy spectrum between in-vacuum permanent magnet undulators (IVU), cryocooled permanent magnet undulators (CPMU) and superconducting undulators (SCU) [12]. The numbers in the legend indicate the period length of the undulator in millimeter.

2.2 Beam heat load sources

There are several mechanisms that can act as a beam heat load source in electron storage rings, namely synchrotron radiation from the upstream bending magnet, longitudinal impedance and electron and/or ion bombardment of the chamber walls. They are described in the following.

2.2.1 Synchrotron radiation

In the upstream bending magnet of a straight section the electron beam produces synchrotron radiation tangentially to the beam trajectory. This creates a fan of radiation with a vertical and horizontal angular power distribution, which hits the outer part of the beam chamber with respect to the center of the storage ring, as well as the upper and lower surface, as indicated in red in Figure 2.7.

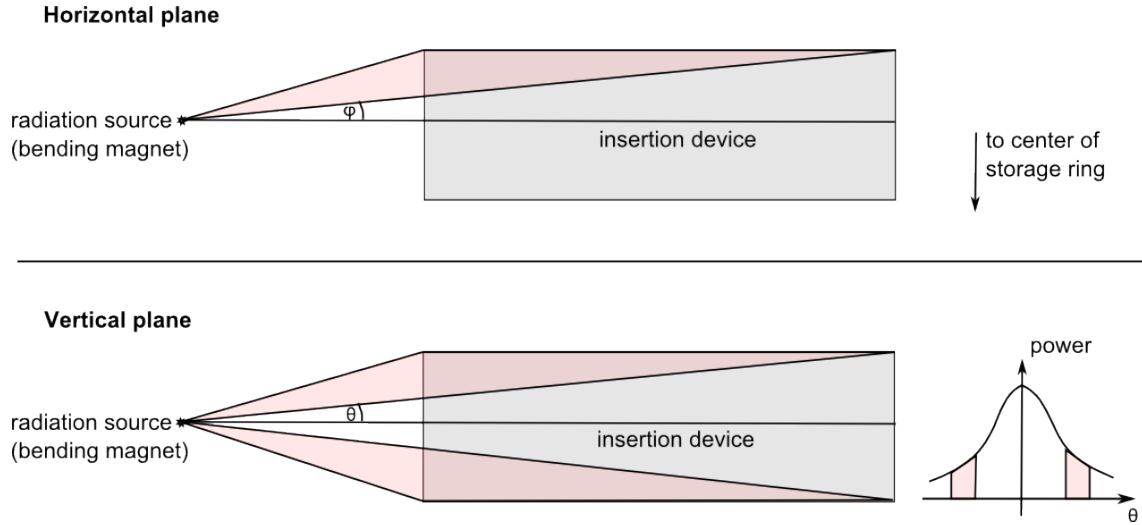


Figure 2.7: Sketch for the power deposition of synchrotron radiation from an upstream bending magnet in an insertion device in the horizontal and vertical plane.

The angular power distribution is given by [13]

$$\frac{dP}{d\Omega} [W/mrad^2] = \frac{7e^2}{64\pi\epsilon_0} \frac{\gamma^5 I}{\rho e} \frac{1}{(1 + \gamma^2\theta^2)^{5/2}} \left[1 + \frac{5\gamma^2\theta^2}{7(1 + \gamma^2\theta^2)} \right], \quad (2.4)$$

where θ is the vertical angle to the tangent of the motion of the electron beam, γ the relativistic factor, I the average beam current, ρ the bending radius, ϵ_0 the permittivity of free space and e the elementary charge. The power per mrad in the horizontal direction, integrated over all vertical angles, is given by [13]

$$P_{syn} [W/mrad] = \frac{eI\gamma^4}{6\pi\epsilon_0\rho} \quad (2.5)$$

Only a fraction of this power is hitting the beam tube surface of an insertion device, depending on its geometry and position (see Figure 2.7). For a cryogenic insertion device usually an absorber is placed in such a way that no synchrotron radiation can hit the cold surface directly. Reflected synchrotron radiation can still be absorbed in the cold surface, which is however too complex to calculate due to its dependence on the geometry, material and surface roughness of the beam pipe.

2.2.2 Longitudinal impedance

When a charged particle beam travels through a beam pipe its interaction with the metallic walls creates image currents and wakefields. These lead to a loss of energy that depends on the properties and geometry of the surface. The power lost by the beam P_{loss} can be described by a longitudinal beam coupling impedance $Z_{\parallel}(\omega)$. For a beam in a circular machine consisting of N equally spaced Gaussian bunches with bunch current I_b and bunch length σ_z the power loss is given by [14]:

$$P_{loss} = N^2 I_b^2 \sum_{p=-\infty}^{+\infty} \text{Re} Z_{\parallel}(pN\omega_0) |S(pN\omega_0)|^2, \quad (2.6)$$

where p is an integer, ω_0 the revolution frequency of the beam and $S(\omega)$ the bunch spectrum, which for a Gaussian bunch is:

$$S(\omega) = \exp\left(-\frac{\sigma_z^2 \omega^2}{2c^2}\right). \quad (2.7)$$

The multibunch spectrum, which is the Fourier transform of all bunches, consists of single lines separated by the bunch frequency $N\omega_0$ with the amplitude of the single bunch spectrum (see Figure 2.8).

Sharp resonance impedance

In case of a sharp resonance impedance, i.e. the impedance has a width smaller than $N\omega_0$ (the bunch spacing is $N\omega_0/(2\pi)$), at most one term of the sum in Equation 2.6 will contribute to the power loss. If the impedance does not coincide with any line of the multibunch spectrum, the power loss is 0. Otherwise it is given by:

$$P_{loss} = N^2 I_b^2 \text{Re} Z_{\parallel}(\omega_p) \exp\left(-\frac{\sigma_z^2 \omega_p^2}{c^2}\right), \quad (2.8)$$

where ω_p is the corresponding line of the multibunch spectrum. The result is very sensitive to the bunch spacing, which determines the position of the lines and the distance between them.

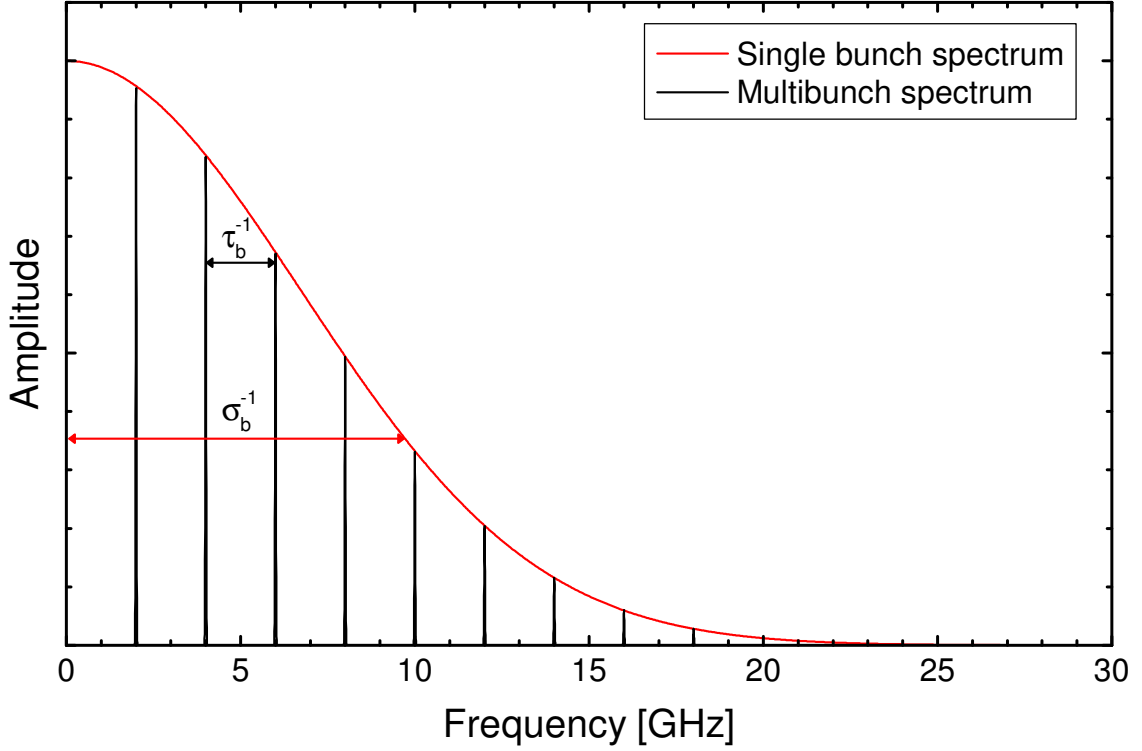


Figure 2.8: Difference between single bunch spectrum and multibunch spectrum. $\tau_b = 2\pi/(N\omega_0)$ is the time between two consecutive bunches and $\sigma_b = \sigma_z/c$ the bunch duration.

Broad-band impedance

If the bunch spacing is much larger than the bunch length ($\sigma_b^{-1} \gg \tau_b^{-1}$ in Figure 2.8) and in absence of resonant modes, Equation 2.6 can be transformed into an integral by multiplying with $N\omega_0/(N\omega_0)$:

$$P_{loss} = \frac{N^2 I_b^2}{N\omega_0} \sum_{p=-\infty}^{+\infty} \text{Re} Z_{\parallel}(pN\omega_0) |S(pN\omega_0)|^2 N\omega_0, \quad (2.9)$$

and substituting $N\omega_0 \rightarrow d\omega$, $pN\omega_0 \rightarrow \omega$, $\omega_0 \rightarrow 2\pi f_0$:

$$P_{loss} = \frac{N I_b^2}{\pi f_0} \int_0^{\infty} \text{Re} Z_{\parallel}(\omega) |S(\omega)|^2 d\omega. \quad (2.10)$$

The lower limit of the integral is changed to 0 by taking out a factor 2.

Broad Gaussian resonance impedance

As a simple academic case, I assume a Gaussian shape for a broad-band impedance centered around a resonance frequency ω_r :

$$ReZ_{||}(\omega) = R \cdot \exp\left(-(\alpha(\omega - \omega_r))^2\right). \quad (2.11)$$

Inserting this into Equation 2.10 and substituting $\omega = 2\pi f$ gives:

$$P_{loss} = \frac{I^2}{Nf_0} \cdot 2R \int_0^{\infty} \exp\left(-(\alpha(2\pi f - f_r))^2\right) df, \quad (2.12)$$

where $I = I_b N$ is the average beam current, $f_0 = \omega_0/2\pi$ and σ_b is the bunch duration.

The solution of the integral can be obtained from Mathematica [15]:

$$P_{loss} = \frac{I^2}{Nf_0} \cdot 2R \frac{\exp\left(-\frac{(2\pi\alpha\sigma_b f_r)^2}{\alpha^2 + \sigma_b^2}\right)}{4\sqrt{\pi}\sqrt{\alpha^2 + \sigma_b^2}} \cdot \left(1 + erf\left(\frac{2\pi f_r \alpha^2}{\sqrt{\alpha^2 + \sigma_b^2}}\right)\right) \quad (2.13)$$

Figure 2.9 shows the error function in this expression as a function of the resonance frequency f_r and the inverse of the resonance width α of the impedance, for a bunch duration $\sigma_b = 16.7$ ps, which is typical at the Diamond Light Source. For $\alpha \gg \sigma_b$ and at the relevant frequencies in the GHz region the error function can be approximated by 1:

$$P_{loss} = \frac{I^2}{Nf_0} \cdot \frac{1}{\sqrt{\pi}} \cdot \frac{R}{\alpha} \cdot \exp(-(2\pi f_r \sigma_b)^2) \quad (2.14)$$

$$\text{with } \alpha^2 + \sigma_b^2 \simeq \alpha^2 \quad \text{and} \quad \frac{\alpha^2}{\alpha^2 + \sigma_b^2} \simeq 1 \quad (2.15)$$

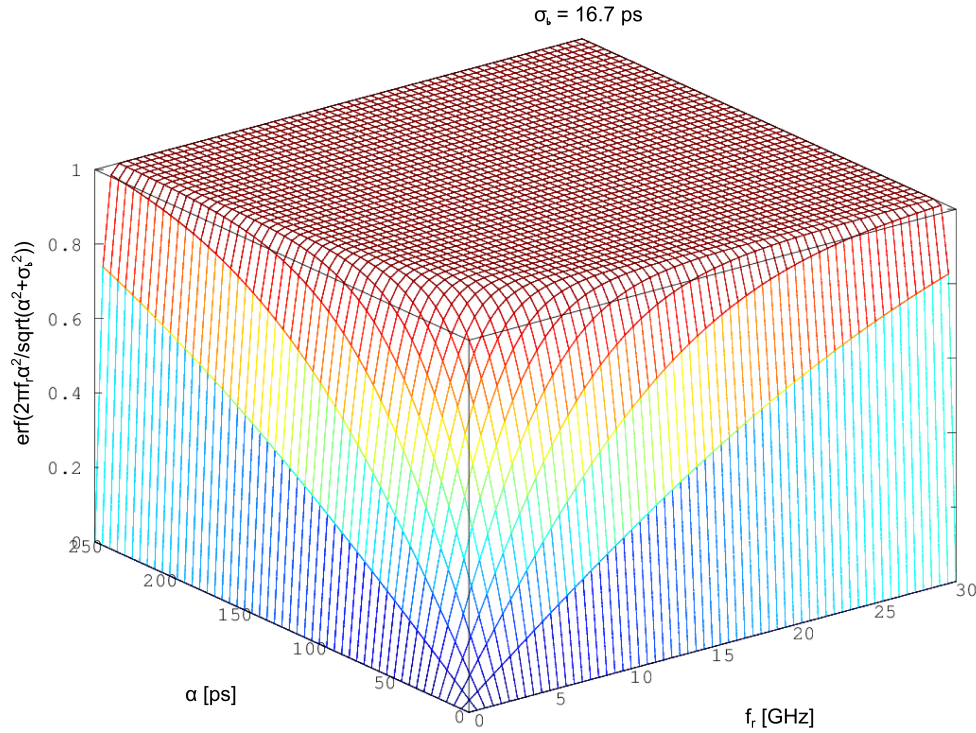


Figure 2.9: Parameter study of the error function in Equation 2.13.

The condition $\alpha \gg \sigma_b$ is only allowed as long as the resonance impedance is still broad compared to the distance between single lines in the multibunch spectrum, which is the case under study.

Step transition impedance

A step transition describes a step-like change in the beam pipe cross section, where the step size is much smaller than the dimensions of the beam pipe. For a step-out transition in a round beam pipe above the beam pipe cut-off frequency the real part of the longitudinal impedance is given by [16]:

$$\operatorname{Re}Z_{\parallel}(\omega)_{\text{step-out}} = \sqrt{\frac{\mu_0}{\varepsilon_0}} \frac{1}{\pi} \ln \left(\frac{r_1 + d}{r_1} \right), \quad (2.16)$$

where μ_0 is the permeability of free space, r_1 is the beam pipe radius before the step, d is the step size and $d \ll r_1$. The power loss due to a step-in transition is negligible. The integral in Equation 2.10 can be executed easily for the limiting case of high frequencies. The result for the power loss is:

$$P_{step} = \frac{I^2}{N f_0} \frac{\sqrt{\mu_0}}{\sqrt{\varepsilon_0} 2\pi^{3/2}} \frac{c}{\sigma_z} \ln \left(\frac{r_1 + d}{r_1} \right). \quad (2.17)$$

The bunch length dependence of the power loss $P \propto \sigma_z^{-1}$ can be used to differentiate the step transition from other impedance effects.

For an elliptical cross section of the beam pipe, like it is the case in COLDDIAG, computer simulations with CST Particle Studio [17] have been performed to show that also in this case a constant impedance can be used to estimate an upper limit of the power loss [18]. With typical beam parameters of the Diamond Light Source the power loss for a 10 μm step at the end of the cold liner is below 1 W and for a 100 μm step between the 50 K shield and the 300 K liner it is below 14 W.

Resistive wall impedance

When a charged particle beam is travelling through a beam tube it creates image currents of opposite charge in the conducting walls (with finite conductivity). This is known as skin effect, because for an alternating electron current the image currents flow only in the outer layer of the conducting walls. The thickness of this layer is called skin depth δ and depends on the angular frequency ω of the electric field generated by the beam:

$$\delta(\omega) = \sqrt{\frac{2\rho}{\mu_r \mu_0 \omega}}, \quad (2.18)$$

where ρ is the dc resistivity of the wall material and μ_r/μ_0 the relative/absolute permeability. The surface resistance of a quadratic surface area is defined as

$$R_s(\omega) = \frac{\rho}{\delta} = \sqrt{\frac{\mu_r \mu_0 \omega \rho}{2}}. \quad (2.19)$$

When the mean free path of the electrons in the surface metal λ becomes much larger than

the skin depth δ the classical model for the skin effect is invalid, because only conduction electrons moving almost parallel to the wall surface contribute to the image current. In this case the surface resistance is given by the anomalous skin effect [19]:

$$\begin{aligned}
 R_s &= R_\infty (1 + 1.157\alpha^{-0.276}) , \quad \text{for } \alpha \geq 3 \\
 \alpha &= \frac{3}{4}\omega\mu_0(\rho\lambda)^2\rho(T)^{-3} \\
 R_\infty &= \left(\frac{\sqrt{3}}{16\pi}(\rho\lambda)(\omega\mu_0)^2 \right)^{\frac{1}{3}}
 \end{aligned} \tag{2.20}$$

The product $\rho\lambda$ is a characteristic constant for a specific metal, according to the Drude model of electrical conduction [20]. The resistivity in α introduces a temperature dependence into R_s , which is typically characterised by the RRR value (residual-resistivity ratio) of the metal - the ratio between the dc resistivity at 300 K and at very low temperatures, where only impurities contribute to the resistivity of the metal; for copper the resistivity barely changes below 20 K. Figure 2.10 shows the difference between the surface resistance from the normal skin effect at room temperature and the anomalous skin effect, when the resistivity is 100 times smaller than at room temperature ($RRR = 100$).

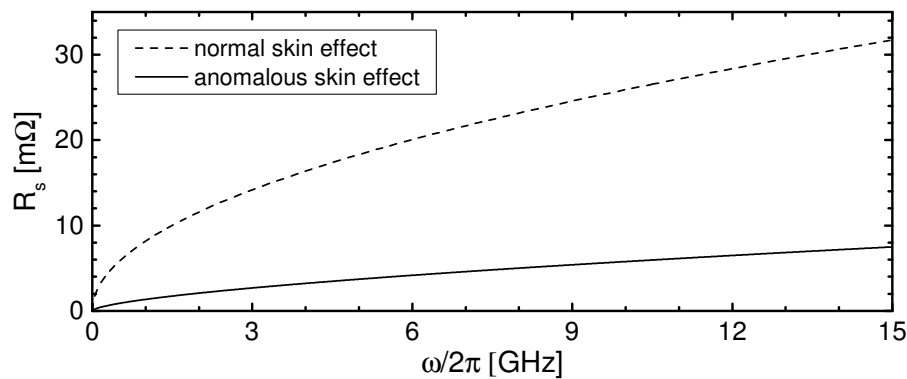


Figure 2.10: Difference between normal skin effect for copper at room temperature and anomalous skin effect at low temperatures with $RRR = 100$ up to 15 GHz.

The surface resistance of the beam tube gives rise to resistive heating along the beam tube walls. A wall resistance $R_{wall}(\omega)$ that relates the surface resistance to the wall geometry can be defined as:

$$R_{wall}(\omega) = \frac{L}{l} R_s(\omega) , \tag{2.21}$$

where L/l is a geometry factor that for a circular beam pipe is simply the length of the beam pipe divided by its circumference. For an elliptical cross section, where one semi-axis is much larger than the other, the same formula holds true with l being 2π times the small semi-axis [16].

In case of the normal skin effect, using Equation 2.10 and 2.19 gives the well-known expression for the beam heat load due to classic resistive wall heating:

$$P_{norm} = \Gamma \left(\frac{3}{4} \right) \frac{L}{2\pi l} \sqrt{\frac{\mu\rho}{2}} \left(\frac{c}{\sigma_z} \right)^{\frac{3}{2}} \frac{I^2}{Nf_0}. \quad (2.22)$$

In case of the anomalous skin effect the term for the heating power becomes more complex:

$$P_{anom} = \frac{L}{2\pi l} \frac{I^2}{Nf_0} \left(\frac{\sqrt{3}}{16\pi} \rho\lambda\mu_0^2 \right)^{\frac{1}{3}} \Gamma \left(\frac{5}{6} \right) \left(\frac{c}{\sigma_z} \right)^{\frac{5}{3}} \cdot f(\sigma_z, \rho) \quad (2.23)$$

$$f(\sigma_z, \rho) = 1 + \frac{\Gamma(0.695)}{\Gamma(\frac{5}{6})} \left(\frac{c}{\sigma_z} \right)^{-0.277} \cdot 1.157 \left(\frac{3}{4} \mu_0 (\rho\lambda)^2 \rho^{-3} \right)^{-0.276} \quad (2.24)$$

While for the normal skin effect the dependence on the bunch length is simply $P \propto \sigma_z^{-3/2}$, in the anomalous case it depends on the resistivity of the metal. If the second term in Equation 2.24 is small compared to the first term, the bunch length dependence can be approximated by $P \propto \sigma_z^{-5/3}$. This will be examined in the following by assuming the bunch length to be in the range between 3.6 mm (12 ps) and 7.2 mm (24 ps), as it is the case for the measurements in this work, and using the resistivity of copper $\rho_{4K} = 1.7 \cdot 10^{-8} \Omega\text{m}/\text{RRR}$. Then Equation 2.24 can be simplified:

$$f(\sigma_z, \text{RRR}) = 1 + 24.45 \cdot \text{RRR}^{-0.828} \cdot \sigma_z^{0.277} \quad (2.25)$$

$$f(3.6 \text{ mm}, \text{RRR}) < 1.1 \quad \text{for} \quad \text{RRR} > 117 \quad (2.26)$$

$$f(7.2 \text{ mm}, \text{RRR}) < 1.1 \quad \text{for} \quad \text{RRR} > 147 \quad (2.27)$$

This means that for high RRR values above 117-147 the bunch length dependence $P \propto \sigma_z^{-5/3}$ is expected for resistive wall heating, and for lower RRR values an additional component with $P \propto \sigma_z^{-1.39}$ starts to be significant to the heating. The RRR value for a surface similar to the surface of the COLDDIAG liner has been studied [21]. The measurements show a

RRR value of 150-200.

Surface roughness

Surface roughness can be a source of impedance, if the size of the corrugations on the surface are of the same order as the bunch length of the beam. One way to define the roughness is to treat the corrugations as peaks with an average height h and an average distance g between them. These parameters have been measured for a sample made from a $50\ \mu\text{m}$ layer of galvanized copper on a $300\ \mu\text{m}$ stainless steel foil, using the same galvanization process as for the COLDDIAG liner [18]. The measured surface roughness is $h \sim 1\ \mu\text{m}$ and $g \sim 30 - 40\ \mu\text{m}$. Compared to the bunch length at Diamond of about $5\ \text{mm}$ the corrugations on the liner surface are about 3 orders of magnitude smaller and therefore not visible to the beam. For this reason any impedance originated from the surface roughness is considered negligible.

Comparison of impedance types

The types of impedances mentioned in the previous sections are summarized graphically in Figure 2.11. It can be seen that the frequency dependence of the impedance can have a big impact on the power loss, which is given by its convolution with the bunch spectrum.

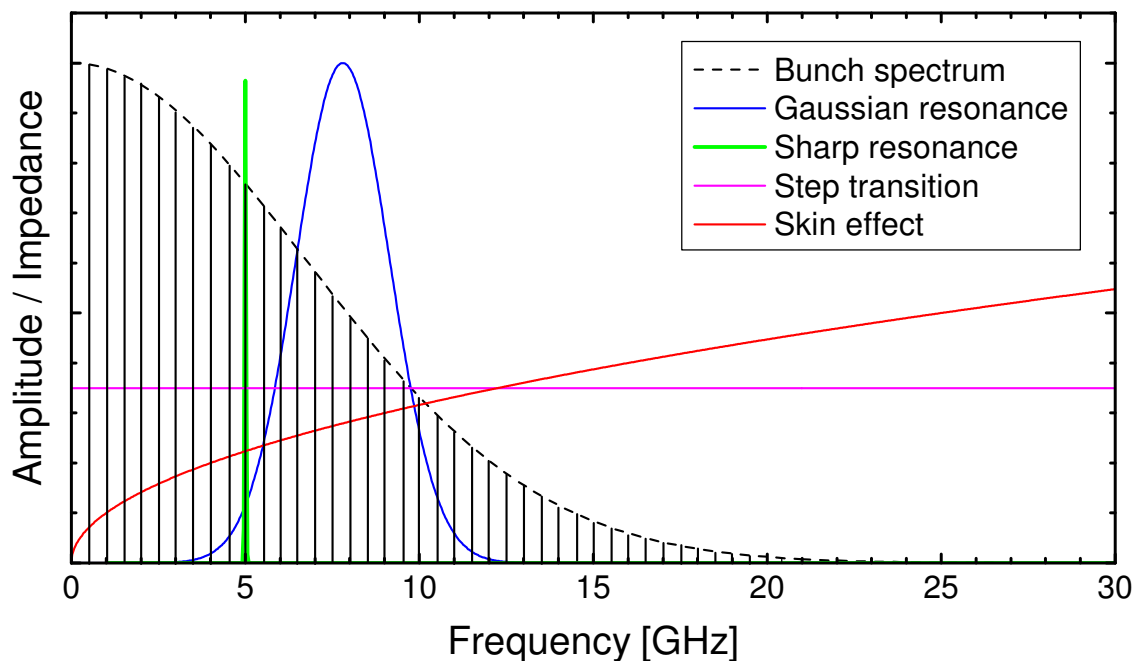


Figure 2.11: Comparison between different sources of impedance and their overlap with the bunch spectrum.

2.2.3 Electron/ion bombardment

Another possible heating mechanism is that charged particles in the residual gas of the beam chamber get accelerated towards the chamber wall by the electric fields of a passing electron bunch. The primary particles for this mechanism in electron machines are photoelectrons generated by synchrotron radiation. When they get emitted into the vacuum they are accelerated back into the chamber wall by a passing electron bunch and generate secondary electrons, which repeat the process. This mechanism is called electron multipacting and can lead to a measurable heat load in the chamber wall, as well as the build-up of an electron cloud in the beam vacuum.

A simple model for a circular beam in a circular beam pipe is described in [22], where the electric field E and the line charge of the electron bunch λ is given by:

$$E(r) = \frac{\lambda}{2\pi\epsilon_0 r} \quad \lambda = \frac{eN_b}{c\tau}, \quad (2.28)$$

with the electron charge e , the particles per bunch N_b , the speed of light c and the bunch duration τ (bunch length in time domain).

$$\Delta p = eE(r)\tau = \frac{e^2 N_b}{2\pi\epsilon_0 c r} \quad (2.29)$$

is the momentum that one electron bunch transfers to a stationary electron at distance r from the center, which does not depend on the bunch length. This corresponds to a transferred energy of

$$\Delta W = \frac{\Delta p^2}{2m_e} = 2m_e c^2 r_e^2 \left(\frac{N_b}{r}\right)^2, \quad r_e = \frac{e^2}{4\pi\epsilon_0 m_e c^2} \quad (2.30)$$

where r_e is the classical electron radius and m_e the electron mass. For the build-up of an electron cloud this energy has to be large enough to produce more than one secondary electron. Furthermore the time between consecutive bunches has to be such that the secondary electrons get accelerated against the chamber wall as well.

A good source of electrons for electron multipacting and the generation of an electron cloud is the cryosorbed gas layer on a cold surface. It is created by energetic particles hitting

the surface oxide layer of the beam chamber and desorbing gas into the beam vacuum, which recondenses on the cold surface (cryo-pumping). The recondensed gas is only loosely bound on the surface and gets continuously desorbed and recondensed by energetic particles passing through into the chamber wall (recycling [23]). At a certain layer thickness of the physisorbed (recondensed) gas an equilibrium is reached. The layer thickness depends on the pressure in the beam vacuum and the type of gas in the layer depends on the temperature and material of the chamber surface. For a typical copper surface between 4 K and 20 K the cryosorbed gas layer consists mainly of hydrogen and is several atom layers thick [24].

2.3 Network analysis

In the second part of the measurements network analysis will be used as a standard technique for impedance determination in the microwave regime to further investigate RF heating as a possible source for the beam heat load. In the following the basic principles, on which the measurements rely, will be introduced. They are found in greater detail in the standard textbooks (e.g. [25]).

2.3.1 The scattering matrix

The transmission and reflection of microwave signals in a device under test (DUT) can be described by the scattering matrix, which relates the incident waves to the reflected waves at the ports of the device. In this work the measurements will be performed on a 2-port network, which leads to a 2×2 scattering matrix defined like:

$$\begin{bmatrix} V_1^- \\ V_2^- \end{bmatrix} = \begin{bmatrix} S_{11} & S_{12} \\ S_{21} & S_{22} \end{bmatrix} \times \begin{bmatrix} V_1^+ \\ V_2^+ \end{bmatrix} \quad (2.31)$$

The vectors stand for the voltages of the incident (+) and reflected (-) waves at port 1 and 2, which are measured with a vector network analyzer (VNA). The determination of the S-parameters (elements of the scattering matrix) is done in two steps. First an incident wave is sent into port 1 of the DUT, i.e. $V_2^+ = 0$, and the voltages induced by the reflected waves are detected. Then the same measurement is done on the other port. This gives the following relations for the S-parameters:

$$S_{11} = \frac{V_1^-}{V_1^+} \quad S_{21} = \frac{V_2^-}{V_1^+} \quad S_{12} = \frac{V_1^-}{V_2^+} \quad S_{22} = \frac{V_2^-}{V_2^+} \quad (2.32)$$

In general S_{ij} is the ratio between the reflected wave at port i and the incident wave at port j . Since the VNA detects fields, the S-parameters have to be squared in order to get power relations. For an incident wave on port 1 S_{11}^2 gives the power fraction reflected at port 1, and S_{21}^2 gives the power fraction transmitted through to port 2. From the energy conservation in a 2-port network follows:

$$S_{11}^2 + S_{21}^2 = 1 - \text{losses} \quad \text{and} \quad S_{12}^2 + S_{22}^2 = 1 - \text{losses} \quad (2.33)$$

The losses represent energy absorbed by the device, for example through the skin effect.

2.3.2 TEM resonator

In this work we are interested in the longitudinal beam coupling impedance introduced by the liner. The real part of this impedance is proportional to the losses of an electromagnetic wave travelling through the structure. A standard method for measuring the beam coupling impedance is the wire method, where a thin wire is stretched along the beam axis to create transverse electromagnetic (TEM) field distributions and simulate the fields of the electron beam. This technique has its limitations for small impedances (e.g. resistive wall impedance of about 1Ω for a smooth copper surface), for which the sensitivity is too low. Instead the wire can be exchanged with a capacitively coupled inner conductor, transforming the setup into a TEM resonator [26]. A drawback of this method is that the impedance can only be determined at the resonant frequencies of the structure, which depend mainly on its length in beam direction. For a resonator of length L the resonant modes (with mode number n) are therefore defined by:

$$n \cdot \frac{\lambda_{res}}{2} = L \quad \text{or} \quad f_{res} = n \cdot \frac{c}{2L}, \quad (2.34)$$

where f_{res} and λ_{res} is the resonant frequency and its corresponding wavelength, and c is the speed of light. For a length of 0.5 m the fundamental mode is at 300 MHz and thus the points where the impedance can be evaluated are separated by 300 MHz.

2.3.3 Loaded and unloaded quality factor

The amount of losses in a resonator can be deduced from its quality factor. There is a difference between the unloaded quality factor Q_0 , which is the quality factor of the resonator itself without any external circuitry and can therefore not be measured directly, and the loaded quality factor, which includes the measurement lines and is lower than

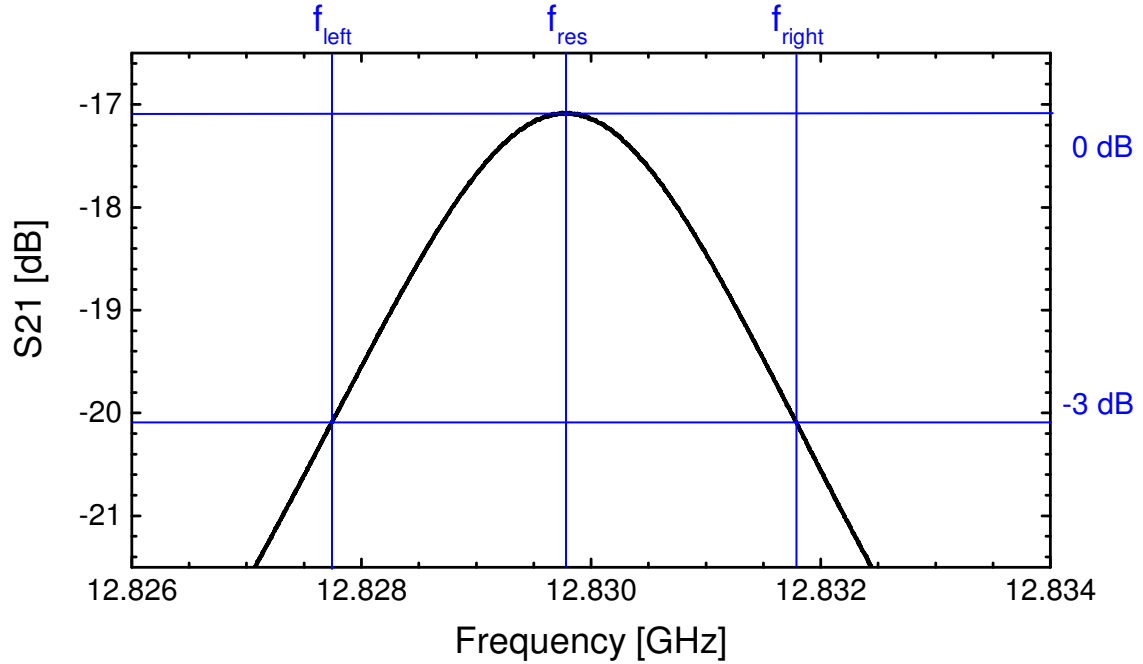


Figure 2.12: Determination of the loaded quality factor of a resonator.

the unloaded quality factor. The loaded quality factor Q_L is the ratio between the center frequency f_{res} of the resonance peak and its full width at half maximum $f_{right} - f_{left}$, which is at -3 dB in logarithmic units (see Figure 2.12). The difference between the loaded and unloaded quality factor depends on the coupling κ of the measurement lines to the resonator. For a two-port transmission resonator that is equally strong and weakly coupled (capacitively) on both ports, the unloaded quality factor is given by [27]:

$$Q_0 = Q_L \cdot (1 + \kappa) \quad Q_L = \frac{f_{res}}{f_{right} - f_{left}} \quad (2.35)$$

The coupling coefficient can be determined from the S-parameter for the transmission:

$$\kappa = \frac{S_{21}}{1 - S_{21}} \quad (2.36)$$

2.3.4 Attenuation, impedance and surface resistivity

The internal loss of a resonator is given by the unloaded quality factor Q_0 [28]. Alternatively the internal loss can be expressed by an attenuation constant α_0 in Np/m , which describes an equivalent 1 m long transmission line with the same loss:

$$\alpha_0 = \frac{\pi}{\lambda_{res} Q_0} \quad \text{and} \quad \alpha_0 \left[\frac{1}{m} \right] = \ln \frac{1}{S_{21}^{\alpha_0}}, \quad (2.37)$$

where $S_{21}^{\alpha_0}$ is the transmission through the equivalent transmission line, which includes the losses of the inner conductor.

The inner conductor in the previous discussed TEM resonator gives rise to an attenuation α_w , depending on the skin effect and the geometry. For a coaxial line with outer diameter D the attenuation α_w is given by:

$$\alpha_w = \sqrt{\pi \rho_w \varepsilon f_{res}} \frac{1}{d \ln \frac{D}{d}} \quad (2.38)$$

with an inner conductor of resistivity ρ_w and diameter d , ε being the permittivity and f_{res} the frequency. Since the loss due to the inner conductor is included in the unloaded quality factor, the attenuation due to the structure itself is the difference between the total attenuation and the attenuation caused by the inner conductor ($\alpha = \alpha_0 - \alpha_w$). This attenuation constant α can be used to calculate the real part of the beam coupling impedance $Re(Z)$ by utilizing $\alpha = \ln(1/S_{21}^{\alpha})$ (Equation 2.37) and $Re(Z) = -2Z_L \ln S_{21}^{\alpha}$ [29]:

$$Re(Z) \left[\frac{\Omega}{m} \right] = 2Z_L \cdot \alpha \quad (2.39)$$

S_{21}^{α} is the transmission through a transmission line with attenuation α and Z_L is the line impedance or characteristic impedance of the transmission line. For a circular beam pipe it is $Z_L = 60\Omega \cdot \ln \frac{D}{d}$, which is the well known expression for a coaxial line. If the shape is different an additional geometric factor has to be included in the logarithm, for example 1.27 for a wire between two parallel plates [28].

The real part of the beam coupling impedance can be determined by measuring S_{21} and the frequency of each resonance, as well as the full width half maximum of the resonance peak. From these values the attenuation α_0 can be calculated. By subtracting from α_0 the attenuation caused by the inner conductor α_w , α can be derived and hence the impedance. For comparison of the longitudinal impedance to literature values for the loss due to the skin effect, it is useful to transform it into a surface resistivity R_s . Since the impedance is given in Ω per unit length, first it has to be multiplied by the length of the resonator and then divided by a geometric factor that transforms the surface into a square. For simple shapes like a coaxial line, where the cross section does not change, the length cancels out and the surface resistivity is given by:

$$R_s \left[\frac{\Omega}{\square} \right] = 2Z_L \cdot \alpha \cdot \pi D \quad (2.40)$$

CHAPTER 3

Experimental setups

This work deals with beam heat load measurements performed with COLDDIAG, while it was installed at the Diamond Light Source, the subsequent offline calibration and impedance bench measurements performed on the COLDDIAG structure and other test samples. The experimental setups will be described in the following, preceded by a summary of the beam parameters and operation modes utilized in the DLS storage ring.

3.1 DLS beam parameters and operation modes

The main machine parameters of the DLS are listed in Table 3.1. During the time COLDDIAG was installed in the DLS storage ring three main operation modes were run for user operation:

- Standard mode: 300 mA beam current in 900 consecutive bunches, 15.8 ps bunch length.
- Hybrid mode: 300 mA beam current in 685 consecutive bunches and one higher charge bunch, 16.6 ps bunch length.
- Low alpha mode: 10 mA/20 mA beam current in 200/400 consecutive bunches, 3.5 ps bunch length.

Table 3.1: Machine parameters of the Diamond Light Source.[30]

Electron beam energy	3 GeV
Nominal beam current	300 mA
Circumference	561.6 m
Revolution frequency	533.8 kHz
RF frequency	499.654 MHz
Maximum no. of bunches	936

In the machine physics sessions special operation modes could be used:

Beam current ramps

Instead of injecting directly to the maximum beam current for a specific filling pattern, the injection can be paused at intermediate values of the beam current. A waiting time of 15 to 30 minutes before continuing the injection allows to measure the beam heat load at the respective beam current. This procedure is referred to as beam current ramp in this work. The beam current is measured using a parametric current transformer (PCT) [31]. Since the accuracy is specified to 0.1%, the measured beam current values are assumed to be without error throughout this work.

Equally spaced bunches

In user operation only consecutive buckets are filled with electrons, resulting in a bunch spacing of 2 ns and a larger gap between the first and the last bunch, which depends on the total number of bunches.

Equally spaced bunches can be achieved by filling every n -th bucket. This is only possible if n multiplied with the number of bunches equals 936 (the total number of buckets). The filling patterns used for the measurements are shown in Figure 3.1.

The bunch charge distribution of the filling patterns is measured by time correlated single photon counting [32].

Variable bunch length

The bunch length is an important parameter of the electron beam. In Figure 3.2 the bunch length is reported as a function of the bunch charge. It increases with bunch charge, because an increasing number of electrons takes up more phase space. For a fixed bunch charge the bunch length can be changed by setting a different RF voltage in the accelerating cavities of the storage ring [26]. A higher RF voltage leads to a steeper zero-crossing of the field, which squeezes the RF bucket and results in a smaller bunch length. The possible range of RF voltages is limited by the stability of the electron beam. Figure 3.3 shows the possible RF voltages and their corresponding bunch length in the DLS storage ring. The bunch length is measured with a streak camera [31].

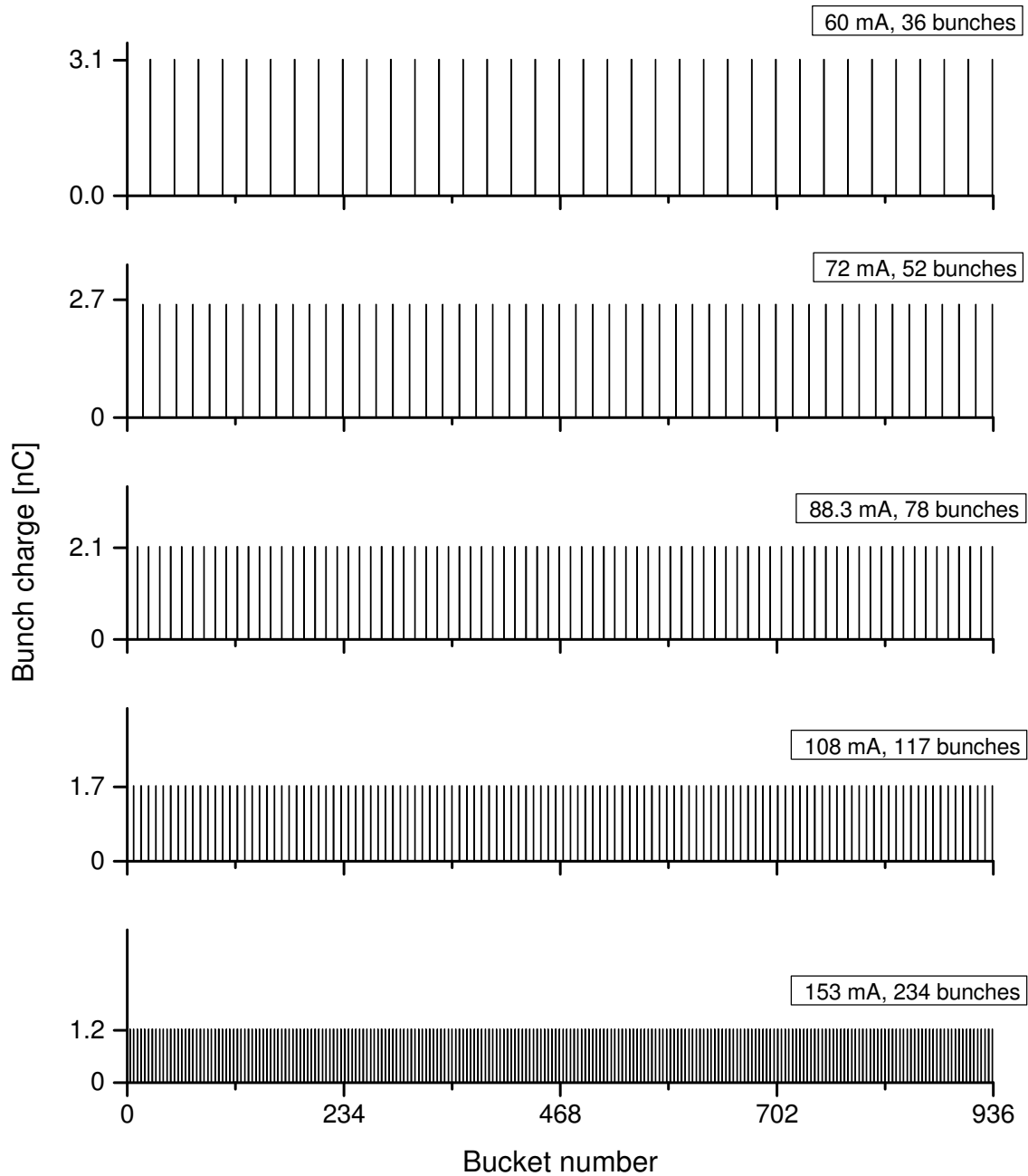


Figure 3.1: Filling patterns with equally distributed bunches.

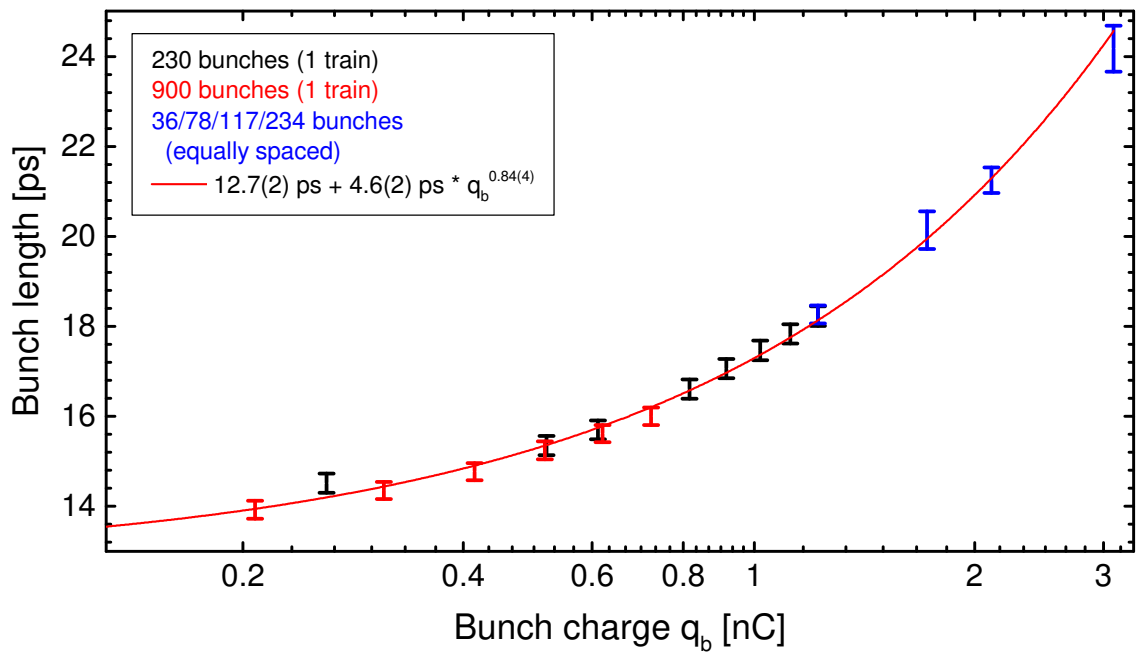


Figure 3.2: Bunch length as a function of bunch charge for different filling patterns. The fit function is a combination of a constant (zero current bunch length) and a power law for the bunch charge dependence (Courtesy of G. Rehm and C. Thomas).

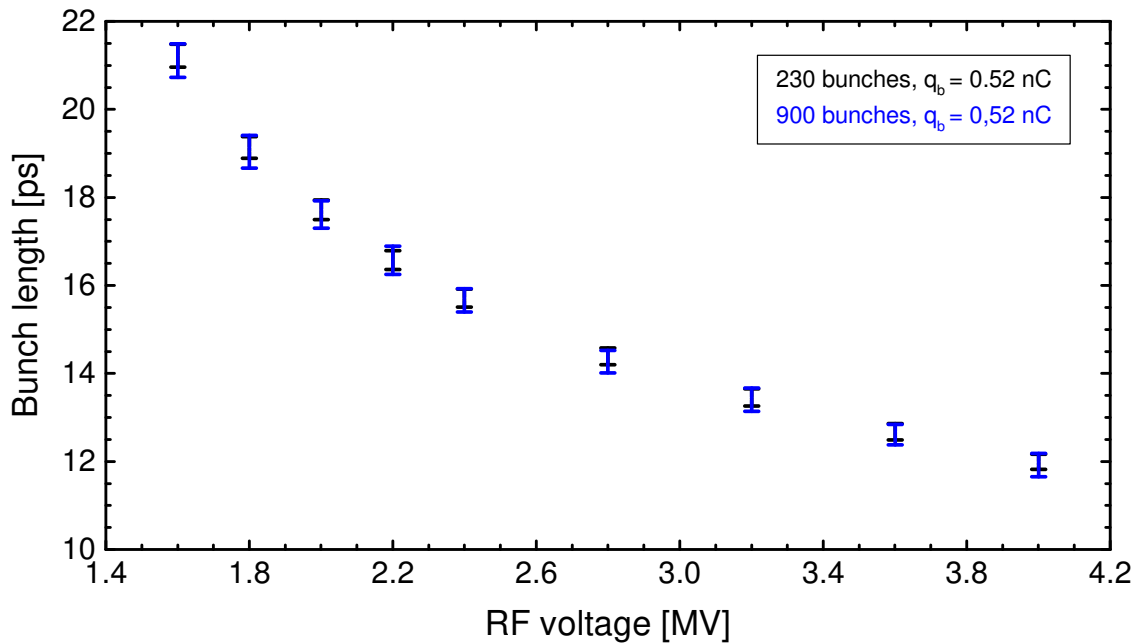


Figure 3.3: Bunch length as a function of the voltage in the RF cavities for two different filling patterns with the same bunch charge $q_b = 0.52 \text{ nC}$ (Courtesy of G. Rehm and C. Thomas).

3.2 A COLD vacuum chamber for DIAGnostics (COLDDIAG)

The knowledge of the heat intake from an electron beam is essential in the design of the cryogenic layout of superconducting insertion devices. COLDDIAG is an important part for the development of superconducting insertion devices at ANKA, because it has been built with the aim of measuring the beam heat load to a cold bore and understanding the underlying heating mechanism. From the design of COLDDIAG [6] to its factory acceptance test [7] and the second installation in the Diamond Light Source storage ring in 2012, many details have changed and can be followed in the PhD thesis of S. Gerstl [33]. In this section the setup as of August 2012 will be described together with the modifications since then.

3.2.1 Vacuum layout

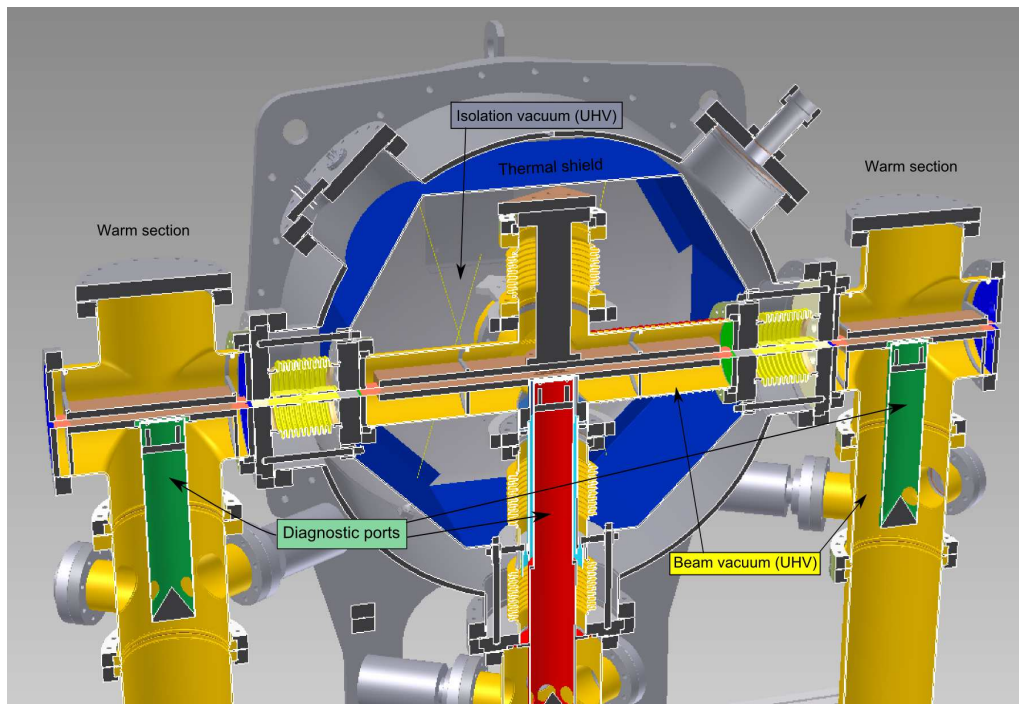


Figure 3.4: Overview of the vacuum layout of COLDDIAG. The beam vacuum is highlighted in yellow.

An overview of the vacuum layout is shown in Figure 3.4. A cold vacuum chamber is located between an upstream and a downstream warm section. This allows for a direct comparison between measurements at cryogenic temperatures and at room temperature. While in the warm sections there is just one ultrahigh vacuum (UHV) needed for the beam, the cold section has an additional isolation vacuum, separated by a six-way cross, to intercept unwanted heat intake from outside through convection.

The electron beam goes through a liner with an elliptical cross section (semiaxes 5 mm

and 30 mm) made from a solid copper block for thermal stabilization. The inner surface of the liner is plated with $50\ \mu\text{m}$ of copper, resembling the copper-plated stainless steel foils used for superconducting insertion devices at ANKA, since the resistive wall heating losses occur only in the first few μm of the surface. The operating temperature of the liner in superconducting insertion devices is typically between 4 K and 20 K. Therefore COLDDIAG is designed in such a way that the liner temperature reaches 4 K without beam. This is achieved through conduction cooling with a Sumitomo RDK-415D cryocooler.

In each section there is a diagnostic tube connected to the liner through six off-center slots (Figure 3.5). The slots allow gas and low energy charged particles to reach the diagnostic devices. In the cold section the design is based on the COLDEX device [34]. The tube is kept warm by introducing a 1 mm gap between the cold liner and the tube to avoid gas condensation on the way to the diagnostics. In the warm sections the diagnostic tubes can be connected without thermal separation.

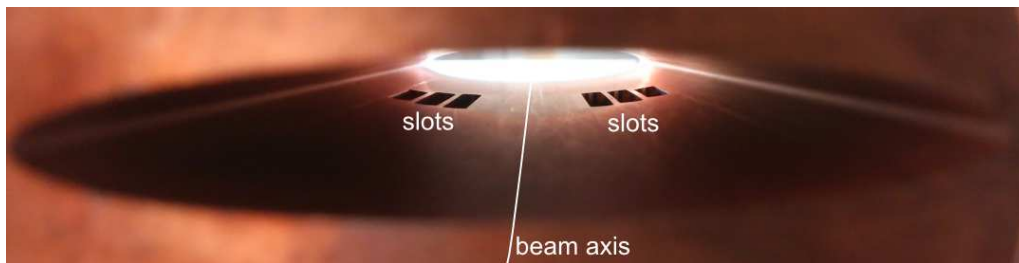


Figure 3.5: Slots to the diagnostic port in one of the warm sections of the liner.

3.2.2 Cryogenic layout

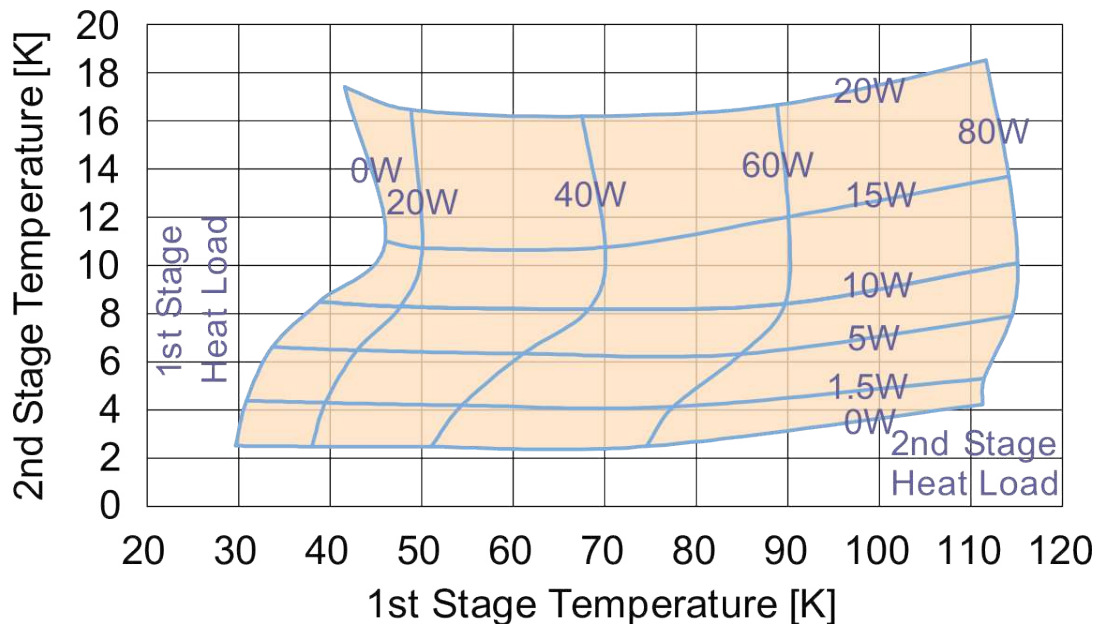


Figure 3.6: RDK-415D Cold Head Capacity Map (50 Hz)[35].

COLDDIAG is a cryogen-free system. The cold section is cooled by a Gifford-McMahon type cryocooler, which uses a closed-loop helium line. The cooling power depends on the temperature at the two stages of the cryocooler (see heat load map in Figure 3.6). With the first stage connected to the thermal shield at 50 K and the second stage connected to the cold liner at 4.2 K it has a cooling power of 35 W and 1.5 W, respectively.

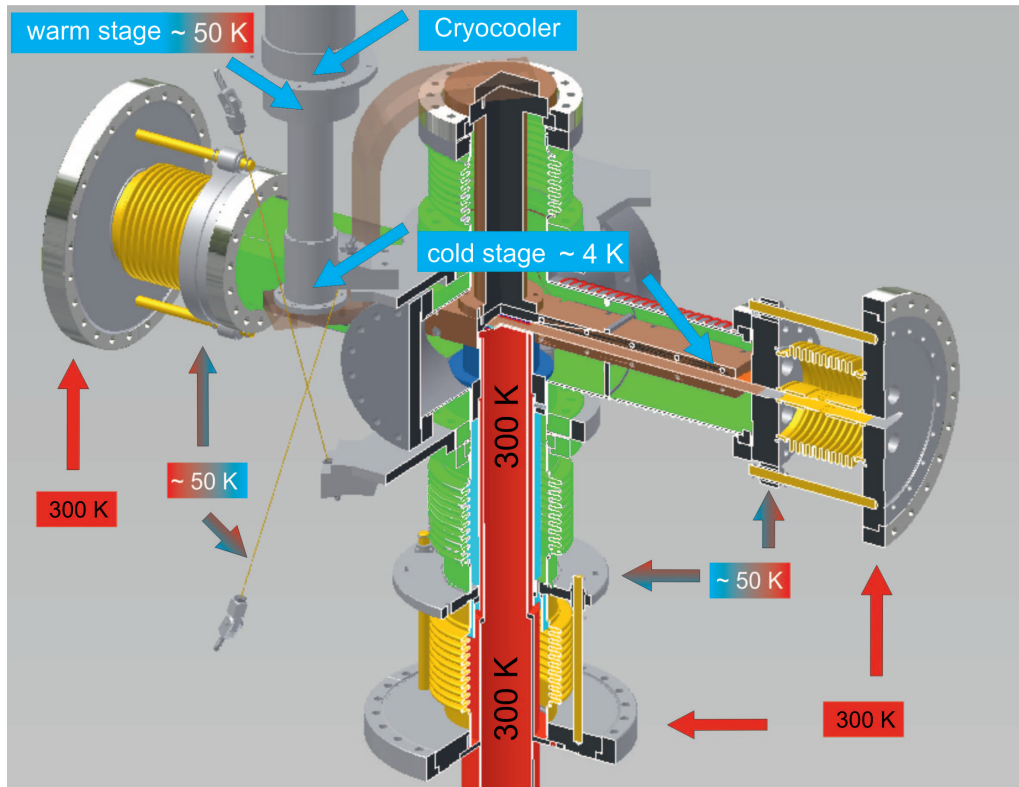


Figure 3.7: Overview of the cryogenic layout of COLDDIAG. The green and yellow surfaces separate the beam vacuum from the isolation vacuum.

For the cryogenic design of the experiment and in order to understand and calibrate the measurements it is important to know the heat intake paths of the system (see Figure 3.7). Heat transfer by convection is sufficiently suppressed by the isolation vacuum and can be neglected.

The estimated heat transfer by conduction and radiation is summarized in Table 3.2. The transition between the warm sections at 300 K and the cold section at 4 K is done in two stages with an intermediate thermal shield at 50 K, to minimize the heat intake through conduction and radiation. A crucial part for the whole system are the thermal transitions of the liner, especially between the 50 K region and the cold liner. They have to be made in such a way that the electrical continuity is preserved. On the other hand the thermal contact has to be minimal in order to reach a low base temperature at the cold liner and prevent the beam heat load measurement from being shadowed by heat load intakes different from the beam heat load on the liner (i.e. heat load from higher temperature regions).

The heat transfer by conduction to the second stage of the cryocooler is limited to the thermal transitions at the liner ends. The thermal shield is collecting the heat intake from the rods holding the inner UHV chamber, from the RF bellows connecting the warm sections and from the solenoid, and transfers it to the first stage of the cryocooler, which has much more cooling power than the second stage (see Figure 3.6).

Most of the heating from radiation is taken by the thermal shield. Only the temperature difference between the thermal shield and the cold liner as well as the necessary openings for the electron beam and the diagnostics lead to a heat load contribution from radiation. For the calibration of the beam heat load measurement it has to be taken into account that the heat conduction over the thermal transitions at the liner ends is larger with beam, because the temperature of the flanges on the 50 K side of the transitions increases with beam.

3.2.3 Diagnostics

With COLDDIAG it is possible to measure the beam heat load, the temperature distribution on the liner, the total pressure and residual gas content, as well as the total flux and spectrum of low energy charged particles hitting the chamber walls. Figure 3.8 contains an overview of the installed diagnostics that will be described in the following.

Temperature sensors and heaters

COLDDIAG is equipped with 42 temperature sensors. Most of the sensors are distributed along the liner, 16 in the cold section and 8 in each warm section. The remaining sensors are placed at different positions in the cryostat, i.e. the two cryocooler stages, the thermal transitions from the cold liner to the 50 K shield, the 50 K shield, the solenoid and the six-

Table 3.2: Estimated heat intake from conduction and radiation to the first and second stage of the cryocooler without beam [36].

	300 K - 50 K	50 K - 4 K
Radiation	12 W	0.2 W
	Thermal shield (8 W)	Thermal shield (0.06 W)
	Diagnostic tube (4 W)	Diagnostic tube (0.12 W)
		Liner ends (0.02 W)
Conduction	40 W	0.4 W
	Thread rods (3 W)	Thermal transition
	Stainless steel rods (14 W)	at liner ends
	RF bellows + fingers (14 W)	
	Solenoid at 1 A (8 W)	
Total heat	52 W	0.6 W

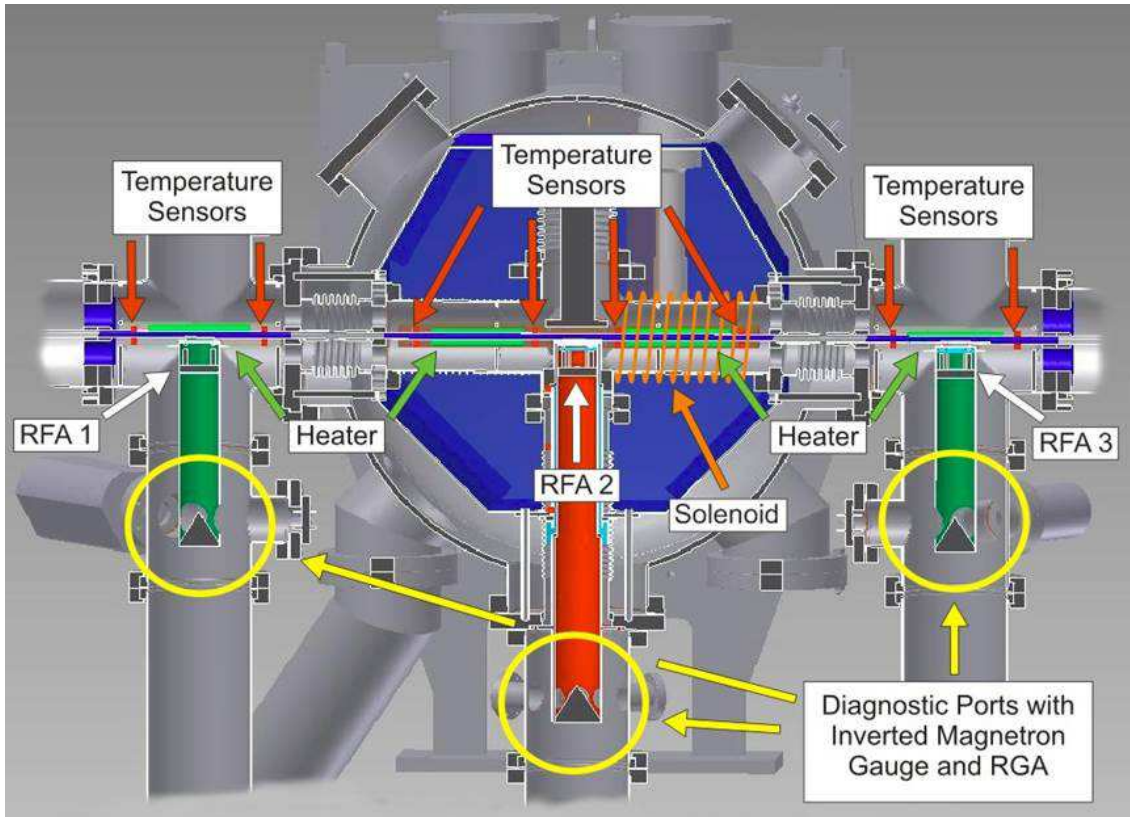


Figure 3.8: Overview of the diagnostics installed in COLDDIAG.

way cross containing the cold liner. The beam heat load is measured with a temperature sensor at the cooling connection between the cold liner and the second stage of the cryocooler.

For temperatures above 50 K Pt-100 sensors are used with a standard calibration curve. Temperatures below 50 K are measured using Lakeshore Cernox 1050SD sensors, which have a calibration error of 0.25 K [33] and a long-term stability of 12 mK at 20 K [37]. The readout of all temperature sensors is done using Lakeshore 218S temperature monitors and a four-wire measurement technique.

In addition to the temperature sensors six heaters are distributed on the liner, four in the cold section and one in each warm section. They allow to calibrate the measured temperature at the cooling connection to the beam heat load by simulating the heat intake from the beam.

Each heater is 10 mm wide, 120 mm long and can provide up to 7.5 W of heating power. They are controlled by TTI power supplies and the applied heating power is obtained with a Keithley 2700 multimeter by measuring the voltage drop across the heater with a four-wire technique.

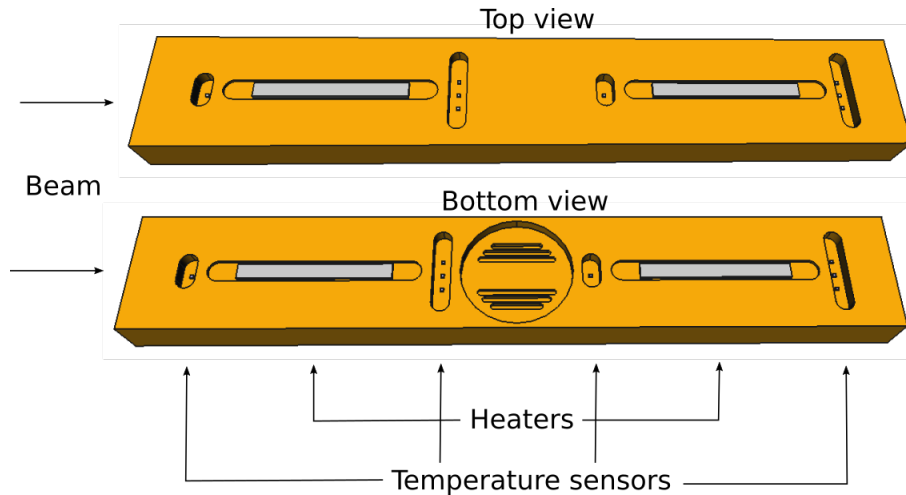


Figure 3.9: Positions of the temperature sensors and heaters on the cold liner.

Retarding field analysers

A retarding field analyser (RFA) at the top of the diagnostic port in each section allows to measure the total flux and energy spectrum of low energy charged particles hitting the chamber walls. It consists of a tungsten mesh acting as the grid and a detector plate as collector. It covers three of the slots in the beam tube (see Figure 3.5). The collector can be biased with a positive or negative voltage up to 60 V to measure the flux of negatively or positively charged particles, respectively. With the grid against ground the total flux of charged particles is measured. Additionally the grid can be used to apply a retarding voltage up to 250 V (polarity opposite to the collector), in order to measure the energy spectrum of the charged particles hitting the collector.

Two readout methods are implemented. One method uses a Keithley 6514 electrometer to measure the current created by the particles hitting the collector plate. The other method uses a 7230 dual phase lock-in amplifier from Signal Recovery that measures the current on the collector phase locked to the modulated retarding voltage. While the first method can be used to directly determine the number of charged particles per unit time hitting the collector from the measured current, the second method has a better signal-to-noise ratio and allows to directly measure the energy spectrum [36].

A solenoid is wound around the downstream side of the cold section that can be used to reduce the number of charged particles hitting the cold liner, by creating a magnetic field parallel to the beam axis that transforms motion towards the liner surface into a helical path around the beam axis. The magnetic field on beam axis can reach around 5 mT to 10 mT for a current of 0.5 A to 1 A in the solenoid.

Pressure gauges and mass spectrometers

For the measurement of the pressure and gas content in each of the three diagnostic ports of COLDDIAG a MKS inverted magnetron cold cathode pressure gauge and a Pfeiffer Vacuum PrismaPlus QMG 220 compact mass spectrometer for residual gas analysis (RGA) are installed.

The RGA can measure the mass spectrum from 0 u to 100 u and uses a continuous secondary electron multiplier (C-SEM) detector that reaches a detection threshold of 1×10^{-14} mbar. The accuracy of the peak ratio is 0.5%.

3.2.4 Control for constant liner temperature measurements

During the measurements at the Diamond Light Source a new procedure for an improved beam heat load measurement was developed in the framework of this thesis. Instead of letting the cold liner gradually be heated up by the beam and calibrating the heat load to the corresponding liner temperature with the liner heaters, the heaters are used during the beam heat load measurement to keep the liner at a constant temperature (e.g. 20 K). In this way the system needs less time to stabilize and the beam heat load can be read directly from the power to the liner heaters. Furthermore it is possible to measure the beam heat load not only for a specific liner temperature but also as a function of the liner temperature.

In order to keep the liner temperature constant a PID (Proportional-Integral-Derivative) control loop was added to the control system, with the process variable being the liner temperature and the control variable being the current in the heaters. After a specified time intervall (5 s was found to give the best result) the controller determines the difference between the setpoint of the liner temperature and the measured temperature, and changes the current in the heaters according to the PID parameters. The part of the control system containing the implementation of the PID control loop is shown in Figure 3.10.

The determination of suitable PID parameters was done based on the Ziegler-Nichols method [38], with the aim of accepting some overshoot of the temperature to get a fast settling time. First the control is set to proportional only (PID parameters: $K_p = P$, $K_i = 0$, $K_d = 0$) and the system is brought out of equilibrium by changing the setpoint of the liner temperature. The heating power H for each iteration is given by:

$$H = K_p \cdot |T_{target} - T_0| \quad , \quad (3.1)$$

where T_{target} is the target temperature and T_0 is the current temperature.

This results in an oscillation which is damped, stable or unstable, depending on the value

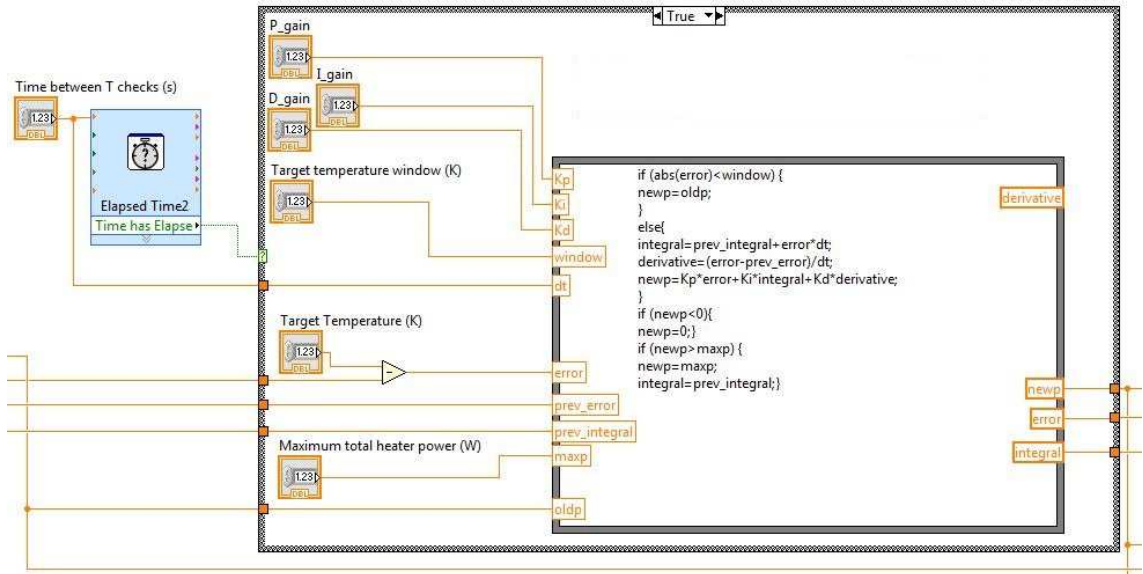


Figure 3.10: PID control loop in the COLDDIAG LabVIEW control system.

of K_p . Then K_p is adjusted to a value P for which the oscillation is stable, i.e. it has a constant amplitude. This value of P and the periodic time of the oscillation t_{osc} is noted. With these two values the PID parameters can be calculated according to the Ziegler-Nichols method:

$$K_p = 0.6 \cdot P \quad , \quad K_i = 2/t_{osc} \quad , \quad K_d = t_{osc}/8 \quad (3.2)$$

The numbers obtained from the oscillation were $P = 10$ and $t_{osc} = 95$ seconds. The calculated PID parameters had to be adjusted for the integral and derivative part, resulting in the following set of parameters:

$$K_p = 6 \quad , \quad K_i = 0.21 \quad , \quad K_d = 119 \quad (3.3)$$

This PID tuning leads to the control behaviour shown in Figure 3.11. After activating the PID control loop at 13.4 K liner temperature it manages to increase the temperature to 20 K and damp the oscillation in about 10 minutes. The top-up of the beam current at 01:12 shows that the time needed to reach a stable heating power within 0.1 W is reduced even more if the change in temperature or heat load is small.

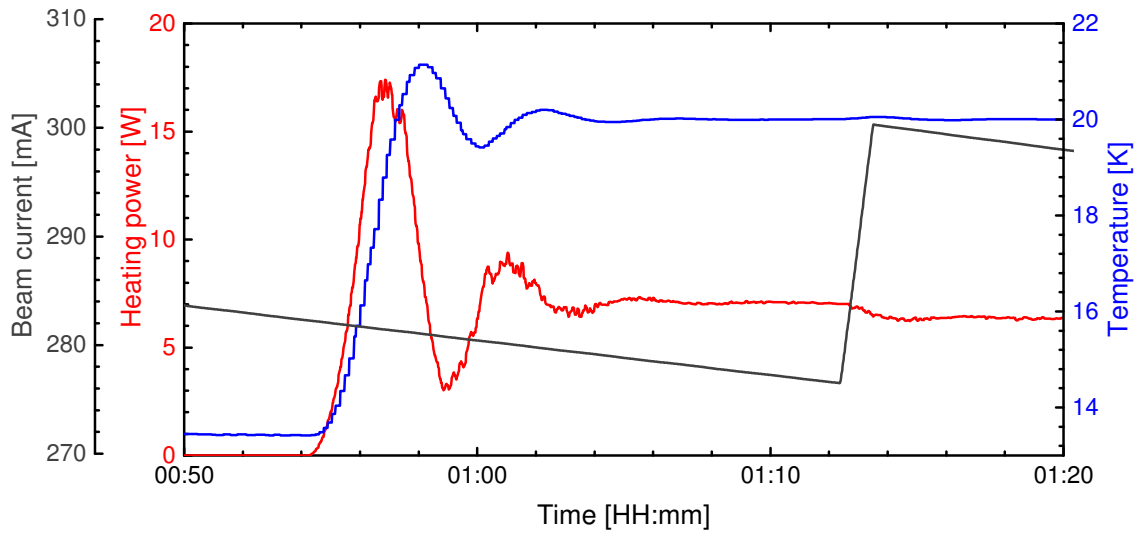


Figure 3.11: Test of the PID parameters $K_p = 6$, $K_i = 0.21$, $K_d = 119$ with beam in top-up mode. The control is switched on at 00:54.

3.2.5 Offline calibration

With the ability to keep the liner temperature constant it became clear that the measured beam heat load has a strong correlation with the temperatures at the thermal transitions from the 50 K shield to the cold liner. The best situation to observe this is directly after a beam dump (see Figure 3.12).

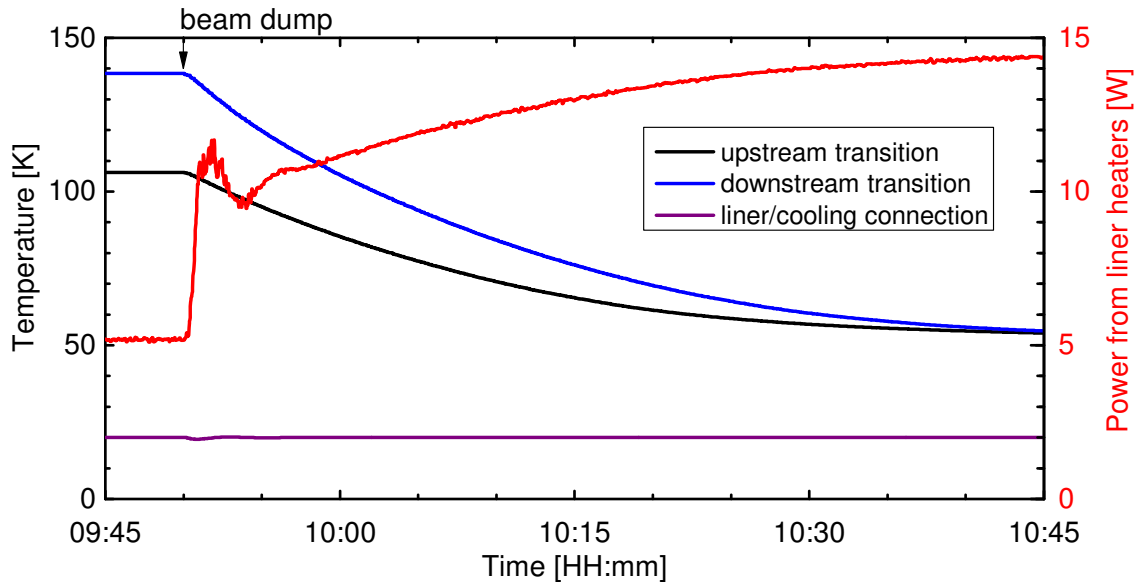


Figure 3.12: Beam dump at 300 mA, 900 bunches with the liner temperature controlled to 20 K.

At the beam dump there is a sudden step up in the heating power from the liner heaters, which is equivalent to less beam heat load. But in the hour after the beam dump the heating power from the liner heaters continues to rise slowly, while the temperature at the upstream and downstream thermal transition goes down in a similar way.

This leads to the conclusion that only the initial step in heating power can be attributed to direct heat load from the beam to the cold liner and the remaining part is in fact heating through conduction over the thermal transitions. In order to remove the latter contribution from the measured beam heat load two additional heaters are needed, one at the warm side of each thermal transition (see Figure 3.13).

In principle the two heaters can be used to control the temperature of the thermal transitions during a measurement, but they could be installed only after the removal of COLDDIAG from the DLS storage ring. At that point an offline calibration was done, where the temperatures at the thermal transitions and at the liner were reproduced without beam for each measurement. The calibration procedure is explained in more detail in Section 4.1.1.

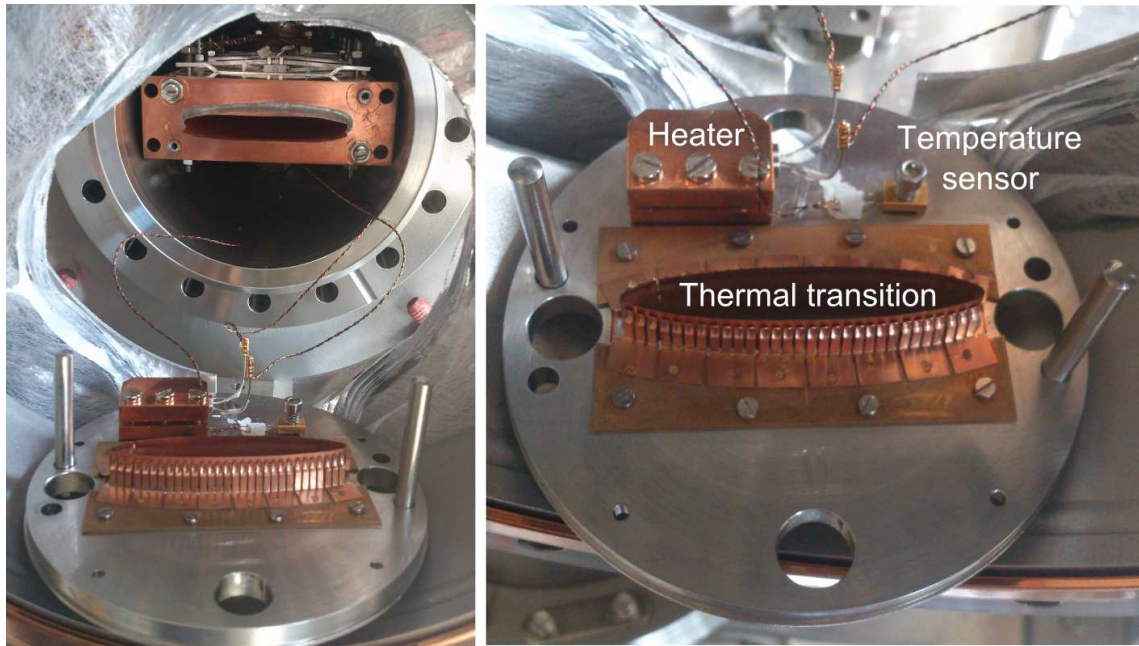


Figure 3.13: Calibration heater at the thermal transition from the 50 K shield to the cold liner.

3.3 Longitudinal wire method for impedance determination

After COLDDIAG has been removed from the Diamond Light Source storage ring and the offline calibration has been performed it became clear that further investigations were necessary in order to find the source of the measured beam heat load. The measurement of the longitudinal beam coupling impedance through network analysis was chosen as the next step.

The classic approach to measuring the beam impedance is the coaxial wire method [39, 40]. To simulate the electromagnetic fields generated by the beam, the beam chamber is converted into a TEM (transverse electromagnetic) line by introducing a coaxial wire. The real part of the longitudinal impedance can be measured directly with a network analyzer. The disadvantages of this technique are the low sensitivity for small impedances in the few Ω region and the need for matching sections at the ends of the structure, because the characteristic impedance and the shape of the beam pipe has to be matched to the 50Ω coaxial cable of the network analyzer. Since in our case the beam chamber cross section is elliptic, the tapering of the matching section to the coaxial cable would introduce additional errors due to the complicated shape. Furthermore the reproducibility would be reduced, because matching sections are more susceptible to adjustment errors than capacitive coupling.

Therefore the resonator method for impedance determination [41, 28] is used. Its implementation is described in the following.

3.3.1 Resonator method

A device-under-test (DUT), for instance a reference tube or the COLDDIAG liner, is transformed into a resonator (see Figure 3.14) by closing the ends with copper end plates, either integrated into a flange or pressed directly against the ends. The (coaxial) measurement cables are connected through a SMA-pin-connector in each end plate, which couples into the resonator through a 3 mm pin (copper beryllium with $50\ \mu\text{m}$ gold finish, 1.3 mm diameter) at the end of the coaxial feedthrough. The isolation material inside the connector is teflon. Inside the DUT a copper rod (3.2 mm diameter, 99.9% purity) is centered to create a TEM line resonator. The centering is done using support pieces made from teflon, the same material used inside the connectors. Its influence on the resistive part of the impedance is negligible. The length of the inner conductor is chosen in such a way that the coupling gap to the connector pin is 6 mm on each side. This value allows for an acceptable signal-to-noise ratio at low frequencies, where the noise floor is at $-120\ \text{dB}$, while the coupling at high frequencies is still small enough to meet the requirement of weak coupling (see Section 2.3.3).

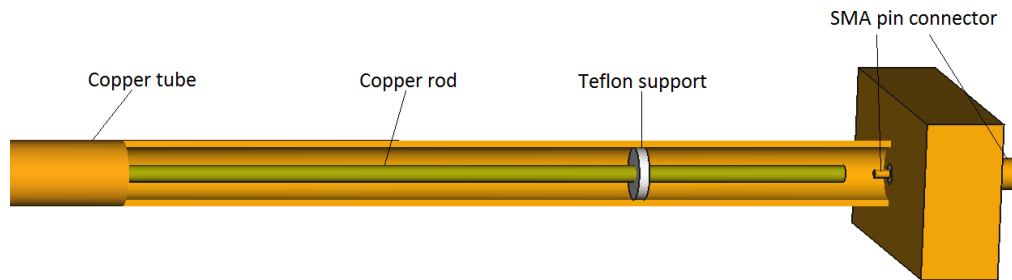


Figure 3.14: Basic setup of the resonator method impedance determination. A cut through the outer conductor (copper tube) shows the teflon support and capacitive coupling at one end of the resonator.

3.3.2 Vector network analyzer

For the measurements a 2-port vector network analyzer (Anritsu ShockLine™MS46322A) was used. A manual Short-Open-Load-Through (SOLT) calibration was applied, including a 3 m SMA cable (Subminiature version A connectors) connected to a 0.6 m SMK test port cable (2.92 mm or K type connector) at each port. The following frequency sweep settings were used:

- 16001 measurements points
- 100 Hz IFBW (interfrequency bandwidth)
- Averaging OFF
- Interpolation ON

3.3.3 Reference measurements

The measurement procedure has been validated using a simple coaxial TEM line made from a copper tube (10.26 mm inner diameter, 503 mm length, 99.9 % purity) for the outer conductor and a copper rod (3.2 mm diameter, 485 mm length, 99.9 % purity) for the inner conductor (left side in Figure 3.15). For this setup the expected resistive wall impedance due to the outer conductor can be calculated analytically using Equation 2.39 and inserting the attenuation due to the outer conductor α_{oc} , replacing the inner diameter d with the

outer diameter D in Equation 2.38:

$$\operatorname{Re}(Z) \left[\frac{\Omega}{m} \right] = 2Z_L \cdot \alpha_{oc} = 120 \Omega \cdot \sqrt{\pi \rho_{oc} \varepsilon f_{res}} \frac{1}{D} \quad (3.4)$$

Since the COLDDIAG liner has an elliptical cross section, its characteristic impedance Z_L deviates from that of a circular pipe. Therefore an additional reference measurement has been performed on a copper chamber with the same cross section and length of a COLDDIAG warm part (270 mm). It is made from the same material as the liner and the ellipse has been eroded with a similar surface roughness of $R_a = 3.6 \mu\text{m}$. The difference to the warm part (Figure 3.16) is that it is not electroplated with an additional copper layer and there are no pumping slots (right side in Figure 3.15).

3.3.4 Measurements on COLDDIAG

Impedance measurements have been performed on the following parts of the COLDDIAG structure:

- 270 mm warm section
- 490 mm cold section
- 554 mm cold section with thermal transitions to the 50 K shield
- 850 mm cold section with thermal transitions and finger bellows between 50 K shield and warm sections (Figure 3.17)

A comparison between those measurements and the reference measurements allows to identify specific sources of impedance, i.e. skin effect, surface roughness, flange cavities, step transitions and slots.

The results of those measurements are discussed in Chapter 5.

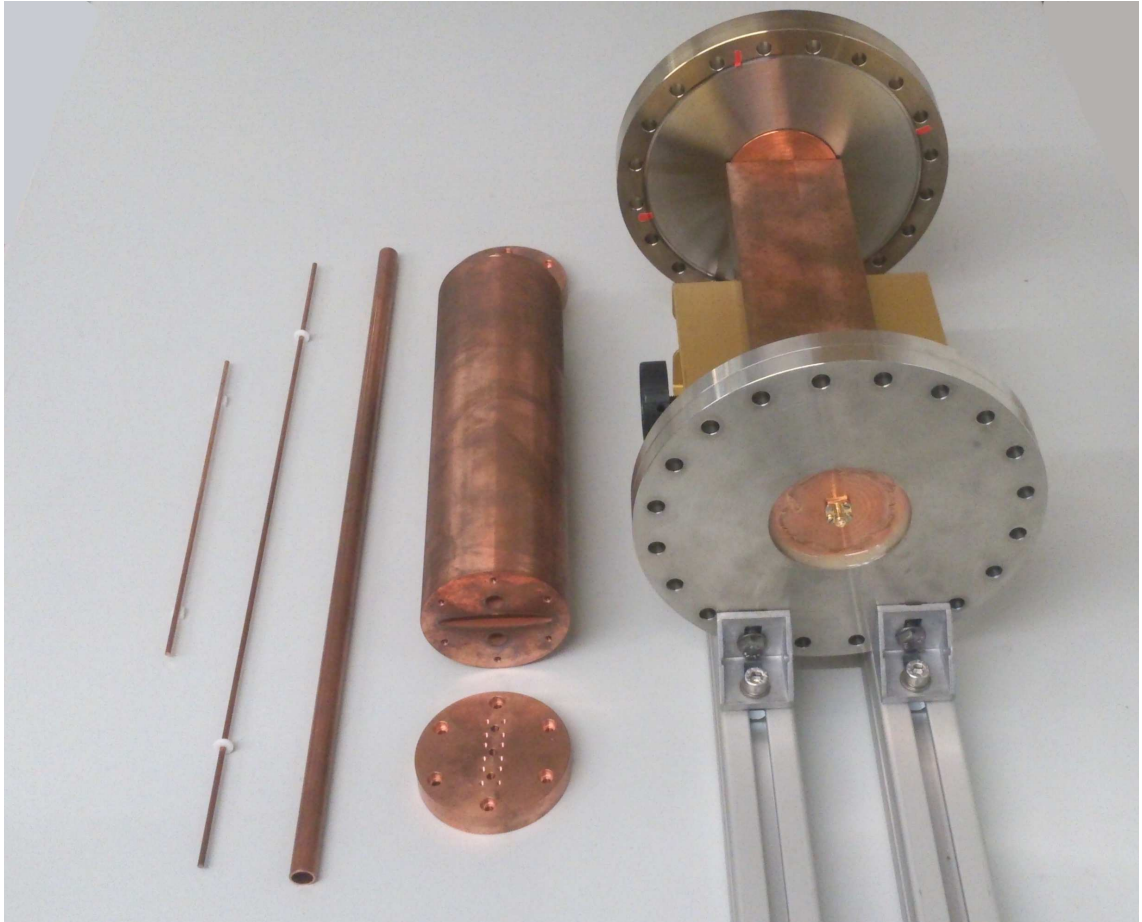


Figure 3.15: Test chambers used for reference measurements. From left to right: inner conductors made from a copper rod, drawn round copper pipe and eroded elliptical copper chamber, fixing mechanism for the reference measurements.

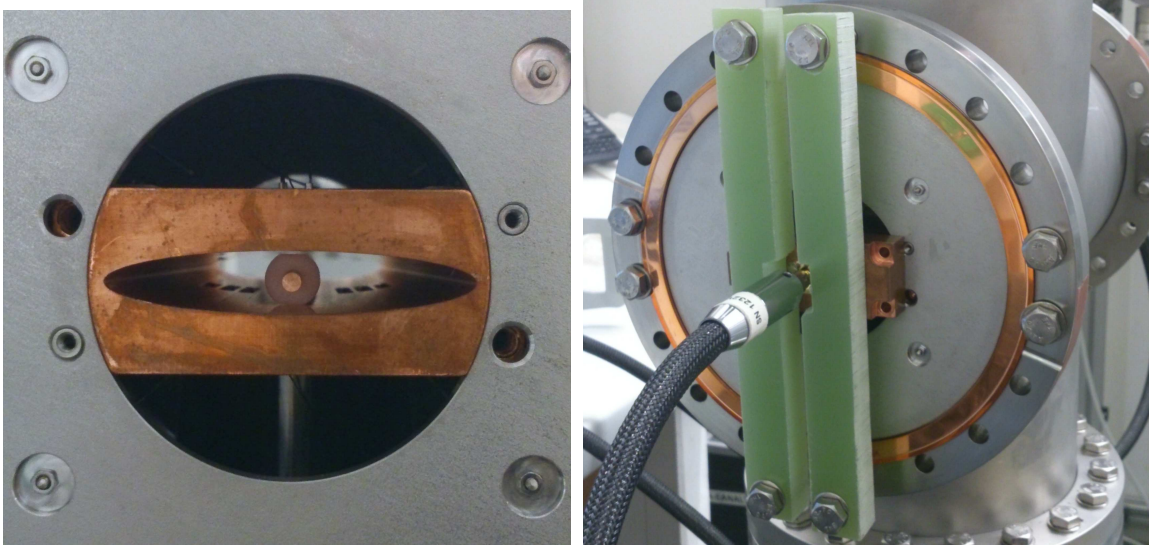


Figure 3.16: Setup for the impedance measurement on a COLDDIAG warm section. Left: alignment of the inner conductor. Right: fixing mechanism for the end plates.

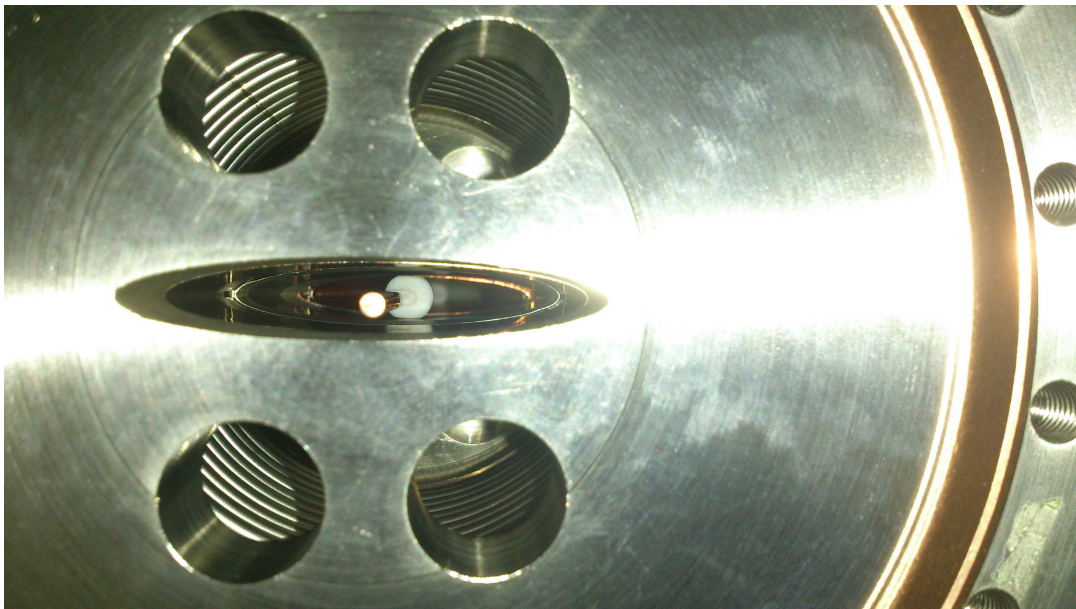


Figure 3.17: Alignment of the inner conductor for a impedance measurement on the COLD-DIAG cold part including thermal transition and bellows.

CHAPTER 4

Measurements with COLDDIAG at the Diamond Light Source (DLS)

COLDDIAG was installed in the DLS storage ring from September 2012 to August 2013. During this period measurements were performed for a wide range of machine conditions, employing the various measuring capabilities of the device. In this chapter the analysis of the measured beam heat load, pressure and gas content, as well as the low energy charged particle flux and spectrum, as a function of the electron beam parameters (i.e. bunch charge, number of bunches, bunch length and bunch spacing) and COLDDIAG parameters (i.e. liner temperature and solenoid field) is presented.

4.1 Beam heat load

The beam heat load discussed in the following refers to the heat load that was measured with the cold liner at a fixed temperature, using the temperature sensor at the cooling connection for the PID control of the liner heaters. The second approach to measure the beam heat load, i.e. letting the liner warm up by the increasing beam current, gives comparable results, but has the intrinsic disadvantage of an uncontrolled liner temperature and a longer measuring time. The measured beam heat load is corrected by removing the influence of the thermal transition through offline calibration, to get the direct beam heat load from the electron beam on the cold liner.

4.1.1 Calibration

The calibration of the beam heat load was done in an offline experiment after the removal of COLDDIAG from the DLS. Additional heaters have been mounted at the thermal transitions (Section 3.2.5) to simulate the heat flow through the thermal transitions to the cold liner. The upper part of Figure 4.1 shows an example of a beam heat load measurement, where the temperature of the cooling connection from the cryocooler to

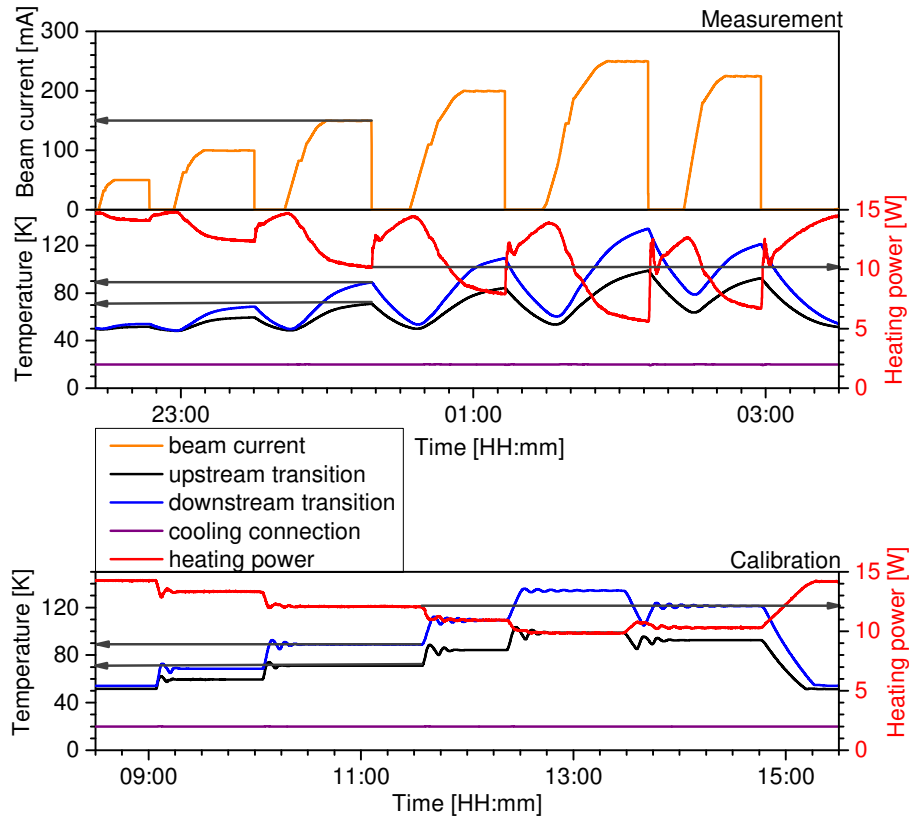


Figure 4.1: Example for the beam heat load calibration with the liner temperature fixed at 20 K. The upper part shows a measurement with 460 bunches and 6 beam current steps, and the lower part the corresponding offline calibration. Arrows indicate the relevant points for the beam heat load determination at 150 mA beam current.

the cold liner is kept at a constant temperature (20 K) during the measurement. The different beam current steps result in given temperatures at the upstream and downstream transition and in a given heating power to the liner heaters, which is necessary to keep the liner at a constant temperature. In the corresponding calibration (lower part of Figure 4.1) the temperatures at the upstream and downstream thermal transition are reproduced using the heaters installed at the flanges connecting the transitions to the 50 K shield (Section 3.2.5). The temperature at the cooling connection is reproduced by the liner heaters and results in a higher heating power than during the measurement because of the absence of beam heating. The difference between the two heating powers is therefore the beam heat load. The error on the beam heat load is estimated to be within 0.1 W. It is primarily coming from the readout of the heating power to the liner heaters during the measurement, which shows a small oscillation because of the PID control and is slowly decreasing due to the slow thermalization of the cryostat.

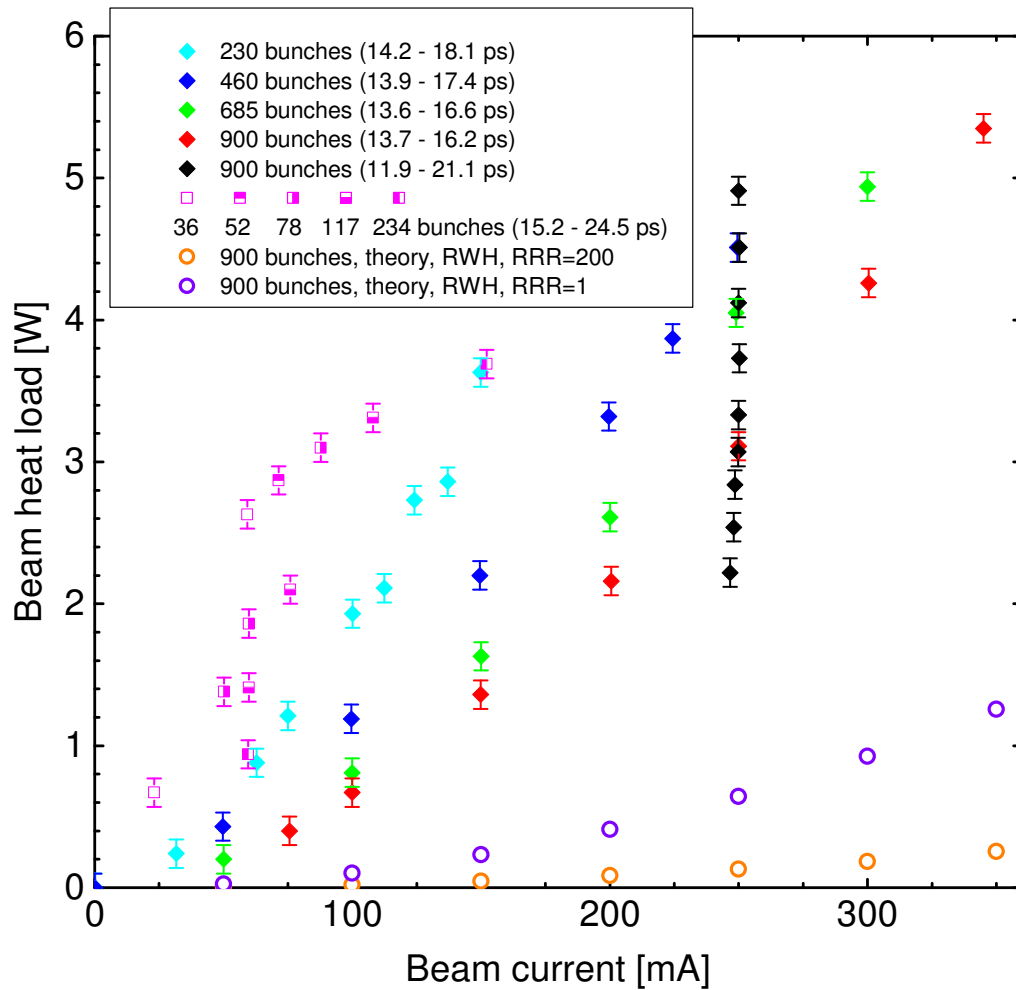


Figure 4.2: Beam heat load as a function of beam current for a wide range of beam parameters. Included are measurements for 4 beam current ramps with a certain number of bunches in one train (cyan, blue, green, red), beam current steps for filling patterns with equally distributed bunches (magenta) and a measurement with everything fixed except the bunch length (black). The theoretical values for resistive wall heating are indicated with circles, for a bunch length of 14.54 ps.

4.1.2 Measurements

The aim of the following analysis is to find the dependence of the beam heat load on the different relevant beam parameters and compare it to existing beam heat load models. As an overview in Figure 4.2 the beam heat load is shown as a function of the average electron beam current. The different colours refer to individual measurements, each with its respective beam parameter ranges as indicated in the legend. Additionally, the theoretical values for resistive wall heating are shown for two different purities of copper, high purity copper with a RRR of 200 and low quality copper with a RRR of 1, and compared to the

measured values they are smaller by a factor of about 5 and 20, respectively. It can be readily seen that the bunch length has a great impact on the beam heat load (see black diamonds in Figure 4.2) and that for the same beam current the beam heat load increases with a decreasing number of bunches (higher bunch charge), as for example at 150 mA the heat load for 230 bunches is about 3 times higher than the heat load for 900 bunches.

4.1.3 Bunch length

To explore the effect of the bunch length on the beam heat load a dedicated measurement has been done, in which the filling pattern was kept the same (250 mA beam current, 900 bunches) and the bunch length was changed by varying the accelerating voltage in the RF cavities of the storage ring (see section 2.1). In this way the bunch length is the only changing beam parameter; its impact on the beam heat load is quite significant (see Figure 4.3). For beam heating due to RF effects P one expects different dependencies on the bunch length σ , depending on the particular effect: $P \propto \sigma^{-1}$ for step transitions, $P \propto \sigma^{-3/2}$ for resistive wall heating, $P \propto \sigma^{-5/3}$ for resistive wall heating in the anomalous regime and $P \propto \exp(-(2\pi f_r \sigma)^2)$ for a broad Gaussian impedance (see Section 2.2). The best fit for the measured data is given by a bunch length dependence of approximately $P \propto \sigma^{-1.4}$ or by a mixture of heating from step transitions and resistive wall heating:

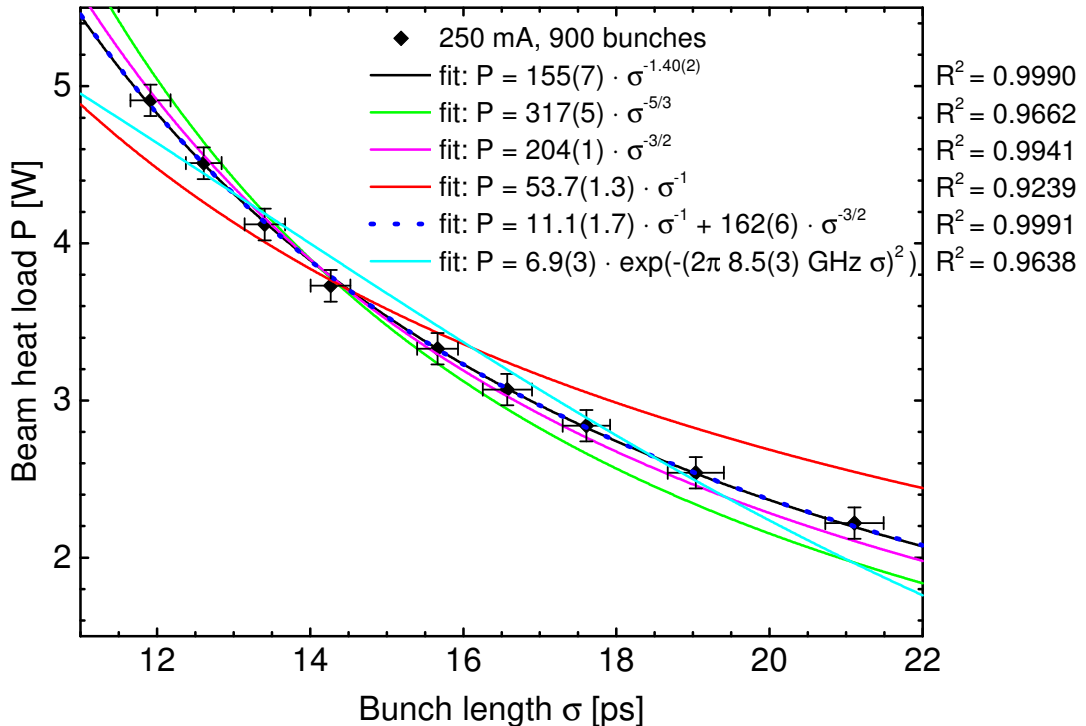


Figure 4.3: Beam heat load as a function of bunch length for a filling pattern of 250 mA beam current in 900 consecutive bunches. Fits to the data corresponding to the best fit using a power law and four different RF effects are shown. R^2 is the adjusted coefficient of determination.

$$P_{empirical}[\text{W}] = 155 \cdot \sigma[\text{ps}]^{-1.4} \quad (4.1)$$

$$P_{mix}[\text{W}] = 11.1 \cdot \sigma[\text{ps}] + 162 \cdot \sigma[\text{ps}]^{-3/2} \quad (4.2)$$

The model for beam heating due to a broad Gaussian resonance does not fit to the data. For beam heating due to synchrotron radiation one expects no dependence on the bunch length (section 2.2), which is clearly not the case. Beam heating from electron bombardment would fit to the general trend of higher beam heat load with shorter bunch length, however the exact dependence is not defined since the underlying beam dynamics is unknown. Thus, beam heating due to electron bombardment cannot be confirmed nor excluded by these observations.

4.1.4 Bunch spacing and number of bunches

Figure 4.4 shows the beam heat load as a function of the number of bunches. Each color stands for a fixed bunch charge and a fixed bunch length. Additionally, the bunch spacing has been varied; the red, green and blue points are taken from four different beam current ramps, where the bunches are consecutive in one train with a bunch spacing of 2 ns and a gap of 72 ns, 502 ns, 952 ns and 1412 ns at the end of the train for the filling pattern with 900, 685, 460 and 230 bunches, respectively. The cyan points are taken from a measurement where the bunch spacing was varied from 8 ns to 52 ns by distributing the bunches equally along the storage ring.

The best fit to the data using a power law gives an exponent varying between 0.88 and 0.95. A linear dependence, which is expected for broad-band RF effects and synchrotron radiation (Section 2.2.2), is shown as dashed lines. Such a dependence implies that the heating from separate bunches is independent and can be treated separately. According to the adjusted R^2 value, this model shows the best representation of the data. An exponent smaller than 1 is not consistent with any known theory. Heating from sharp RF resonances would show a quadratic dependence on the number of bunches (Section 2.2.2) and can be excluded on the basis of this plot.

The effect of the bunch spacing can be seen by comparing the cyan points, where the bunch spacing is varied, with the rest of the measurements. The fact that the dependence on the number of bunches is similar in all cases indicates that the bunch spacing has no influence on the beam heat load. Another strong evidence for that can be found in Figure 4.2. There the beam heat load for 230 bunches with the standard bunch spacing (cyan points) and for 234 bunches with equally spaced bunches (pink) is almost the same for the two beam currents 60 mA and 150 mA.

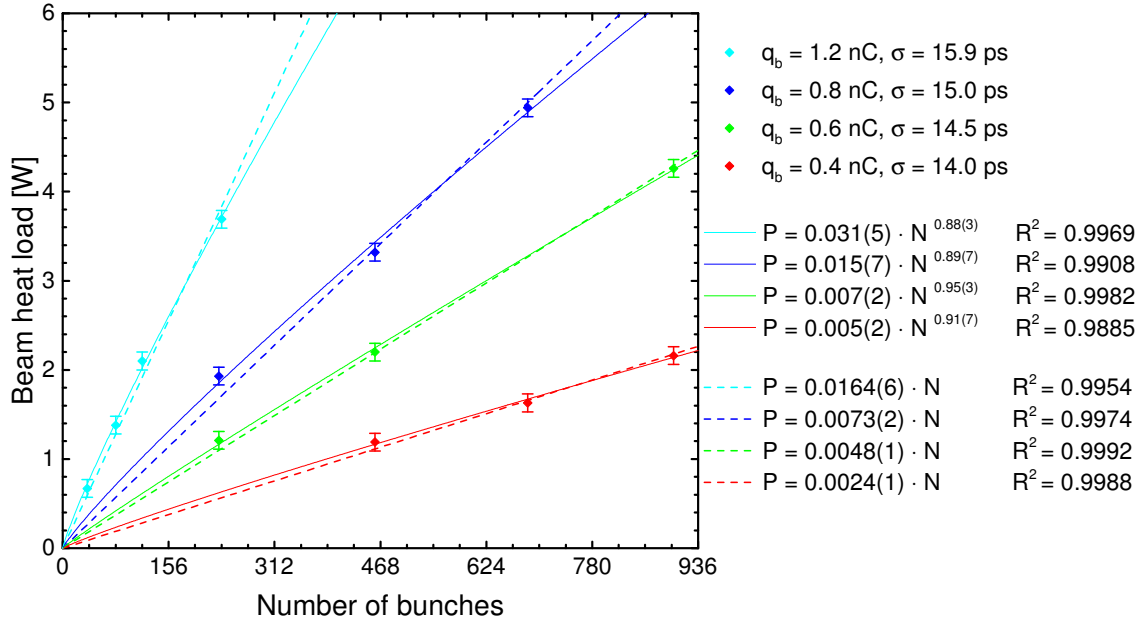


Figure 4.4: Beam heat load as a function of the number of bunches for four different bunch charges. For each set a linear and a power law fit through the origin is shown. R^2 is the adjusted coefficient of determination.

4.1.5 Bunch charge

Assuming a defined dependence on the bunch length and the number of bunches, which is based on the previous findings, the dependence on the bunch charge can be studied. The two models used here are the empirical model (Figure 4.5) and the resistive wall heat load model (Figure 4.6).

The empirical model assumes a bunch length dependence of $P \propto \sigma^{-1.4}$ and a dependence on the number of bunches of $P \propto N^{-0.9}$ as derived in the last two sections by the best fit. Three functions are tested for the bunch charge dependence, a simple power law (black line) and a parabola with (blue line) and without (red line) a linear part. The power law is purely empirical, the quadratic part corresponds to heating due to RF effects and the linear part to heating due to synchrotron radiation, even if the dependence on N should be linear for the non-empirical models.

The resistive wall heating model for a chamber with $RRR < 7$ [2] assumes a bunch length dependence of $P \propto \sigma^{-1.5}$ and a dependence on the number of bunches of $P \propto N^{-1}$. The same three fit functions are used as in the first case.

The fits are generally better at low bunch charges, because there most of the measurements were taken. For the empirical model the power law and the combination of linear and quadratic bunch charge dependence give a similar good fit, while the purely quadratic formula is fitting slightly worse. It has however just one fit parameter instead of two.

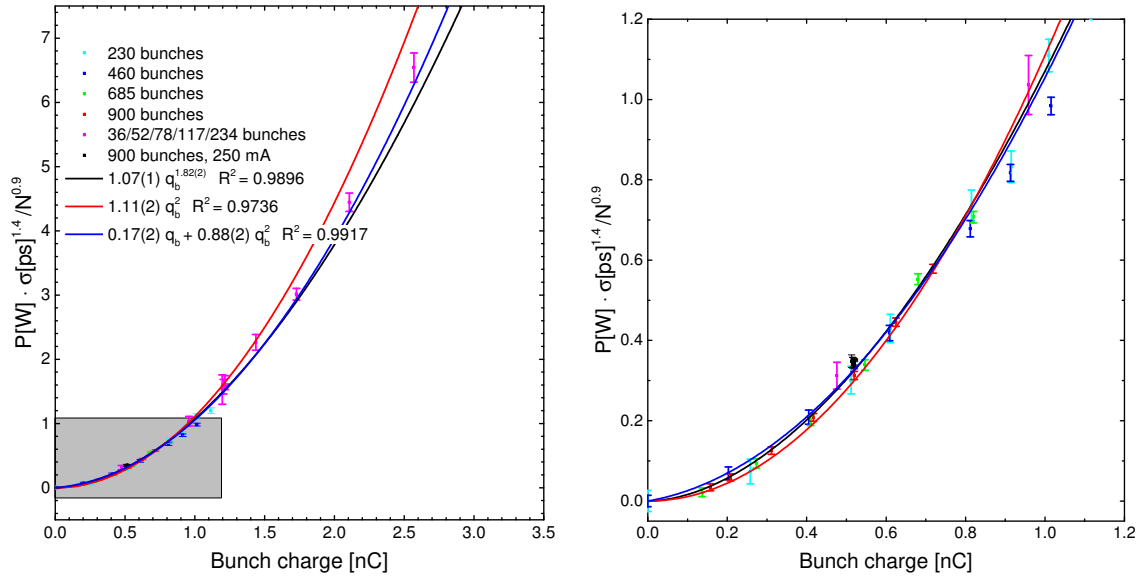


Figure 4.5: Beam heat load as a function of bunch charge, modified by the dependence on bunch length and number of bunches from the best fit. On the right plot is shown the area marked in grey in the left plot.

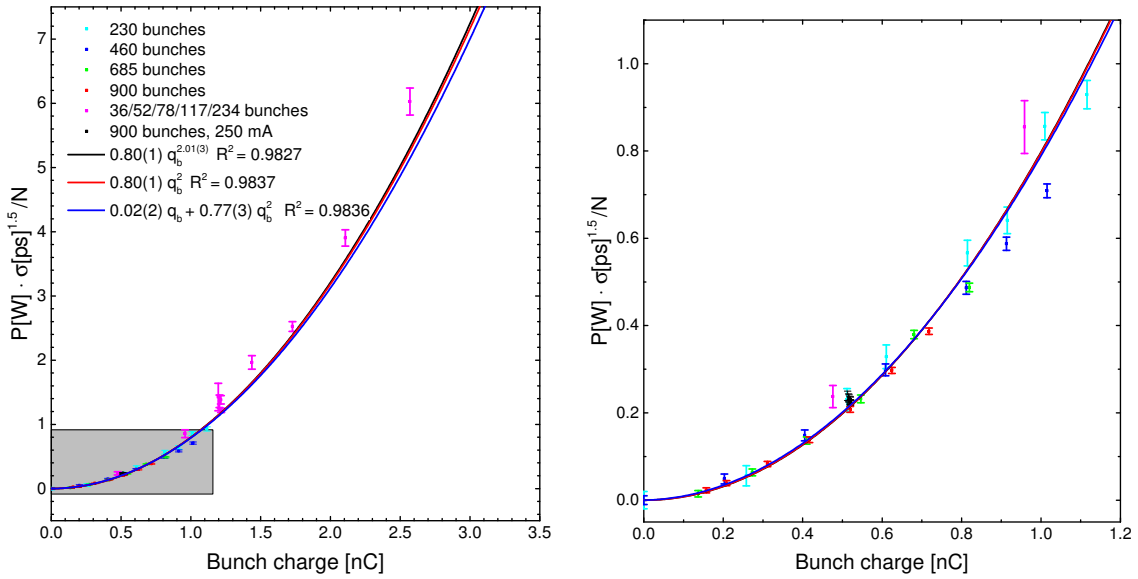


Figure 4.6: Beam heat load as a function of bunch charge, modified by the dependence on bunch length and number of bunches according to resistive wall heating. On the right plot is shown the area marked in grey in the left plot.

For the resistive wall heating model the quadratic bunch charge dependence already shows good agreement with the data. Therefore the other two fits do not differ from it. The exponent of the power law is almost 2 and the linear part in the third formula is much smaller than its quadratic part.

4.1.6 Heat load models

Assuming different models, it is possible to plot the measured beam heat load to the predicted dependencies on the beam parameters q_b , N and σ , perform a linear fit and compare how the data fit to these models. In Figure 4.7(a) the measured beam heat load is plotted against a model, which is constructed from the empirical fit parameters derived in the previous sections, i.e. a bunch charge dependence of $P \propto q_b^{1.82}$, a dependence on the number of bunches of $P \propto N^{0.9}$ and a bunch length dependence of $P \propto \sigma^{-1.4}$. The other three models in Figure 4.7(b) to (d) represent heating due to resistive wall heating in the normal and anomalous regime and due to step transitions, respectively (Section 2.2.2). A linear fit is done for each case to test the validity of the model.

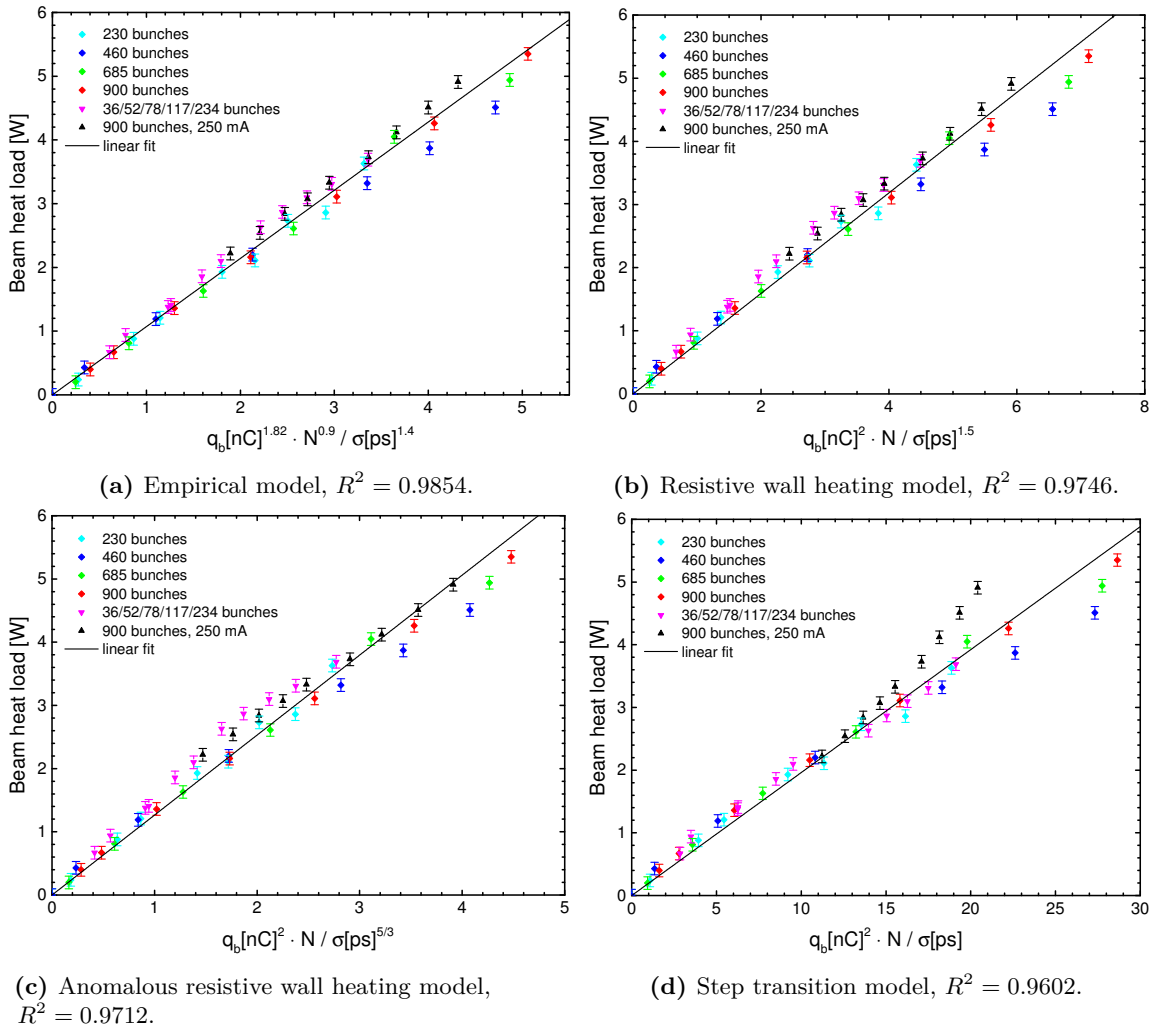


Figure 4.7: Comparison of the beam heat load model, derived from the measurements, with three different RF effect models.

Compared by the adjusted R^2 value the best fit to the data is given by the empirical model. The two resistive wall heating models show both less agreement with the data than the empirical model, with the anomalous resistive wall heating model deviating from the data more in the center. The step transition model shows the least agreement, especially for the measurement with different bunch lengths for the same filling pattern (black points in Figure 4.7(d)).

4.1.7 Liner temperature

Since the liner temperature at the cooling connection can be fixed to given values, it is possible to measure the beam heat load at different liner temperatures. One limitation is the amount of current that the wires of the liner heaters can carry. To overcome this limit the cartridge heaters at the cold stage of the cryocooler can be used to raise the base temperature, and the heaters on the liner are used for the temperature control. The beam heat loads in Figure 4.8 were measured in this way with a fixed filling pattern (900 bunches, 300 mA) and a fixed heating power at the cold stage between 0 W and 12 W. An overall increase in beam heat load with liner temperature can be observed, which is irregular and shows a local minimum between 28 K and 30 K. A pressure change is not visible during the measurement and the gas composition shows only a small change at 30 K, where mainly the partial pressure with mass 28 u increases by about 50% (see Section 4.2).

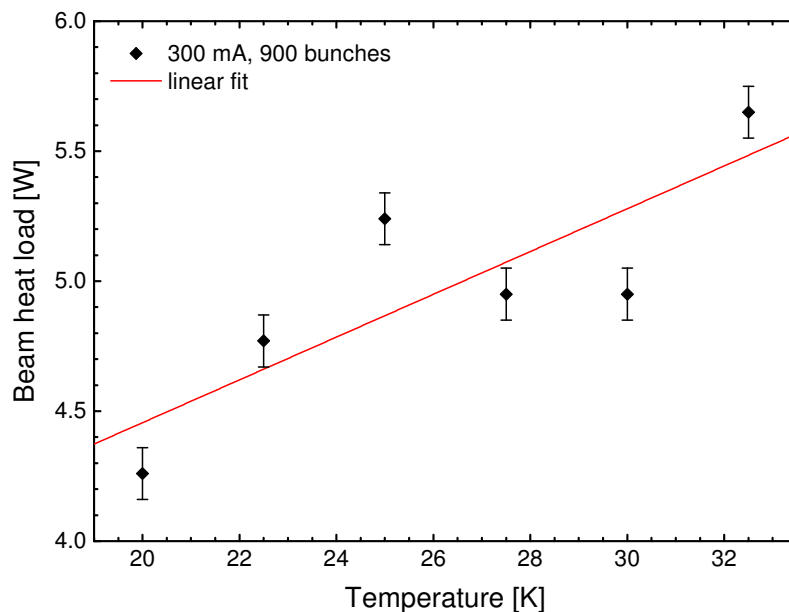


Figure 4.8: Beam heat load as a function of the liner temperature at the cooling connection for a fixed filling pattern (300 mA, 900 bunches). The error is estimated to be 0.1 W.

4.1.8 Warm sections

Using the warm sections of COLDDIAG it is also possible to measure the beam heat load at room temperature. Since there is no active cooling in the warm sections the time to reach thermal equilibrium is much longer than in the cold section (1 to 2 days). Therefore it is not possible to measure the beam heat load at a constant temperature. For the same reason data from dedicated measurement sessions can not be used, but only the ones taken during user operation, where the same filling pattern is usually kept for several days.

The downstream warm section had thermal contact with the cryostat, which lead to a constant temperature in this section (independent of the heat load), preventing the beam heat load determination. The calibration of the upstream warm section is done with the heater on the liner, by heating without beam to the temperature that was measured with beam and reading the power to the heater. In this case the heat coming from the two transitions cannot be removed by a calibration, because there are no temperature sensors at the connecting flanges, and it is therefore included in the measurement.

When comparing the beam heat load in the warm section to the cold section one has to take into account the different lengths of the sections. While the cold section is 0.5 m long, the warm section is only 0.27 m long, and any beam heating effect scaling with length (e.g. resistive wall heating) will scale accordingly. The absolute and scaled beam heat load is shown in Figure 4.9 for the upstream warm section and compared to similar measurements in the cold section. The measured beam heat load in the warm section is 30 % to 40 % lower than in the cold, but when scaled by the length of the section it is 20 % to 30 % higher.

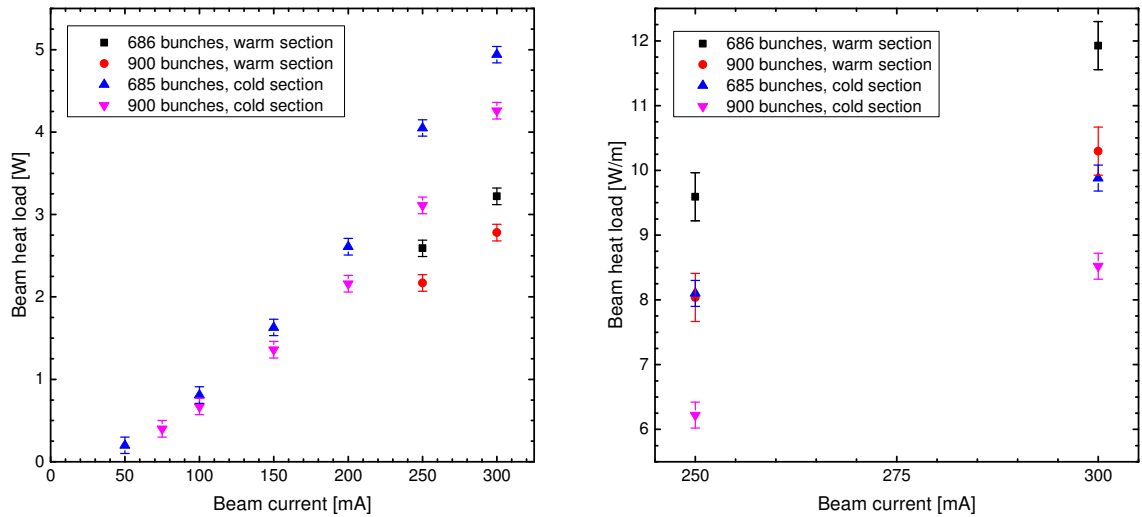


Figure 4.9: Comparison between the beam heat load in the warm and in the cold section. Left: measured beam heat load. Right: beam heat load scaled by the length of each section.

4.2 Pressure

In COLDDIAG the pressure can be measured in two ways. One is the measurement of the total pressure by using the pressure gauges in the three sections of COLDDIAG as well as at the upstream and downstream pumping station, and the other is the measurement of the partial pressures for the masses between 1 u and 100 u using the RGA in each diagnostic port.

The sensitivity of the pressure measurements is limited by outgassing in the diagnostic sections, where the pressure gauges and the RGAs are located. The measured pressure without beam is in the range between 6×10^{-10} mbar and 8×10^{-10} mbar.

4.2.1 Total pressure

The total pressure was measured with the liner temperature in the cold section kept at 20 K. When changing the beam current in the storage ring, the temperatures in the cryostat as well as the pressures undergo a dynamic change. Therefore the specific pressure values were taken after a waiting time of usually 15 to 30 minutes, which was needed for the beam heat load measurement anyway and allows the system to thermally stabilize and yields a value close to the equilibrium pressure.

Figures 4.10 and 4.11 show the total pressure as a function of beam current measured for different filling patterns, i.e. beam current ramps with 230, 460, 685 and 900 bunches in one train, several bunch spacings with the bunches distributed equally around the storage ring and different bunch lengths with an otherwise fixed filling pattern (250 mA, 900 bunches), achieved by changing the cavity voltages of the RF system.

In the two pumping stations before and after COLDDIAG (Figure 4.11) there is a more pronounced pressure increase with beam current compared to the other sections. The reason for this is that the absorber, which is protecting the COLDDIAG liner from direct synchrotron radiation, is located after the upstream pumping station. Therefore synchrotron radiation is hitting the beam tube in that section, producing a linear contribution through photodesorption to the pressure rise. In the downstream pumping station another taper is responsible for the same effect.

In COLDDIAG itself the pressure change is much less, especially at high beam currents, because these three sections are screened from direct synchrotron radiation. Since the base pressure is relatively high with 6×10^{-10} mbar to 8×10^{-10} mbar at 20 K liner temperature, the sensitivity of the pressure measurements is limited. The observed pressure change cannot be explained by the liner temperature, since in the cold section the heaters keep the liner temperature at 20 K, and in the warm sections the temperature change during a measurement session is below 1%. A possible explanation is thermal outgassing of the transitions from the cold liner to the 50 K shield, which get heated from below 40 K without

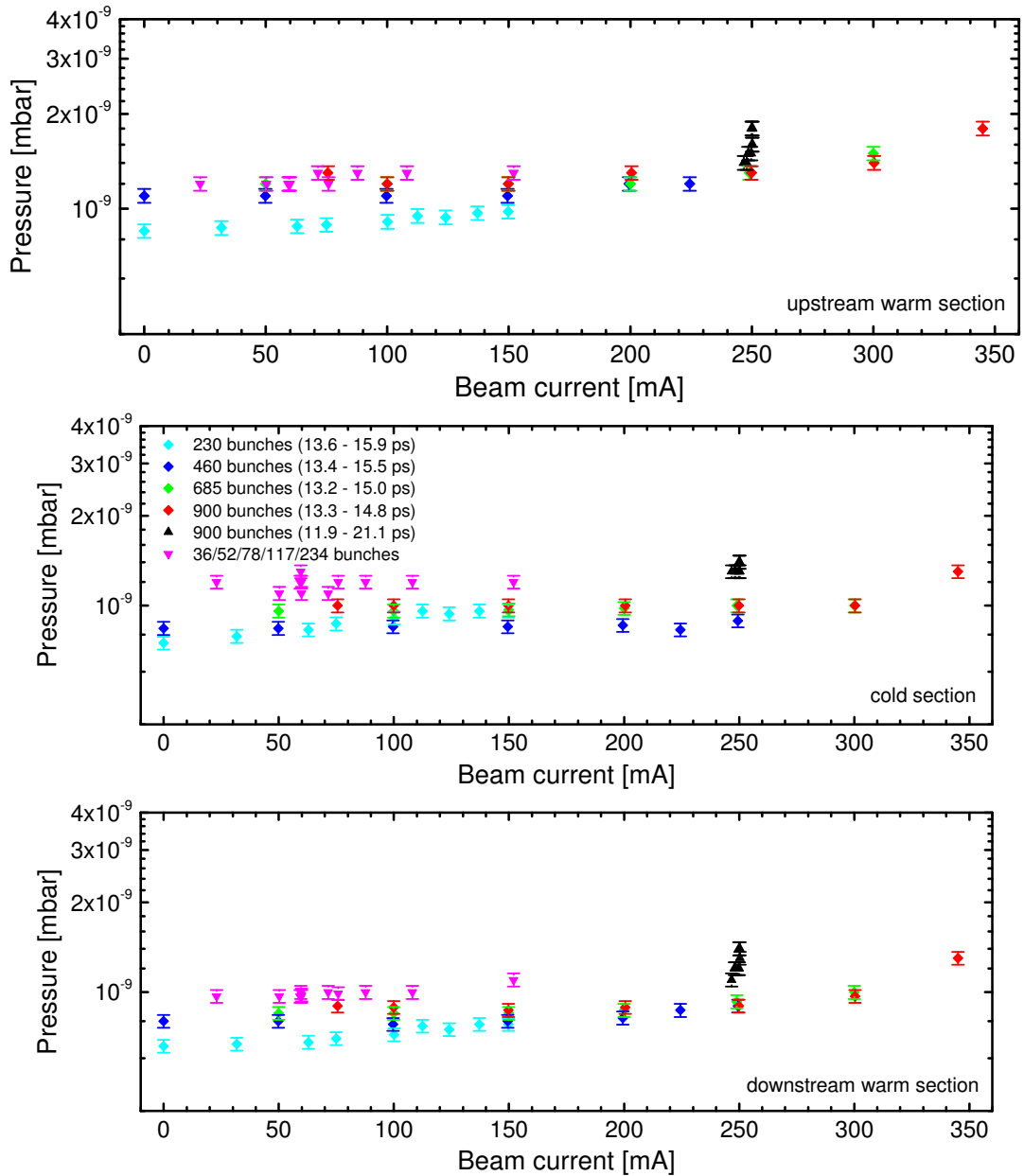
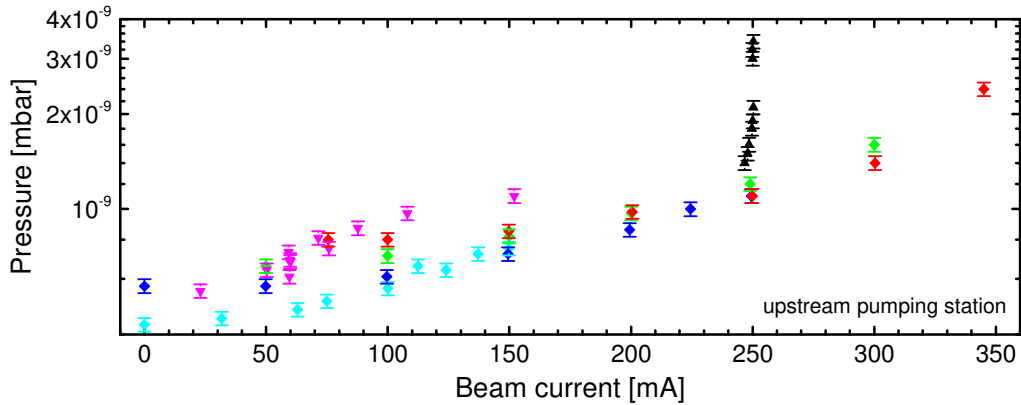
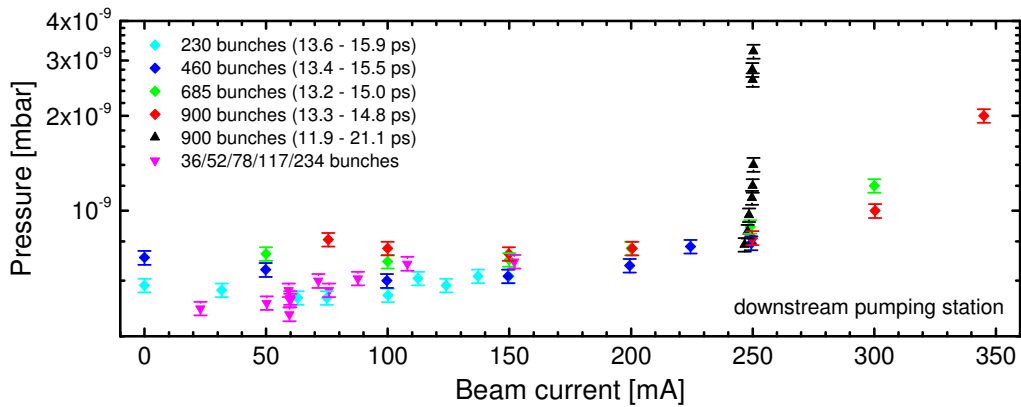


Figure 4.10: Total pressure as a function of beam current in the cold section and the two warm sections of COLDDIAG for several filling patterns. The reproducibility of the pressure reading is 5% [42].

beam to 170 K downstream and 130 K upstream, measured at the flange connected to the finger bellow, with 350 mA beam current. Another possibility is electron bombardment on the cold walls. However, due to the limited sensitivity of the pressure measurement it is not possible to draw conclusions.



(a) Upstream pumping station.



(b) Downstream pumping station.

Figure 4.11: Total pressure as a function of beam current in the two pumping stations before and after COLDDIAG for several filling patterns. The reproducibility of the pressure reading is 5% [42].

In order to get a picture of the dynamic pressure changes during beam injection and beam dump, in Figure 4.12 the total pressure over time is shown during several beam current steps with 230 consecutive bunches. In this case the pressure change is well visible, because the pressure stays below 1×10^{-9} mbar where the resolution of the gauge is better by one digit due to its logarithmic scale. During injection the pressure rises to a peak value and comes down to an equilibrium value after the injection. At the beam dump the pressure falls sharply and settles down to a value that is higher than the first dip but still lower than the value with beam. In the cold section this behaviour is much more pronounced than in the two warm sections. In the upstream pumping station the pressure rise and fall is much larger due to the direct synchrotron radiation. In the downstream pumping station the pressure rises when dumping the beam, which is not intuitive. A possible explanation is that the beam dump causes a vacuum spike at the downstream pumping station.

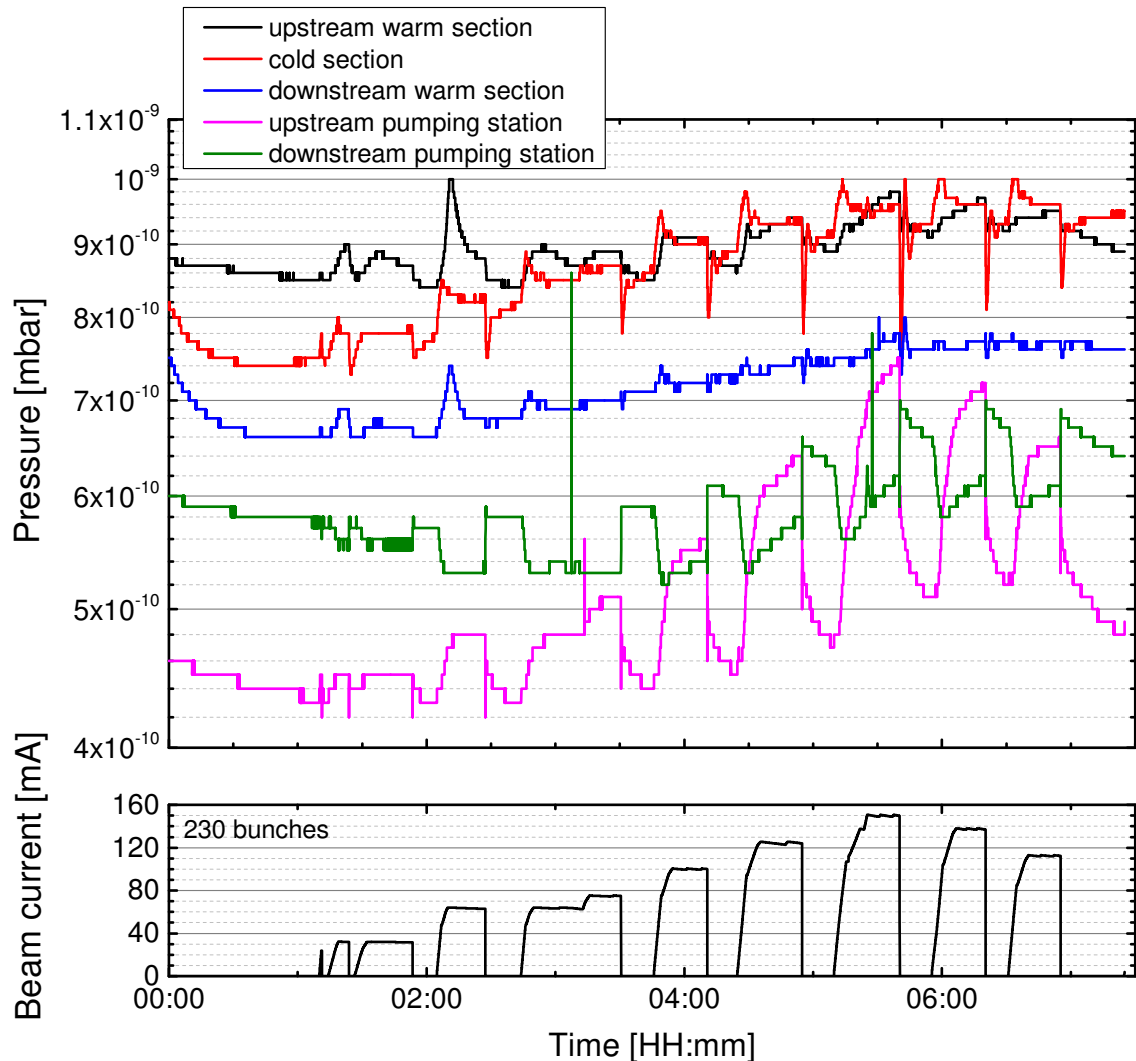


Figure 4.12: Pressure over time in the 5 sections in and around COLDDIAG during several beam current steps with 230 consecutive bunches and the temperature of the cold liner at 20 K.

Pressure and bunch length

For the measurement with a fixed filling pattern (250 mA, 900 bunches) and different bunch lengths the total pressure at each point of the beam heat load measurement is shown in Figure 4.13 as a function of bunch length. In the cold section and the two warm section of COLDDIAG no significant pressure change can be observed, while in the upstream and downstream pumping station a small pressure increase of 1×10^{-9} mbar to 2×10^{-9} mbar is visible for small bunch lengths. A possible explanation is that the bunch spectrum for small bunch lengths below 14 ps hits a resonance in the pumping stations, leading to outgassing due to the temperature increase.

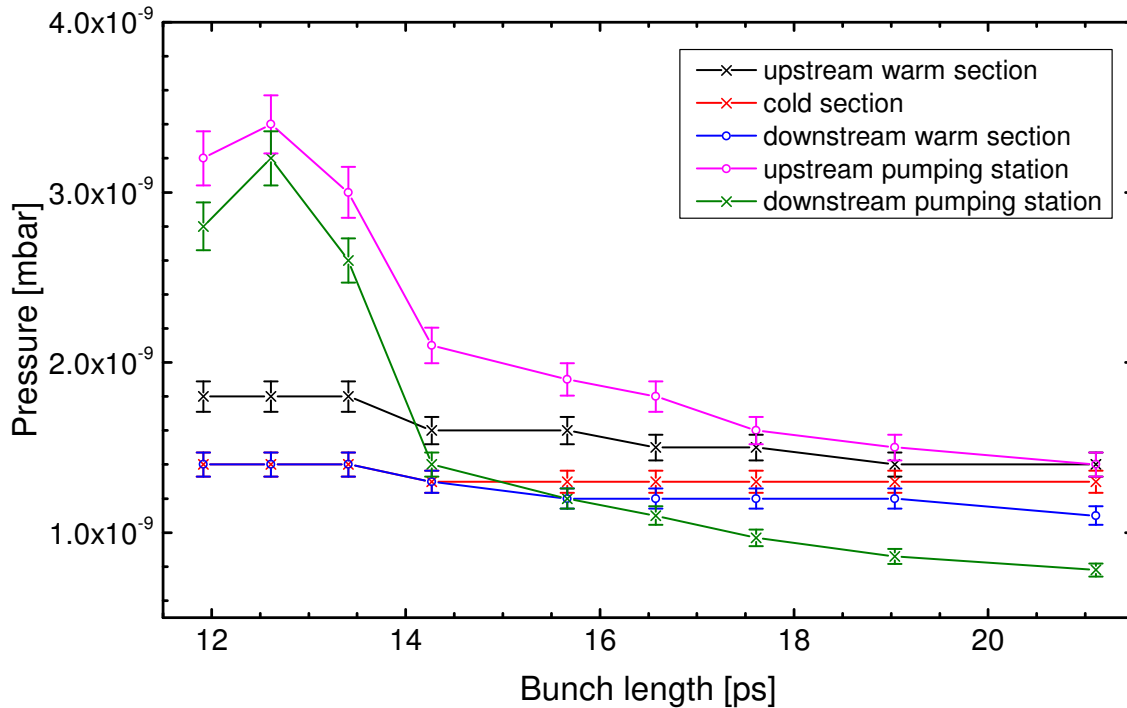


Figure 4.13: Pressure as a function of bunch length in the three sections of COLDDIAG and in the upstream in downstream pumping station. The reproducibility of the pressure reading is 5% [42].

Pressure and liner temperature

The total pressure during the beam heat load measurement at an increased liner temperature between 22.5 K and 32.5 K is shown in Figure 4.14. There is no visible pressure change in any section of COLDDIAG. Small pressure variations of 1×10^{-10} mbar are also present in the warm sections and pumping stations, where the temperature was not changed, and can therefore be neglected.

4.2.2 Gas composition

In order to get a detailed look at the gas composition the partial pressure up to an atomic mass of 100 u has been measured with the RGA in each diagnostic port. With this measurement it is not possible to see fast dynamics as happening during injection or at a beam dump, because the duration of one sweep to scan the atomic masses is over two minutes long. But for equilibrium situations, where also the rest of the measurements are taken, it is possible to get the gas content and with that the partial pressure of specific masses over time.

Figure 4.15 shows for each of the three sections in COLDDIAG the typical mass spectrum

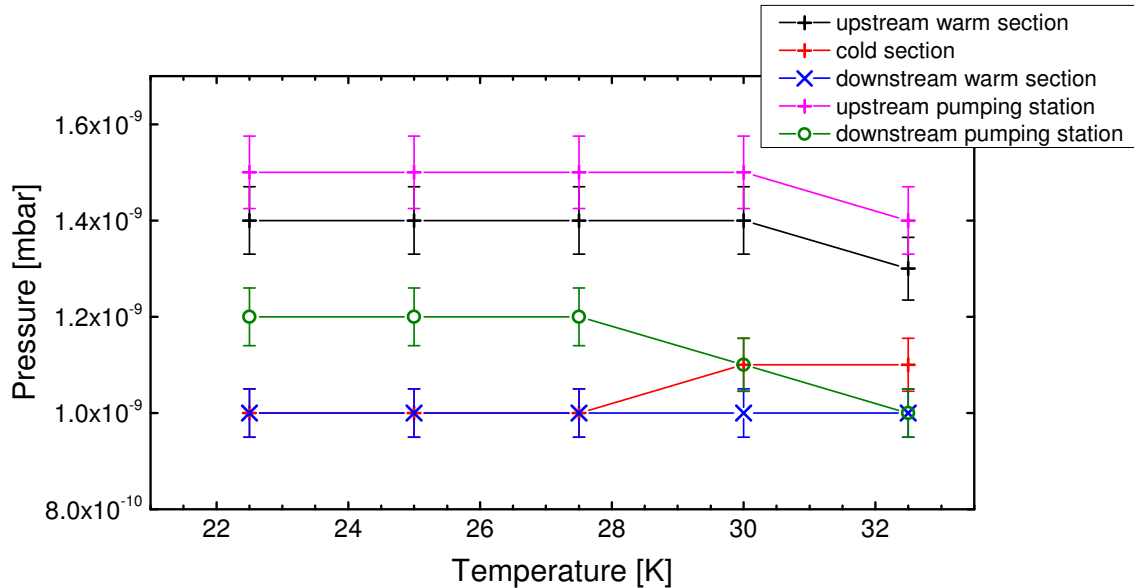
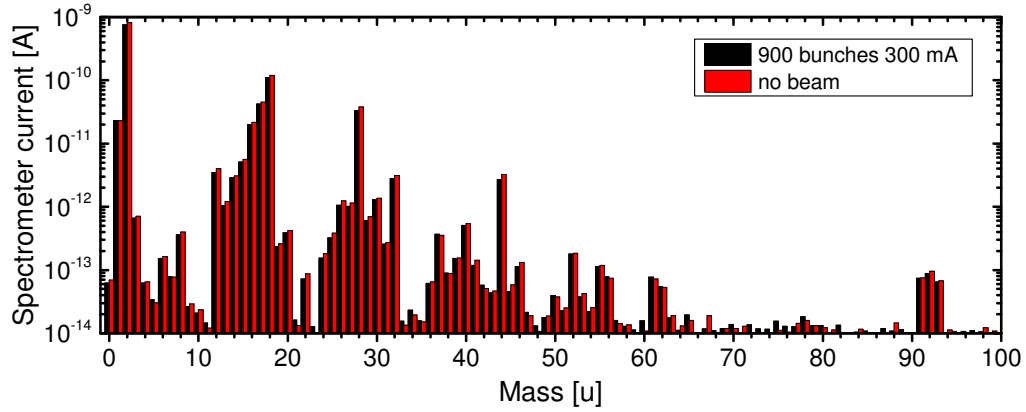


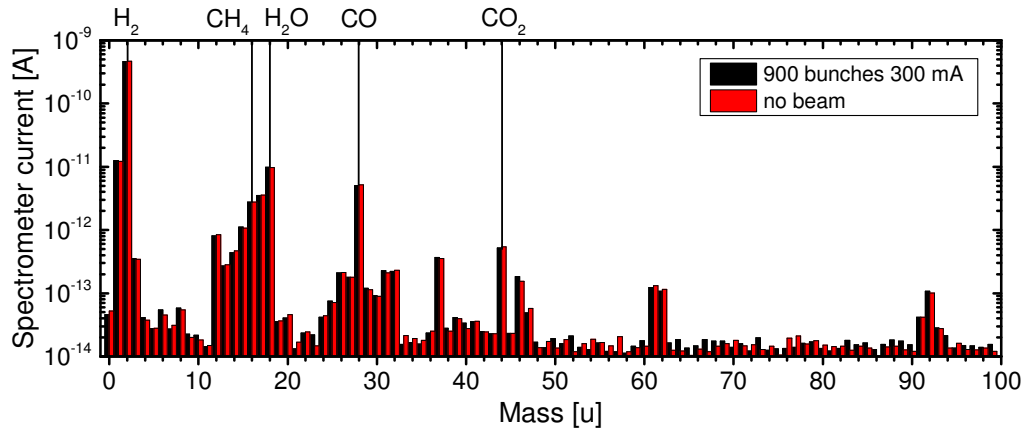
Figure 4.14: Pressure as a function of temperature during the measurement with different liner temperatures. The reproducibility of the pressure reading is 5% [42]. Filling pattern: 300 mA, 900 bunches.

of the residual gas. The spectra were taken with beam (300 mA, 900 bunches), after the pressures and the temperatures have settled from injection, and without beam after the beam dump. The main contributions from hydrogen, water, carbon monoxide/dioxide and methane are indicated. The gas composition looks similar in all three sections and is typical for an unbaked system, dominated by outgassing of the surfaces [44]. In the downstream warm section the background pressure is slightly higher and in the cold section the contribution from hydrogen relative to water is higher because of the cold surface. In all three sections the presence of the beam has no significant impact on the gas composition.

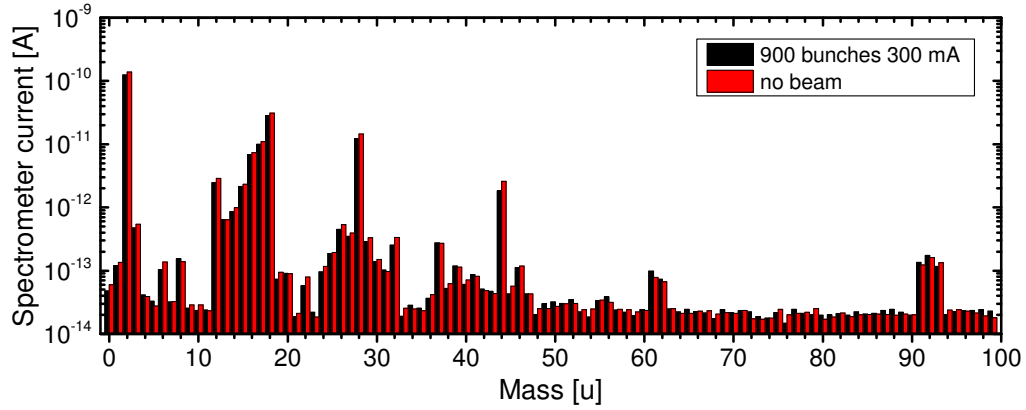
The highest contribution to the total pressure is coming from hydrogen. Figure 4.16 shows the partial pressure of hydrogen over time during a measurement of different filling patterns with beam dumps in between. At the beginning the pressure is coming down from a peak after heating up the liner to 20 K before the start of the measurement. After this initial peak the pressure settles to a base value. In the cold section the partial pressure shows a dip subsequent to each beam dump, because the liner temperature drops before the temperature control can react and adjust the heating power. When the liner temperature is back to 20 K the partial pressure is back at its base value as well. Accordingly, during injection the liner temperature shortly rises and causes the partial pressure to show a small peak. Besides these dynamic changes the partial pressure of hydrogen is independent of the filling pattern in the cold section. In the two warm sections the overall trend of the partial pressure of hydrogen is running through some variations. This can be attributed to changes in the liner temperature, since the two warm sections are not temperature controlled.



(a) Upstream warm section.



(b) Cold section.



(c) Downstream warm section.

Figure 4.15: Mass spectra of the residual gas in the three sections of COLDDIAG measured with the RGA in each diagnostic port. The measurements with and without beam are 40 minutes apart. Reproducibility of the peak ratio: 0.5%, detection limit: 1×10^{-14} mbar [43].

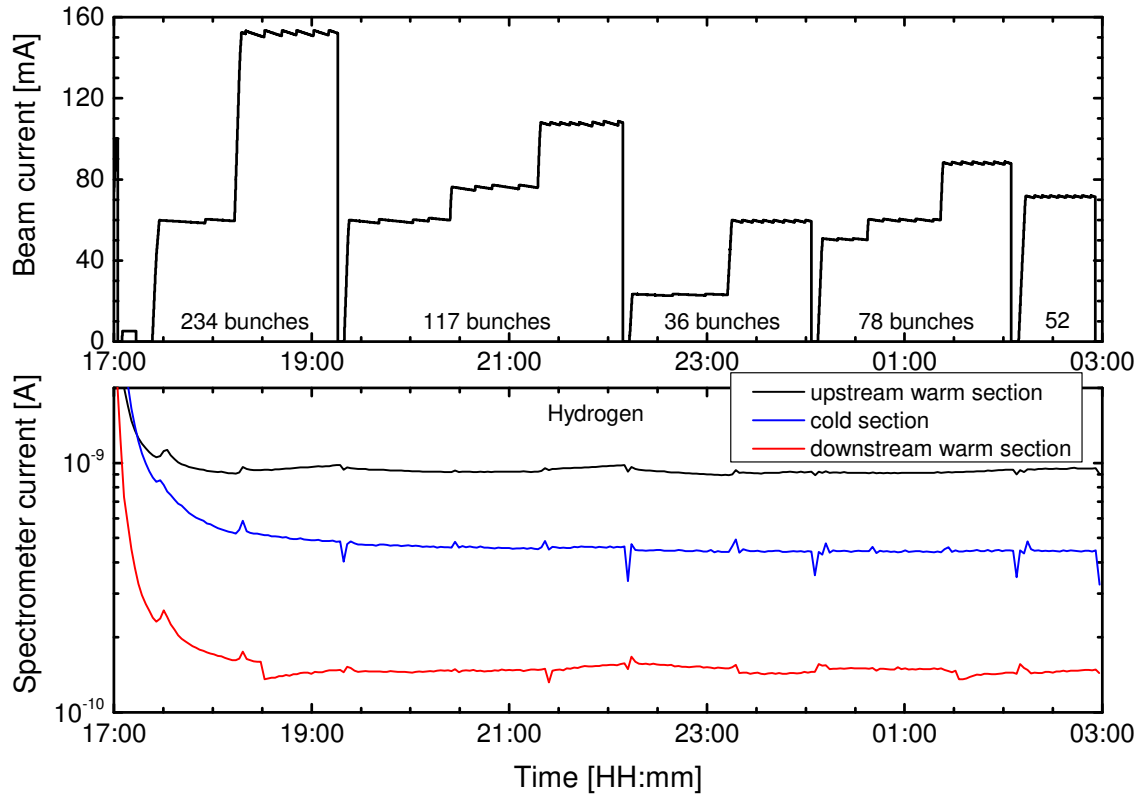


Figure 4.16: Top: beam current over time. Bottom: spectrometer current, which is proportional to the partial pressure of hydrogen in the three sections of COLDDIAG over time for several filling patterns with varying beam heat load.

For the beam heat load measurements at different liner temperatures it is interesting to look at how the partial pressures behave. In Figure 4.17 the eight largest contributions are shown as a function of time. The temperature at the cooling connection, which is just slightly lower than the liner temperature, is indicated at the top of the plot, with the oscillations in partial pressure being the transition between those temperatures. The partial pressure of hydrogen, giving the largest contribution to the total pressure, does not change significantly. The only change in partial pressure occurs at the transition between 32.5 K and 30 K, where mainly particles with mass 28 and 16 condensate. This is in agreement with the fact that in this temperature range the saturated vapour pressure of nitrogen, carbon monoxide and methane is in the UHV region [45]. The measured beam heat load shows a local minimum at that temperature (see Figure 4.8), during an otherwise rising trend. This can indicate that the absence of particles with mass 28 on the surface lowers the beam heat load.

As it is the case for the measurement of the total pressure, the high background pressure dominated by outgassing in the diagnostic ports limits the sensitivity of the partial pressure measurement.

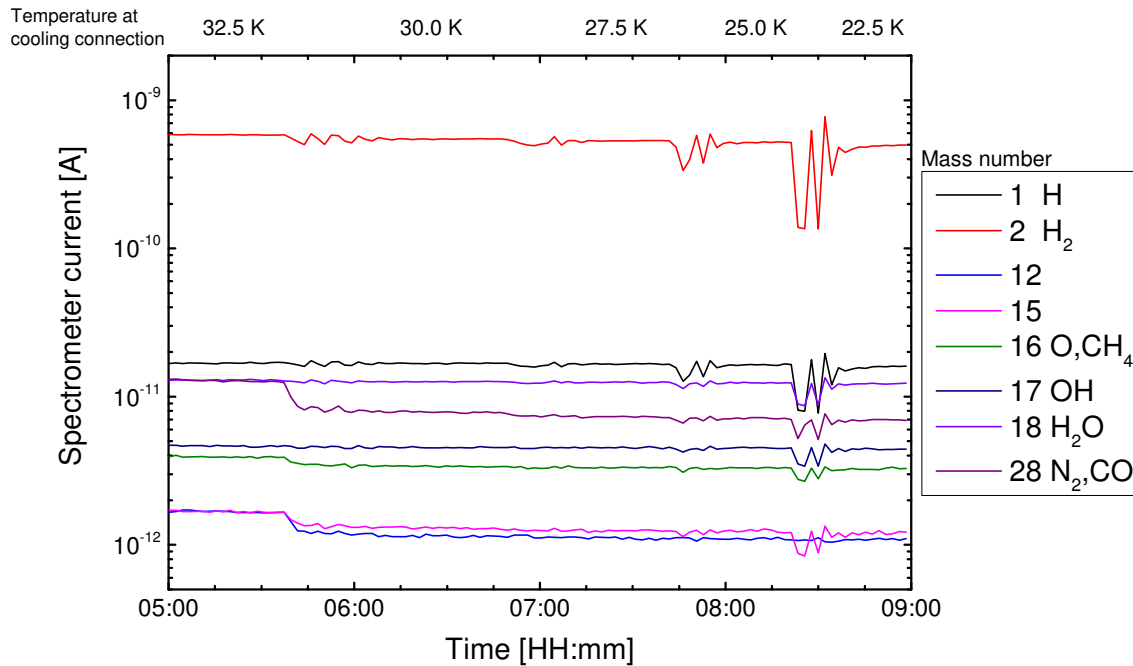


Figure 4.17: Spectrometer current of the masses with the highest contribution (proportional to partial pressure) in the cold section during the measurement with different liner temperatures (300 mA, 900 bunches).

4.2.3 Effect on heat load

To answer the question if the pressure has an influence on the beam heat load a test was done, where with beam in the machine and the liner temperature at 20 K the ion pumps were turned off to generate a pressure increase. The procedure can be followed in Figure 4.18 and Figure 4.19. The filling pattern is 250 mA in 900 bunches in top-up mode, resulting in a constant beam heat load when nothing else is changed. The heaters on the liner are set to a power that results in a liner temperature of 20 K. After the pressure has settled from activating the temperature control of the liner, the ion pumps are switched off gradually; first in the cold section, then in the two warm sections and finally in the upstream and downstream pumping station. This results in a pressure increase of roughly one order of magnitude. Even with ten times more residual particles in the beam chamber no change in beam heat load can be observed, since the liner temperature as well as the heating power at the liner heaters does not change. This excludes any heating mechanism that depends on the number of residual gas particles in the beam vacuum, like scattering of bending magnet radiation on the gas particles. It does however not exclude heating originated from the cryosorbed gas layer, because in this case the pressure rise is only a consequence and not the source of the heating.

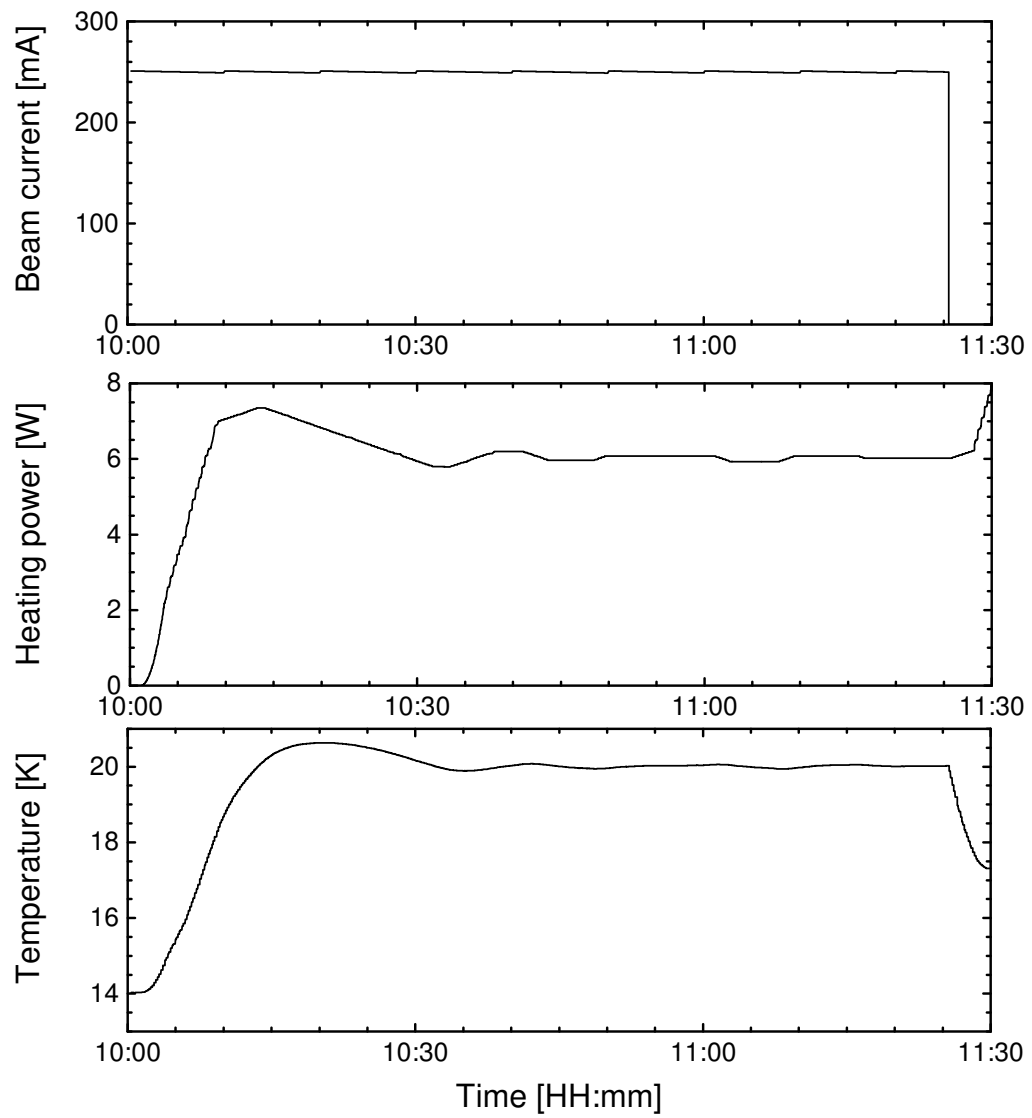


Figure 4.18: Beam current, heating power at the liner heaters and temperature at the liner during a measurement, where the effect of pressure on beam heat load was tested.

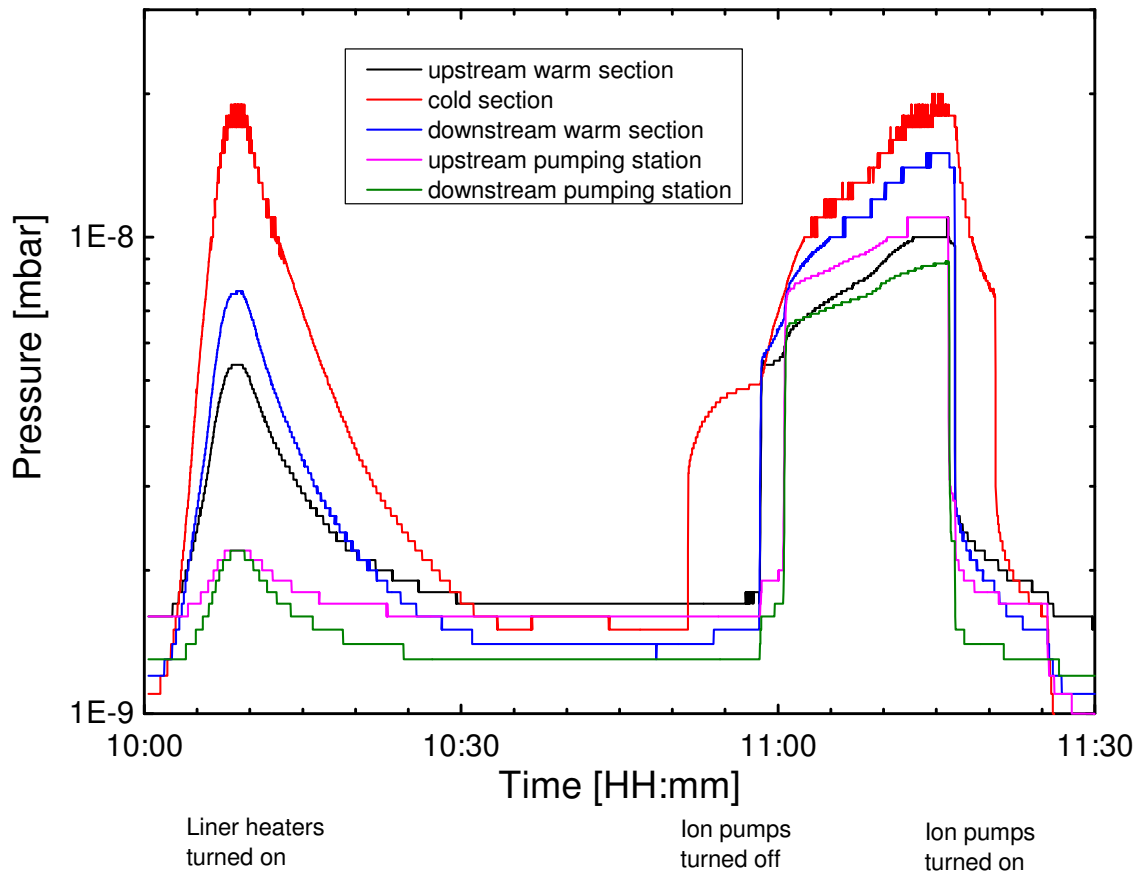


Figure 4.19: Total pressure in the different sections of COLDDIAG during a measurement, where the effect of pressure on beam heat load was tested.

4.3 Electron and ion bombardment of the chamber walls

The flux and spectrum of charged particles hitting the chamber walls was measured with retarding field analyzers installed in the cold section and the two warm sections of COLDDIAG (Section 3.2.3). The total flux is measured with the grid voltage of the RFA set to 0 V and for the energy spectrum the grid voltage is changed in a range between 0 V and 250 V. There are two methods available for the readout, measuring the RFA current directly with an electrometer and using a lockin-amplifier. The lockin-technique naturally gives the energy spectrum and is much less affected by noise. The electrometer on the other hand measures the total impinging current in ampere ($1.6 \cdot 10^{19} e^-/s$), from which the particle flux can be calculated by normalizing to the exposed surface (see later in Section 4.3.4). However, this particle flux is a lower limit for the actual flux, because of the finite transparency of the RFA and the defined position of the ports in the liner.

4.3.1 Total flux

By changing the polarity of the grid voltage and the collector voltage it is possible to differentiate between particles with a positive and a negative charge. With the grid grounded, a negative potential at the collector allows to collect positively charged ions and a positive potential at the collector is used to collect negatively charged particles. Because it has already been shown that the flux of positive ions is an order of magnitude smaller than for electrons [33], the following will concentrate on measurements with a positive bias at the collector.

Figure 4.20 shows the measurements for the flux of electrons hitting the chamber walls for three different beam current ramps in the three sections of COLDDIAG. The electron flux is increasing linearly with beam current, but with a different slope in each section. In the upstream warm section the least amount of electrons is detected, whereas in the downstream warm section about twice as much is measured, and even more in the cold section.

The linear increase of the electrometer current with beam current can be explained with photoelectrons, which are produced by synchrotron radiation. Although an upstream absorber should screen all sections of COLDDIAG from synchrotron radiation, it is still possible for reflected synchrotron radiation to reach the liner surface. The measured electron flux is lower in the upstream warm section, because it is closer to the absorber and therefore less illuminated by the reflected synchrotron radiation. From this viewpoint the electron flux in the downstream warm section would be the highest. It can be higher in the middle cold section because the cryosorbed gas layer can act as an additional source of low energy electrons. It was not possible to verify this hypothesis by measuring at room temperature, because COLDDIAG can not be safely operated without cooling.

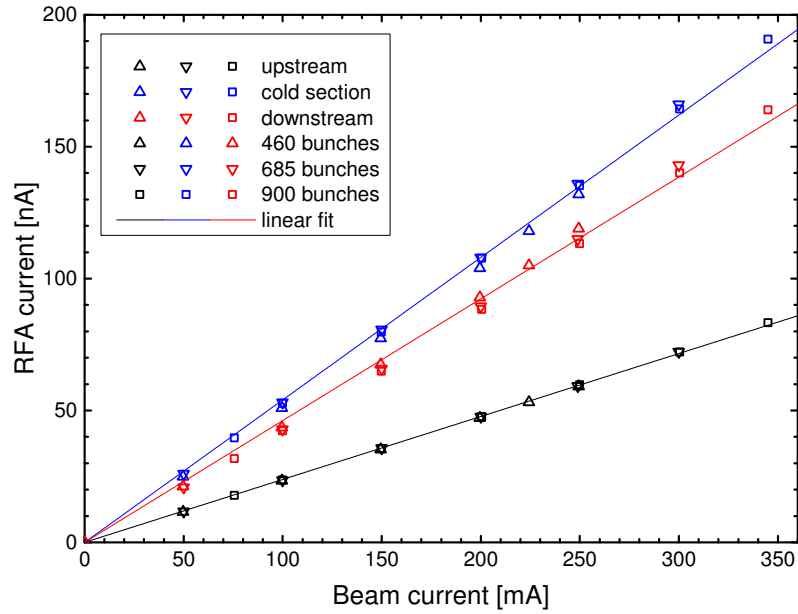


Figure 4.20: Flux of negatively charged particles (electrons) as a function of beam current for three different beam current ramps in each of the three sections of COLDDIAG, which are indicated with different colors. Accuracy of the current measurement: $\pm 0.1\% + 0.1 \text{ nA}$ [46].

4.3.2 Energy spectrum

The energy spectrum of electrons up to 250 eV is measured with the collector at 50 V, while the grid is ramped from 0 V to -250 V. For electrons the absolute value of the grid voltage in V is equivalent to the electron energy in eV. The full spectrum in Figure 4.21 shows no significant contribution above about 10 eV.

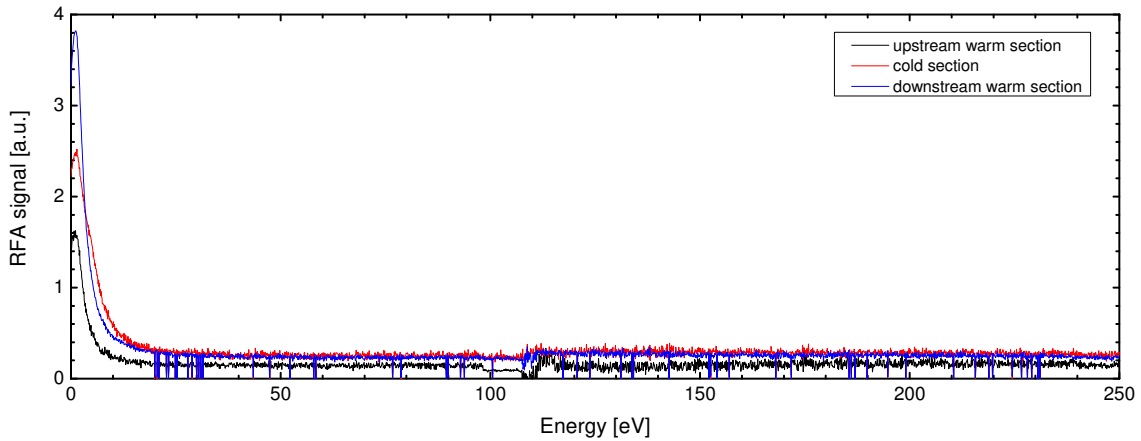


Figure 4.21: Energy spectrum of negatively charged particles (electrons) in each section of COLDDIAG for energies up to 250 eV (energy resolution: 0.1 eV). Filling pattern: 250 mA, 685 bunches, 16.0 ps bunch length.

The essential part of the spectrum up to 20 eV has been measured as a function of beam current up to 250 mA in 25 mA steps for a filling pattern with 900 consecutive bunches and the liner temperature fixed to 20 K (Figure 4.22).

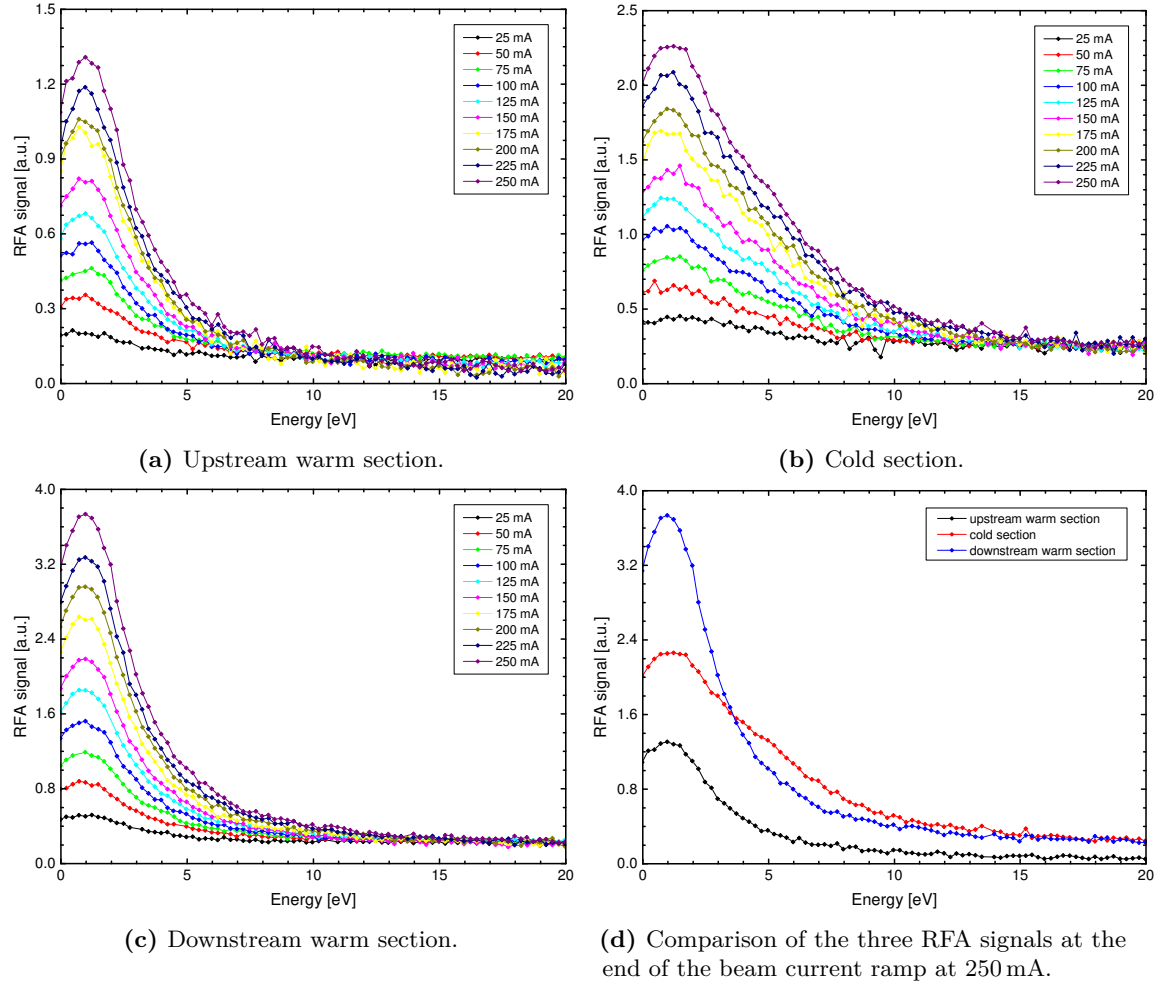
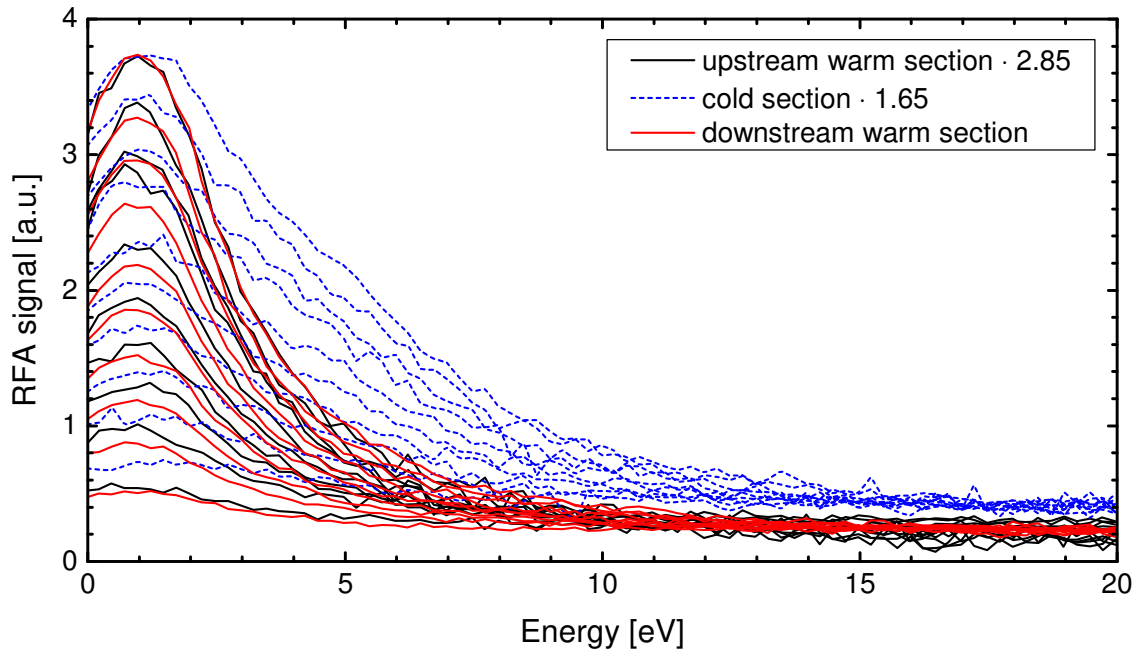
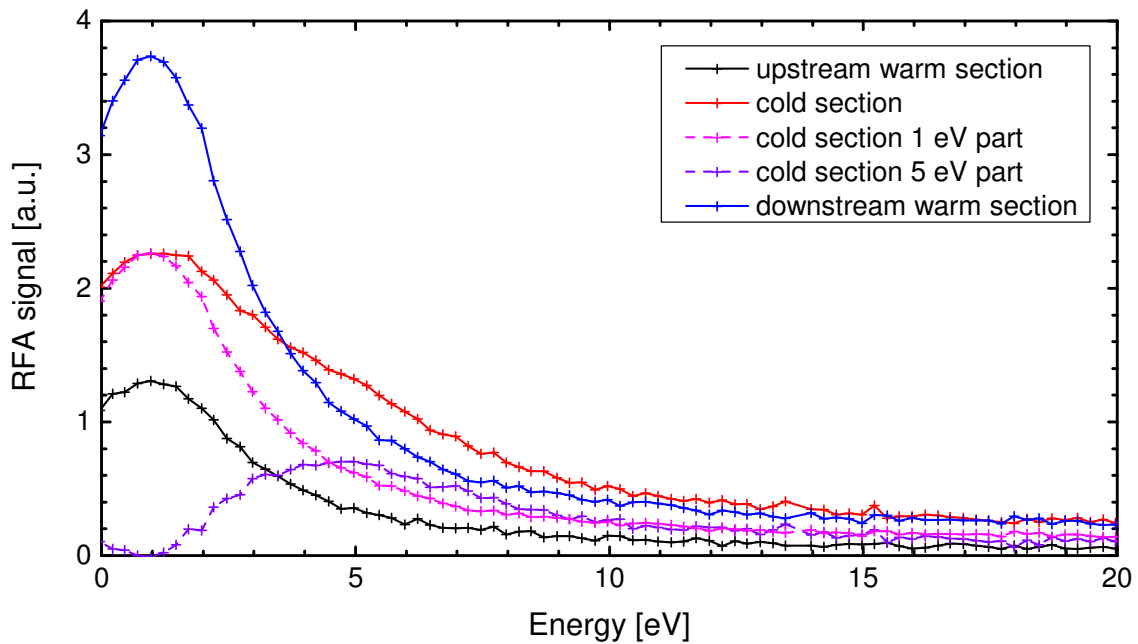


Figure 4.22: Energy spectrum of negatively charged particles (electrons) between 0 eV and 20 eV (energy resolution: 0.25 eV), hitting the chamber walls in each of the three sections of COLDDIAG for a beam current ramp with 900 bunches.

In the upstream and downstream warm section the measured total flux originates from electrons with energies below 5 eV, with the peak at 1 eV and the half maximum at 3 eV. In the cold section the peak at 1 eV is much broader and has a different shape. To investigate the shape of the peaks further in Figure 4.23(a) the energy spectrum in all three sections is scaled linearly to the same peak height at 1 eV. The shape of the spectrum is very similar in the two warm sections. Assuming that the same contribution at 1 eV is present in all three sections, the spectrum in the cold section is split in two parts in Figure 4.23(b). One part is a peak at 1 eV with the same shape as in the warm sections. The remaining part is a smaller peak at around 5 eV with a FWHM of about 6 eV.



(a) Energy spectra from Figure 4.22 scaled to the same peak height at 1 eV.



(b) Energy spectra for 250 mA and 900 bunches. The energy spectrum in the cold section is split into a peak at 1 eV, proportional to the peaks in the warm sections, and the remaining part.

Figure 4.23: Energy spectrum of negatively charged particles (electrons) between 0 eV and 20 eV (energy resolution: 0.25 eV), hitting the chamber walls in each of the three sections of COLDDIAG.

Because of this additional contribution the measured electron flux in the cold section is higher than in both warm sections. This leads to the conclusion that the cryosorbed gas layer in the cold section produces electrons with an energy of about 5 eV.

4.3.3 Beam parameters

If the low energy electrons originate from synchrotron radiation rather than the electron beam itself, one would expect to see no influence of beam parameters such as bunch length and bunch spacing on the measured electron flux. The bunch length dependence was investigated in a measurement where the accelerating voltages in the cavities of the storage ring were changed with a fixed filling pattern (250 mA, 900 bunches), thus only changing the bunch length (left plot in Figure 4.24). The dependence on the bunch spacing was measured with filling patterns that have the same beam current, but a different number of bunches. The bunches are equally distributed along the storage ring, effectively increasing the bunch spacing with a decreasing number of bunches (right plot in Figure 4.24). For both cases the total electron flux was measured with the collector voltage at 50 V and the grid grounded.

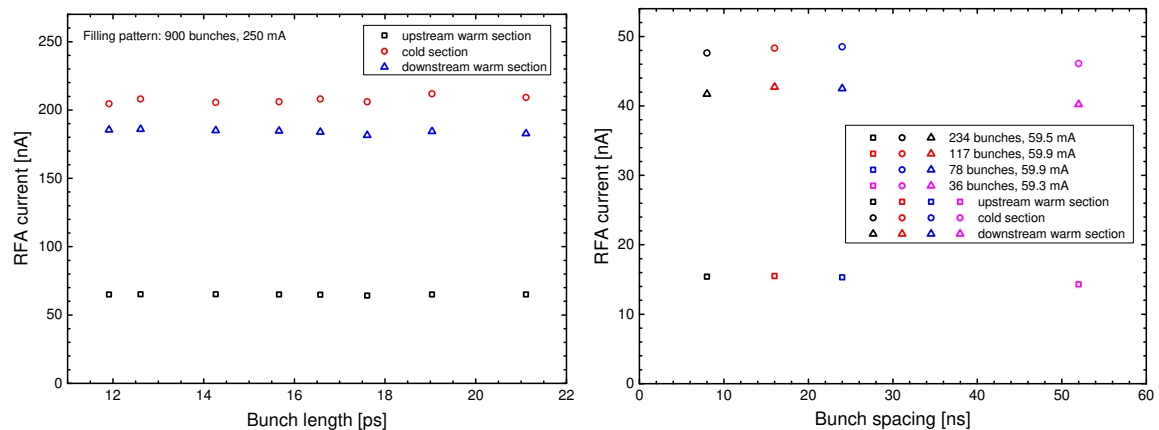


Figure 4.24: Flux of negatively charged particles (electrons) as a function of bunch length and bunch spacing in each of the three sections of COLDDIAG, which are indicated with different symbols.

In all three sections of COLDDIAG no significant variation of the electron flux is observed as a function of bunch length and bunch spacing. This supports the assumption that the origin of the measured low energy electrons is not the electron beam directly, but reflected synchrotron radiation from the upstream bending magnet.

4.3.4 Heat load from low energy electrons

The heat load caused by low energy electrons hitting the chamber walls can be estimated from the measured flux and spectrum. It is assumed that their kinetic energy is fully

converted to heat and that the measured flux and spectrum is the same for the whole chamber wall.

For the cold section the surface area is:

$$A_{\text{cold}} = \text{length} \cdot \text{circumference} = 0.5 \text{ m} \cdot 0.1245 \text{ m} = 6.2 \times 10^{-2} \text{ m}^2 \quad (4.3)$$

The surface area covered by the slits leading to the RFA, which represents the active measuring area, is:

$$A_{\text{slits}} = 4.8 \times 10^{-4} \text{ m}^2 \quad (4.4)$$

By assuming a 50 % transparency of the grid, which means that every second electron entering the slits gets detected, the ratio between the measured electrons and the total number of electrons hitting the chamber wall is:

$$\frac{\text{total } e^-}{\text{measured } e^-} = 2 \cdot \frac{A_{\text{cold}}}{A_{\text{slits}}} = 258 \quad (4.5)$$

The total number of electrons can be calculated by multiplying this ratio with the measured RFA collector current of up to 200 nA:

$$\text{total } e^- = \frac{2.0 \times 10^{-7} \text{ A}}{1.6 \times 10^{-19} \text{ A s}} \cdot 258 = 3.2 \times 10^{14} \frac{\text{electrons}}{\text{s}} \quad (4.6)$$

Since in the energy spectrum of the RFA in the cold section most electrons have a smaller energy than about 5 eV, a conservative estimate for the heating power is done by assuming that all electrons have an energy of 5 eV:

$$P_{e^-} = 5 \text{ eV} \cdot 3.2 \times 10^{14} \frac{\text{electrons}}{\text{s}} = 0.26 \text{ mW} \quad (4.7)$$

This result is four orders of magnitude smaller than the measured beam heat load, although rough assumptions are made about the detection efficiency of the RFA. It indicates that low energy electrons are not responsible for the heating of the liner. However, it cannot be excluded that the low energy electrons are not distributed equally and therefore do not hit the liner where the slots to the RFAs are.

4.4 Beam displacement

To investigate the influence of the stored electron beam position on the measured beam heat load, the beam was steered in the vertical and horizontal direction by introducing orbit bumps in the straight section, where COLDDIAG was installed.

The beam displacement in the vertical plane is shown in Figure 4.25. The beam current was kept at 300 mA using the top-up mode and no heater was powered during the measurement, which means that the temperature at the cooling connection is directly related to the measured beam heat load including the heat from the thermal transitions. At the bottom of Figure 4.25 the changes in beam position are indicated. First the beam was steered up by 1 mm along the straight section. Then it was steered in the opposite direction by 2 mm. From there it was steered along a diagonal path in the vertical plane, starting at -1 mm in the upstream magnet and going to 1 mm in the downstream magnet. After a beam loss the diagonal path was mirrored, starting at 1 mm in the upstream magnet and going to -1 mm in the downstream magnet. The only change in temperature at the cooling connection that is not correlated to the thermal transition temperatures occurs when the beam is shifted down by 1 mm along the whole straight section. While the temperature at the cooling connection rises from 17.5 K to 18.3 K, the temperatures at the upstream and downstream transitions rise by 7 K and 6 K, respectively. This indicates that the heat load is not only increased in the cold section, but also in the thermal transitions. There is no measurable change in heat load when the beam is steered diagonal through COLDDIAG. The important difference to an even shift by 1 mm is that the steer by 1 mm in opposite directions in the magnets creates a beam displacement in COLDDIAG that is only about $100\ \mu\text{m}$ at the ends of the cold liner. There are at least two possible reasons why no change in beam heat load can be observed by shifting the beam up instead of down. One is that the vertical alignment of the liner with respect to the beam may not be centered, but slightly shifted up. The other reason is that, for a certain distance, the beam may couple to the slits of the diagnostic ports (this would however not explain the heat in the thermal transitions).

The beam displacement in the horizontal plane is shown in Figure 4.26. Here the beam was moved by a total distance of 1.05 mm. The changes in beam position are again indicated at the bottom of Figure 4.26. First the beam is moved to $+0.35$ mm (a positive displacement is towards the center of the storage ring) from the original orbit in the straight section of COLDDIAG. Then the displacement is stepped slowly from $+0.35$ mm to -0.6 mm. And finally the beam is returned to its original orbit. For this measurement the temperature at the cooling connection is kept at 20 K by the liner heaters, for which the heating power is shown in the middle plot of Figure 4.26. The heating power shows a negative slope throughout the whole measurement, which is related to the temperature increase in the thermal transitions.

Overall, the beam heat load is not sensitive to small variations of the beam position. Only a downward movement by 1 mm results in a slight increase of the beam heat load.

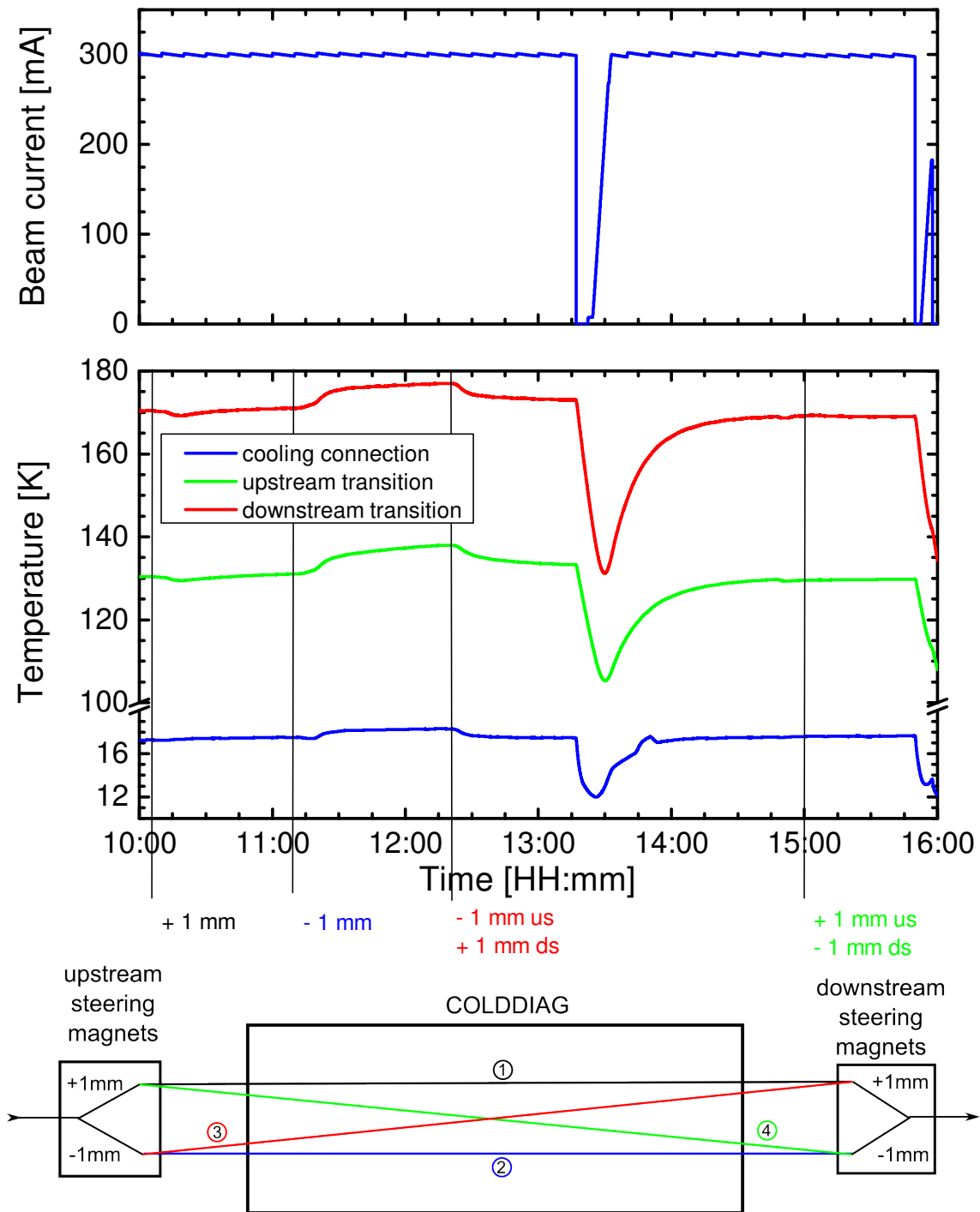


Figure 4.25: Effect of beam displacement in the vertical direction on the measured beam heat load. Top: average current of the stored electron beam, Middle: temperature at the cooling connection to the liner and at the thermal transitions, Bottom: sketch of the beam displacement in the straight section.

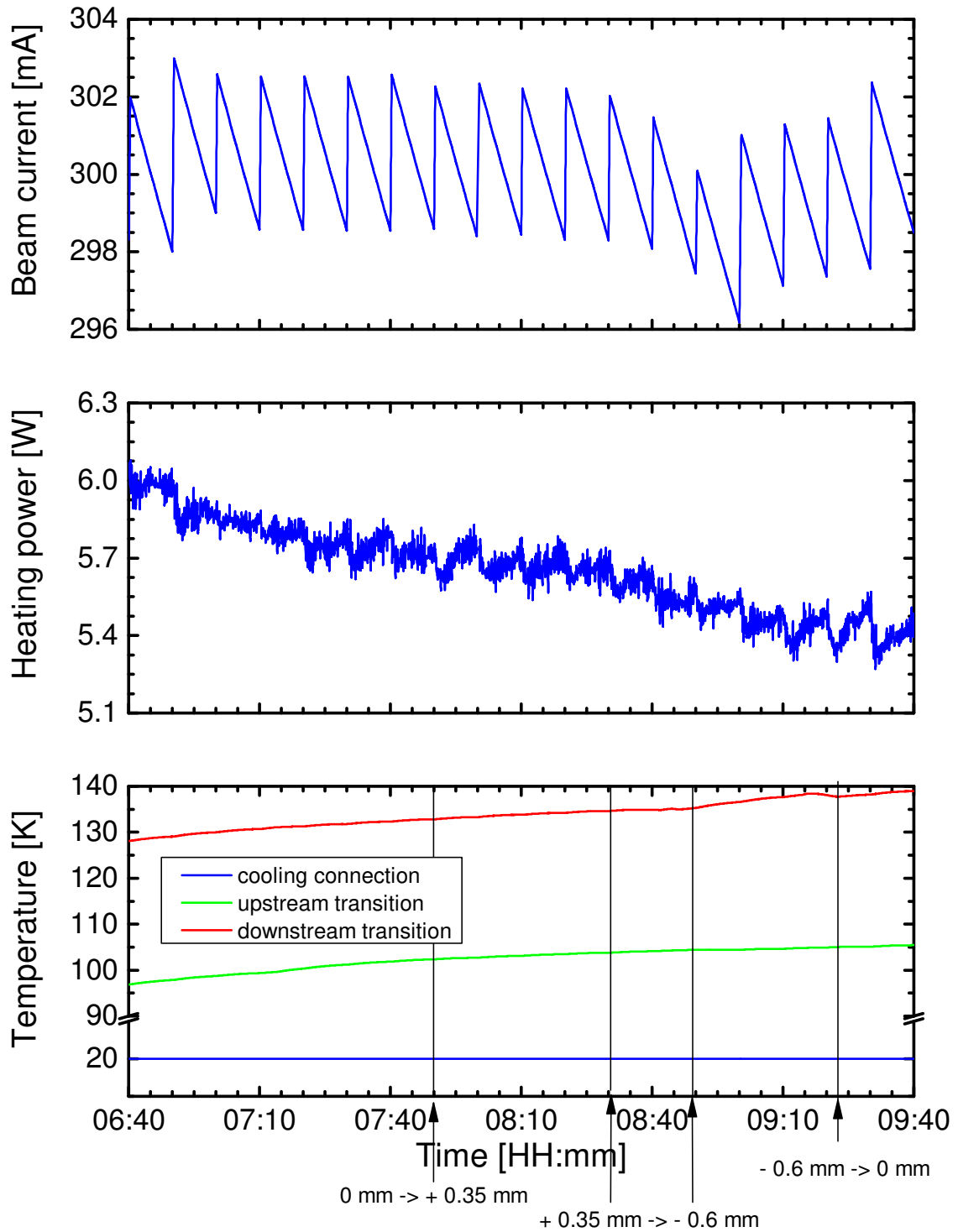


Figure 4.26: Effect of beam displacement in the horizontal direction on the measured beam heat load. Top: average current of the stored electron beam (900 bunches), Middle: heating power at the liner heaters, Bottom: temperature at the cooling connection to the liner and at the thermal transitions. A positive displacement is towards the center of the storage ring.

4.5 Temperature distribution on the liner

The temperature distribution on the cold liner can be observed with 16 temperature sensors distributed along the bottom and top of the liner. They allow to determine if the heat is deposited equally on the liner surface, or if the temperature distribution follows a specific pattern.

4.5.1 Static temperature distribution at 20 K

The instantaneous spatial temperature distribution on the liner is pictured in Figure 4.27 without a stored electron beam and in Figure 4.28 with 300 mA in 685 bunches. The pictures are taken from a readout software that was programmed in the framework of this thesis. In both cases the temperature of the cooling connection is adjusted to 20 K. Two of the temperature sensors show no meaningful value, i.e. a flat line instead of the typical temperature response, and they are marked in white. For different measurements in other temperature regions they started to show a sensible response.

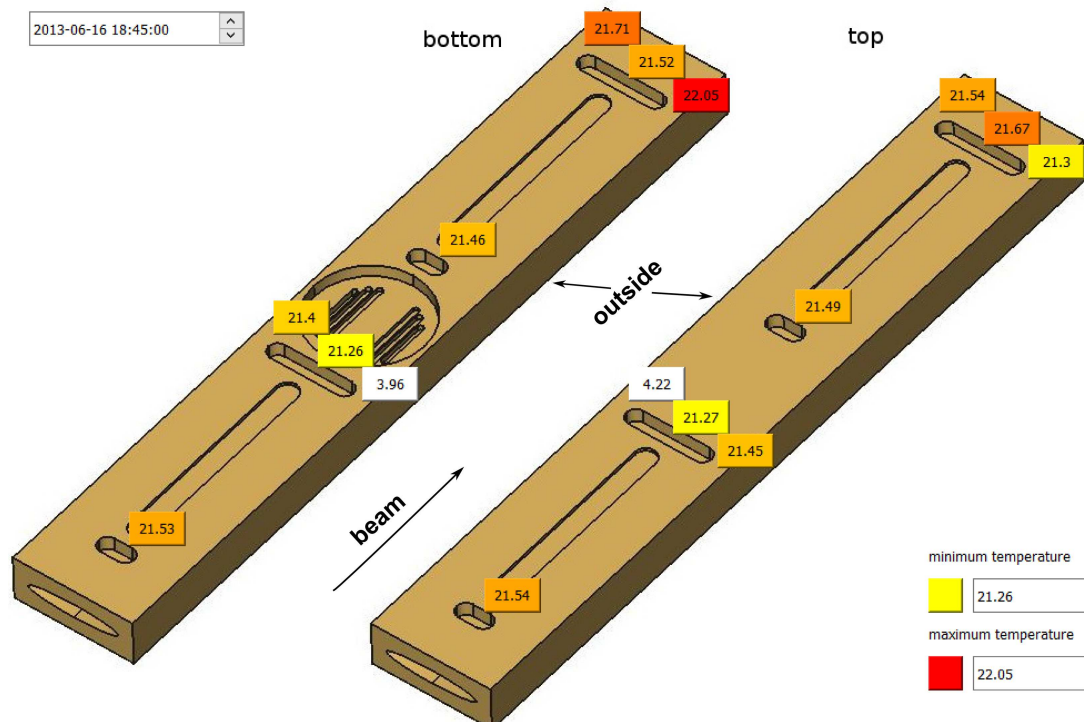


Figure 4.27: Spatial temperature distribution on the bottom and top of the liner at 20 K without beam. A color scale from yellow (low) to red (high) is applied to the temperatures. Two sensors are not working and marked in white. Calibration accuracy: ± 0.25 K. Average temperature: 21.51 K.

Without beam, the temperature sensors on the cold liner show a temperature between

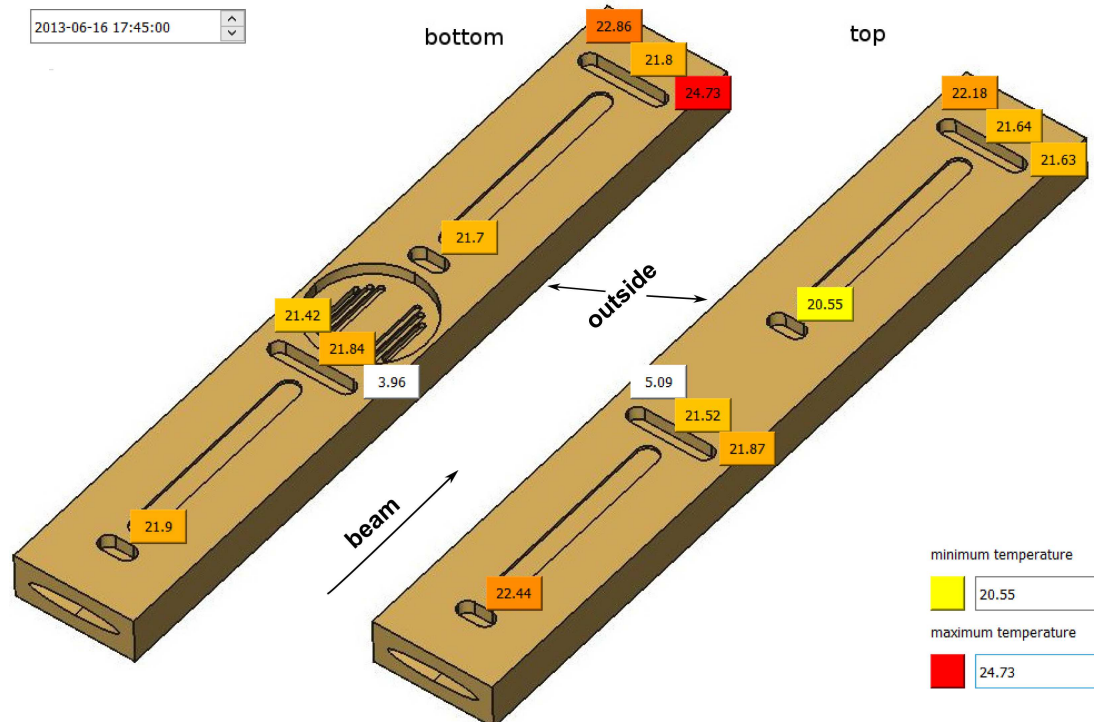


Figure 4.28: Spatial temperature distribution on the bottom and top of the liner at 20 K with beam (300 mA, 685 bunches). A color scale from yellow (low) to red (high) is applied to the temperatures. Two sensors are not working and marked in white. Calibration accuracy: ± 0.25 K. Average temperature: 22.01 K.

21.26 K and 21.71 K, within the calibration accuracy of 0.25 K. Only one sensor, which is located downstream, on the bottom of the liner and towards the outside of the storage ring, is showing a higher temperature of 22.05 K.

With beam, the average temperature slightly rises and most of the sensors show a temperature between 21.42 K and 21.90 K. The sensor showing the highest temperature without beam is measuring a considerably higher temperature with beam. Additionally two sensors downstream (one on the bottom and one on the top) and the sensor upstream on the top read a higher than average temperature. One sensor (top, middle towards downstream) is reading a 1.1 K lower than average temperature.

The measurements show that the presence of the electron beam changes the temperature distribution on the cold liner. But it is not possible to deduce a clear heating pattern that is consistent with the cooling path, especially when considering the sensor showing a lower temperature than without beam. This will be examined further in Section 4.5.5 using heat transfer simulations.

4.5.2 Static temperature distribution without heaters

While for the determination of the beam heat load it is beneficial to use the heaters on the liner in order to measure at a defined temperature, they are not needed for the measurement of the temperature distribution. In Figure 4.29 and 4.30 the temperature distribution is shown for the same beam conditions as in the previous section, but without using the heaters on the liner. This allows to examine if the heaters have an influence on the temperature distribution.

Without beam and at the base temperature all sensors show a value within $5.7\text{ K} \pm 0.2\text{ K}$, which is within the calibration accuracy.

With beam the key aspects of the temperature distribution are similar to the measurement with heaters, but small differences exist. The highest and the lowest temperature is measured at the same location as shown in Figure 4.28, but their distance to the average temperature is about 1 K larger. Overall, the spread of the measured temperatures with beam is considerably larger without using the heaters on the liner. The spread increases from 4.18 K to 6.42 K considering all temperature sensors on the liner, and from 1.44 K to 1.90 K neglecting the sensor with the highest and with the lowest temperature.

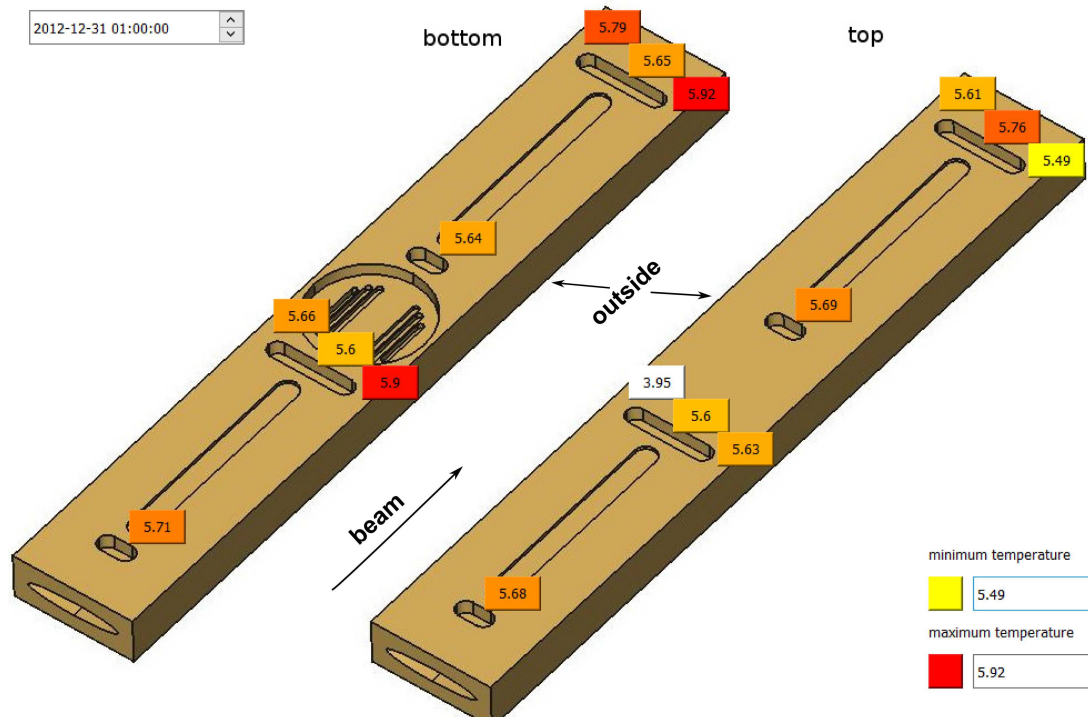


Figure 4.29: Spatial temperature distribution on the bottom and top of the liner without beam and heaters. A color scale from yellow (low) to red (high) is applied to the temperatures. One sensor is not working and marked in white. Calibration accuracy: $\pm 0.25\text{ K}$. Average temperature: 5.69 K .

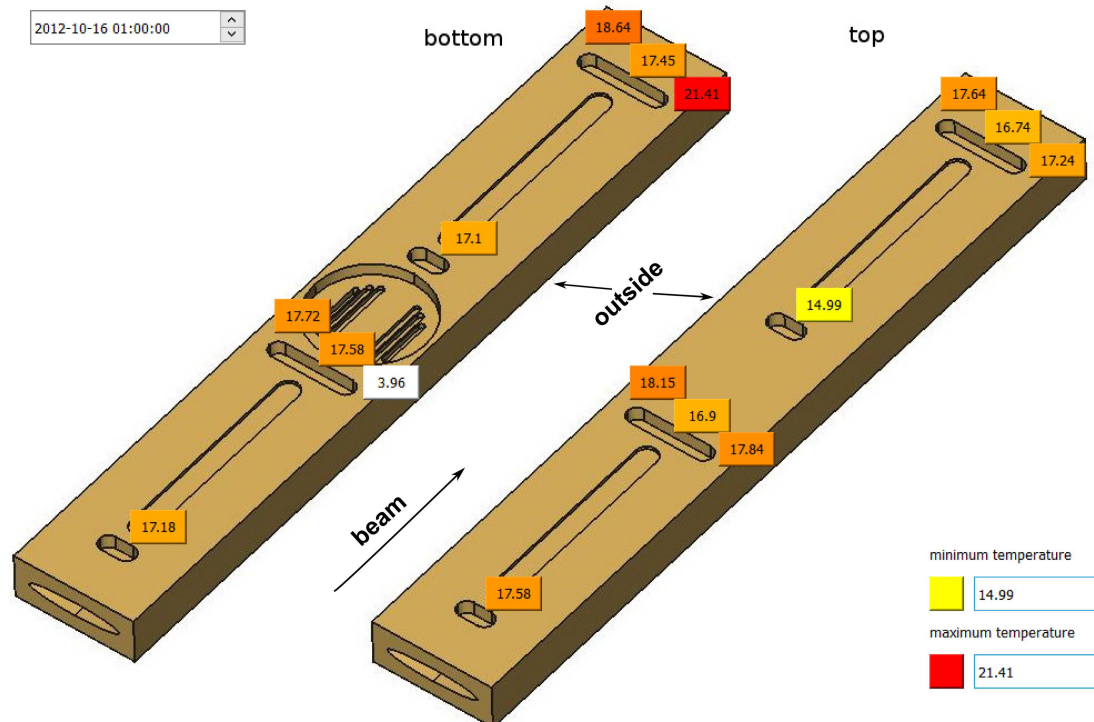


Figure 4.30: Spatial temperature distribution on the bottom and top of the liner without heaters and with beam (300 mA, 685 bunches). A color scale from yellow (low) to red (high) is applied to the temperatures. One sensors is not working and marked in white. Calibration accuracy: ± 0.25 K. Average temperature: 17.61 K.

4.5.3 Dynamic temperature distribution at 20 K

To visualize how the temperature distribution develops with increasing beam heat load one can look at the temperatures during a beam current ramp. In Figure 4.31 this is shown for a beam current ramp with 685 consecutive bunches up to 300 mA in 50 mA steps. In the upper plot the sensors on top of the liner and on the bottom are color-coded in red and blue, and in the lower plot the sensors located to the outside of the storage ring, in the center and to the inside of the storage ring are color-coded in green, red and blue. The temperature of the cooling connection, which is adjusted by a PID control loop, illustrates the temperature gradient to the liner.

The temperatures on the liner start with a spread of 0.8 K at the start of the beam current ramp, which increases to 4.4 K at the highest beam current. The temperature sensor showing the highest temperature also undergoes the largest temperature change during the beam current ramp. The initial temperature spread can be explained by a varying thermal coupling between the sensors and the liner, because if a sensor has less contact to the cooling connection it measures a higher temperature.

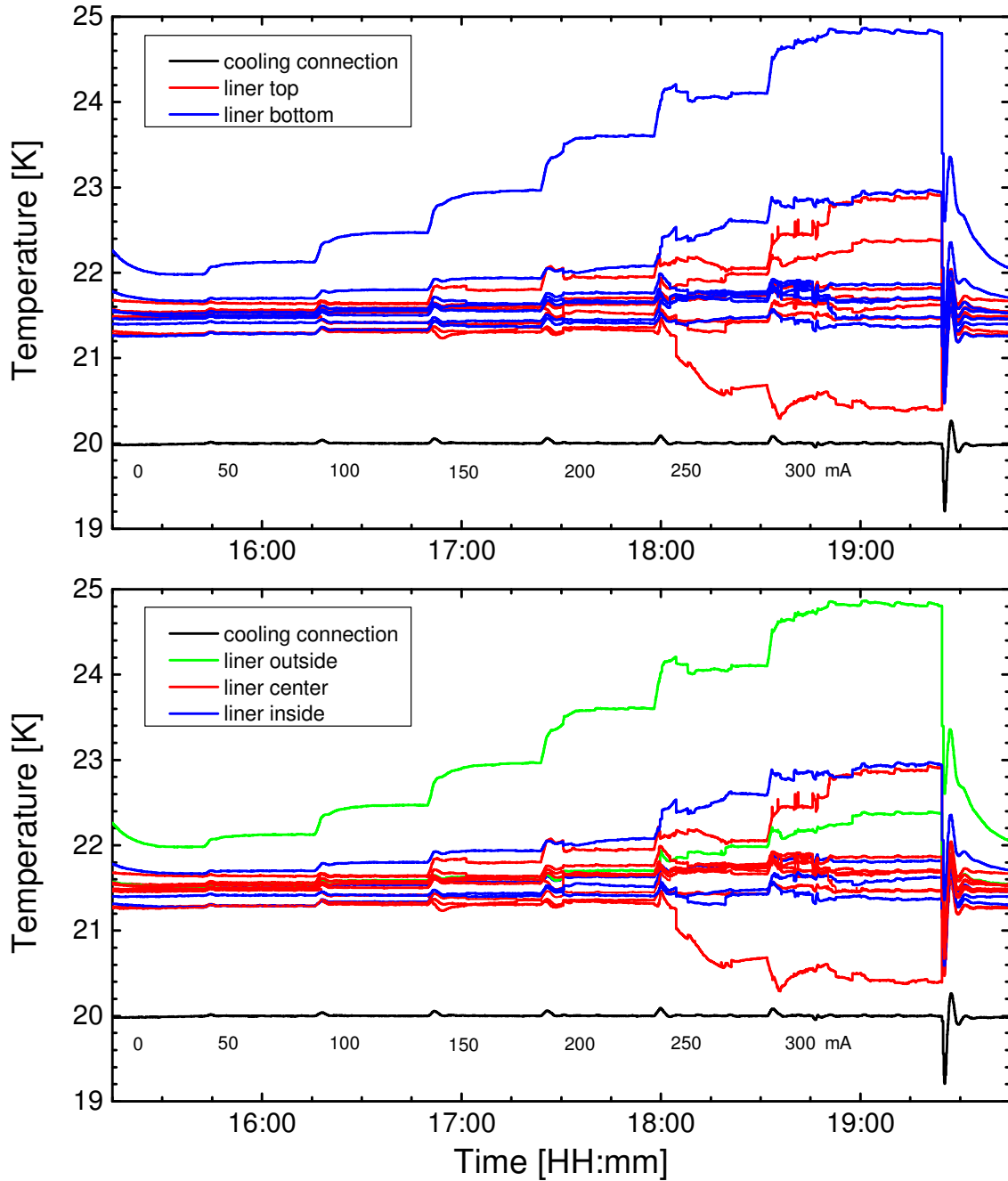


Figure 4.31: Temperature distribution on the liner during a beam current ramp with 685 bunches to 300 mA in 50 mA steps.

For high electron beam currents all the sensors are affected by sudden, noise-like variations. One of the sensors shows a significantly lower temperature at the end of the ramp than with no beam. This is not intuitive, because a lower temperature would indicate a local cooling source at the sensor. Since CernoxTM sensors are resistant to radiation and magnetic fields, an explanation for this occurrence could be that electric fields created by the electron beam get picked up by the temperature sensors and disturb the measurement. Another possible explanation is that the thermal/mechanical contact becomes unstable, when the liner is warmed up by the beam and expands.

For comparison, Figure 4.32 shows the readings of the same temperature sensors during the offline calibration of a beam current ramp. Here the temperature changes are solely coming from a varying heat intake from the thermal transitions connecting to the 50 K shield, since the heating from the beam is missing. Therefore the heat load and the temperature spread is smaller than in the measurement with beam. The noise-like variations are missing completely, confirming that they are caused by the beam.

4.5.4 Dynamic temperature distribution without heaters

In Figure 4.33 the temperature distribution without heaters is shown for a beam current ramp with the same filling pattern as before. Because of the missing heaters the average temperature depends on the beam heat load. But the features of the relative temperature distribution is similar to the measurement at a fixed liner temperature, i.e. wider temperature spread with increasing heat load and noise at higher beam currents. One major difference is that above 200 mA one sensor on the liner is measuring a temperature that is lower than the temperature at the cooling connection. This behaviour is non-physical, because with no other cooling sources the lowest temperature has to be at the cooling connection.

Figure 4.34 shows the temperature distribution on the liner during the calibration of the cooling connection temperature to the heat load from the heaters on the liner. For the whole temperature range the temperature spread is considerably smaller than with beam and no noise is observed for high heat loads.

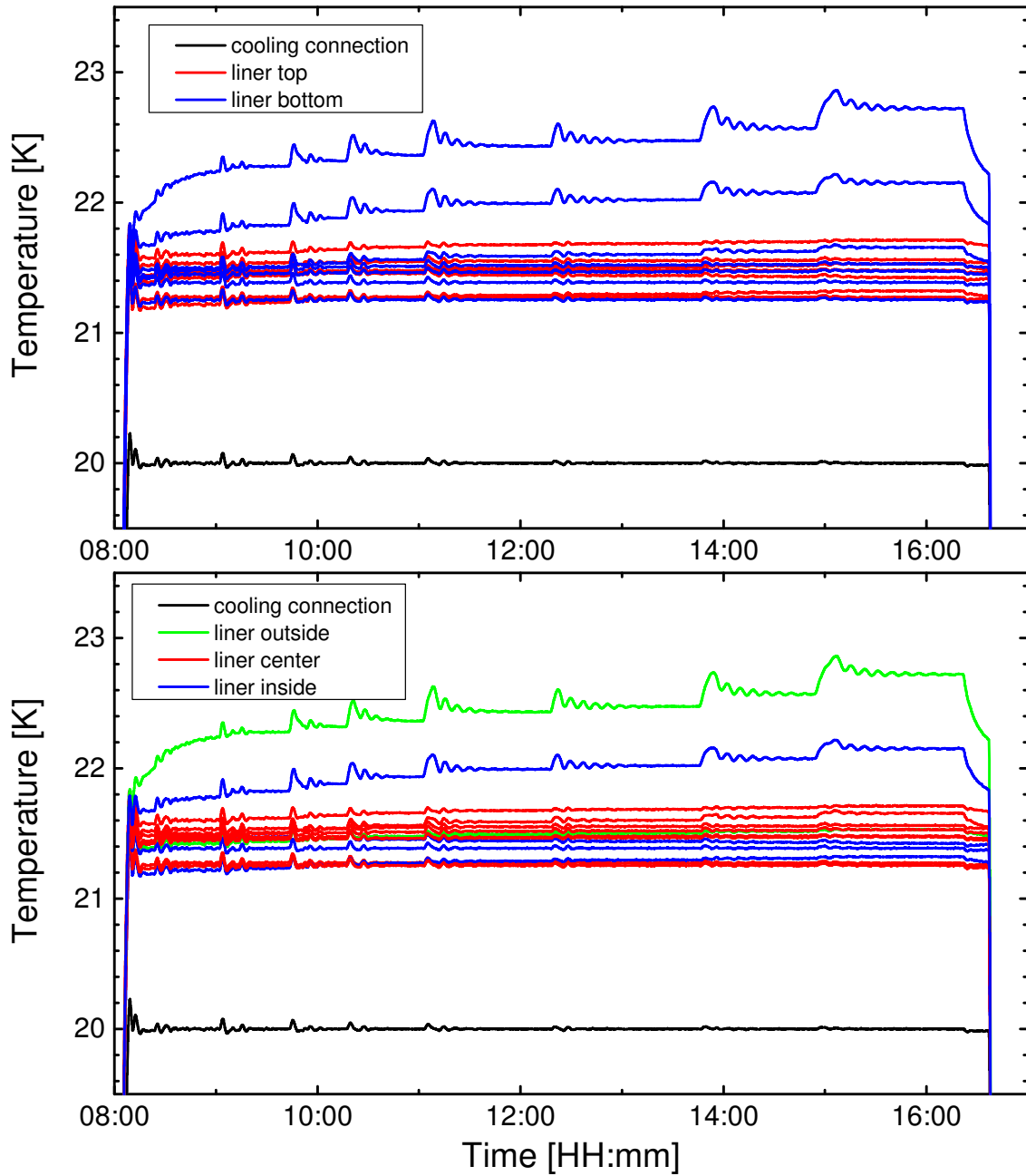


Figure 4.32: Temperature distribution on the liner during the calibration of the 685 bunches beam current ramp. The steps correspond to different thermal transition temperatures.

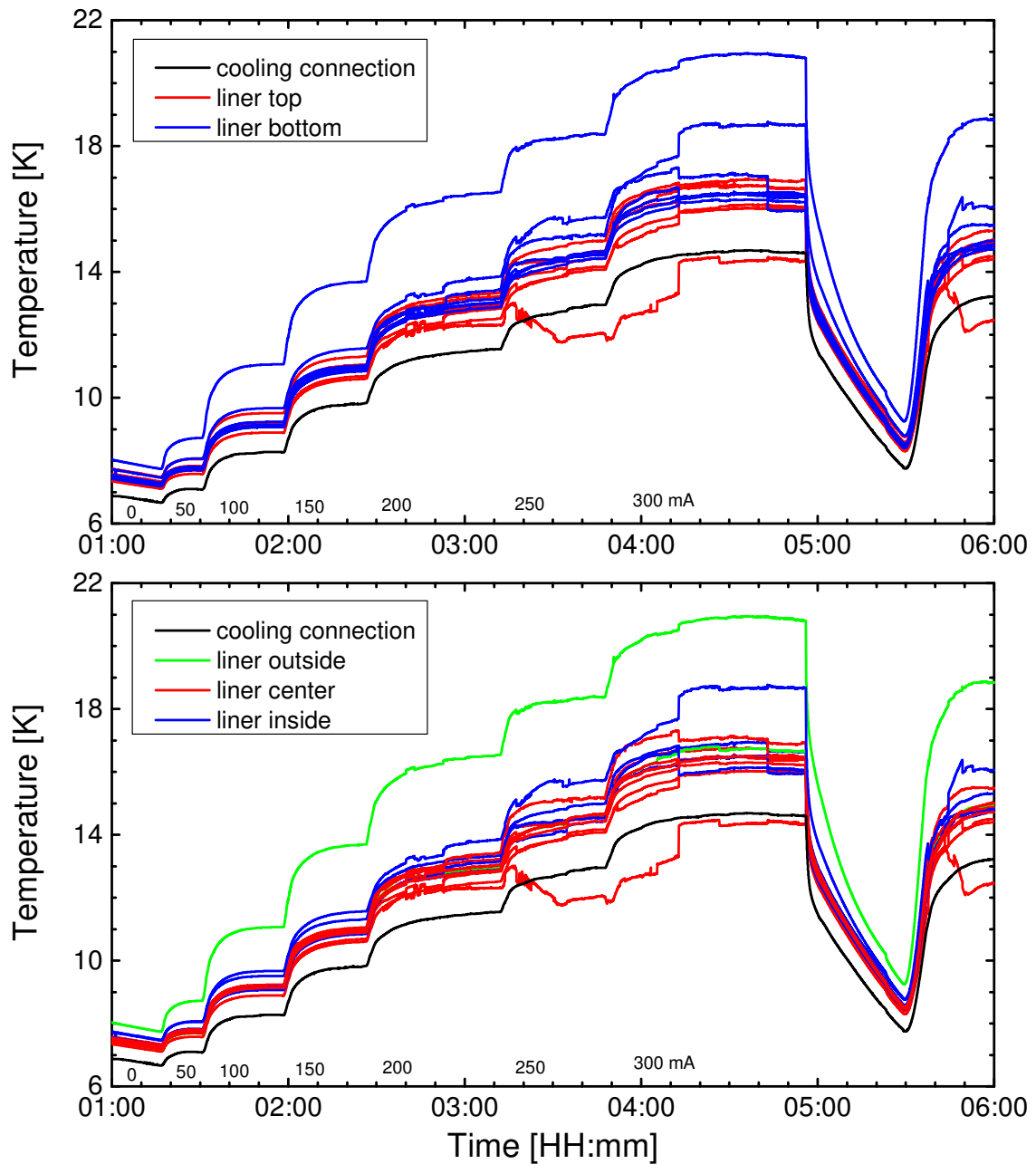


Figure 4.33: Temperature distribution on the liner during a beam current ramp with 685 bunches to 300 mA in 50 mA steps.

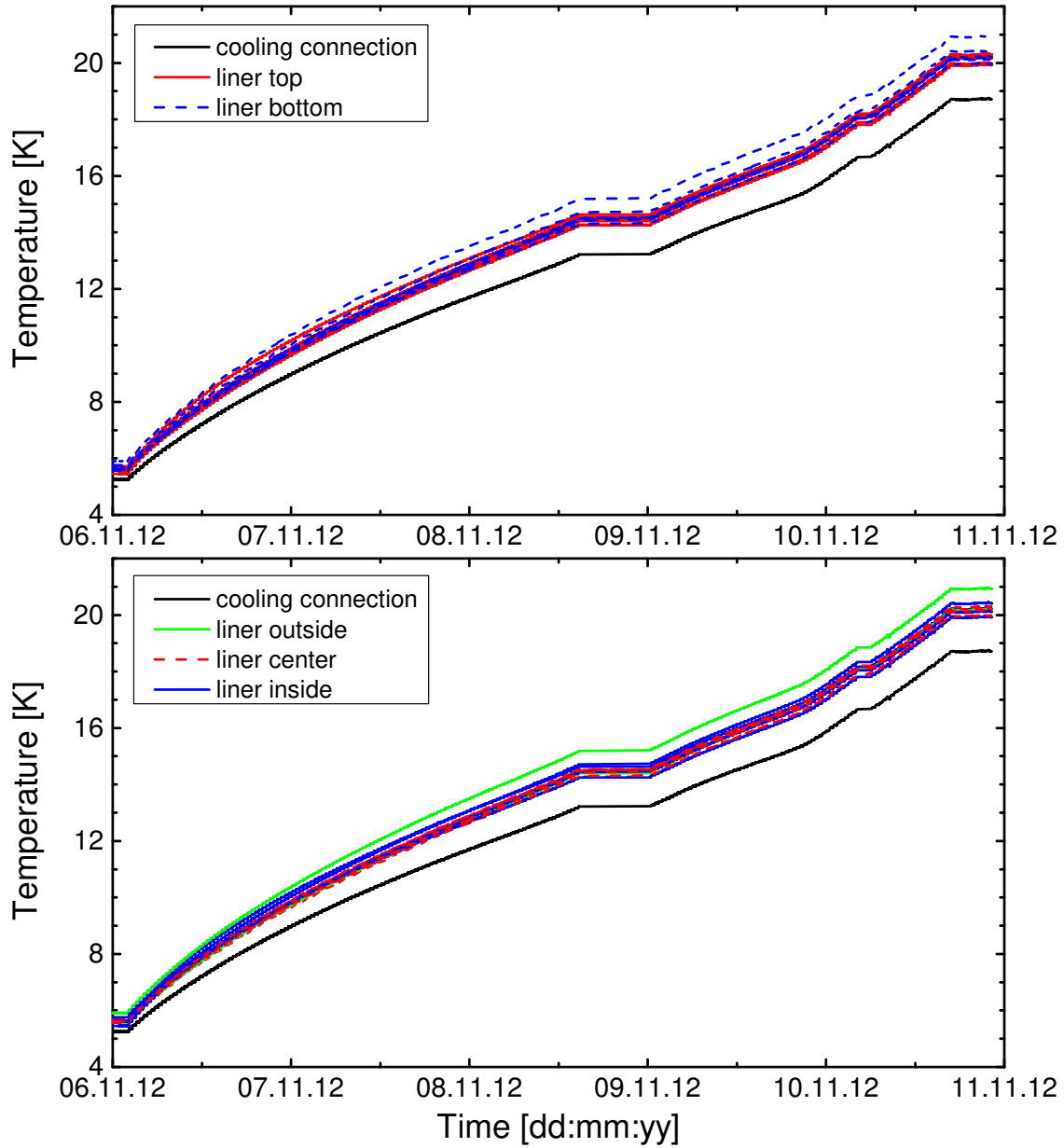


Figure 4.34: Temperature distribution on the liner during a power ramp on the liner heaters.

4.5.5 Heat transfer simulations

In order to investigate the possibility of specific heating patterns leading to the observed temperature distribution on the liner, heat transfer simulations were performed using the Finite Element Method (FEM). The full procedure includes the following steps:

- Generating a simplified 3D-model of the COLDDIAG liner, including the cooling connection to the cryocooler, in FreeCAD [47].
- Creating a mesh from the 3D-model with gmsh [48].
- Importing the mesh into Elmer [49].
- Creating the solver input file, which contains all settings and boundary conditions.
- Running the simulation.

For the material of the liner and the cooling connection copper with a RRR value of 100 is used. The temperature dependence of the thermal conductivity k and specific heat C is modeled with the following equations [50]:

$$\log k(T) = \frac{2.2154 - 0.88068 \cdot T^{0.5} + 0.29505 \cdot T - 0.04831 \cdot T^{1.5} + 0.003207 \cdot T^2}{1 - 0.47461 \cdot T^{0.5} + 0.13871 \cdot T - 0.02043 \cdot T^{1.5} + 0.001281 \cdot T^2} \quad (4.8)$$

$$\log C(T) = -1.91844 - 0.15973(\log T) + 8.61013(\log T)^2 - 18.996(\log T)^3 + 21.9661(\log T)^4 - 12.7328(\log T)^5 + 3.54322(\log T)^6 - 0.3797(\log T)^7 \quad (4.9)$$

The cryocooler is modeled as a boundary condition with a temperature dependent heat flux, using the cooling power h interpolated from the cryocooler load map [35]:

$$h(T) = \frac{4.51 \cdot 10^{-3} T^4}{1 + 2.10213 \cdot 10^{-4} T^4} \quad (4.10)$$

Figure 4.35 shows the resulting temperature distribution on the cold liner, when a 20 W heat source is put on the position of the temperature sensor showing the highest temperature in Figure 4.30. While the temperature at that position can be reproduced, the measured

temperature at the remaining sensors is much lower than in the simulation. The average measured temperature of 17.6 K is more than 2 K lower than in the simulation.

In the simulation the heat is applied from the outside of the liner to avoid meshing problems with the elliptical surface. In reality the heat is deposited at the inner surface of the liner. This leads to an overestimation of the temperature at the sensor, due to the path through copper of at least 1 mm. It shows that the measured temperature difference of 1 K or more between two neighbouring temperature sensors can not be created by heat deposited on the inner surface of the liner.

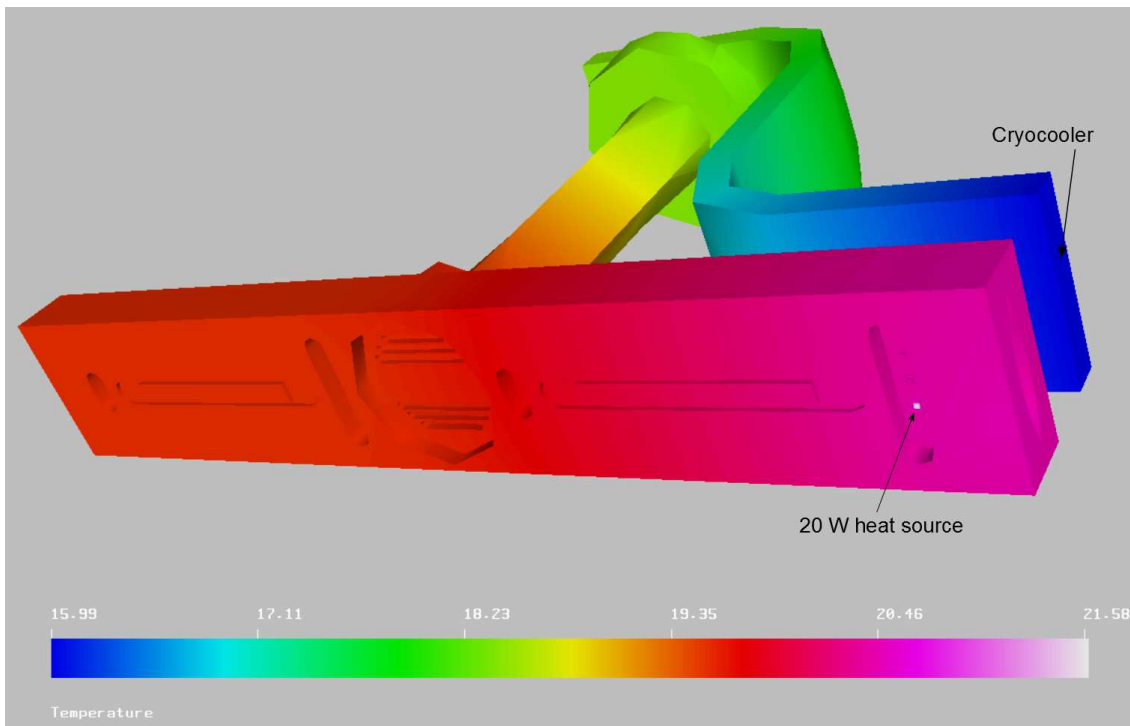


Figure 4.35: Simulation of the temperature distribution on the cold liner with a 20 W heat source at the position of a temperature sensor.

In a second simulation (Figure 4.36) the deposited heat is split in two parts, 15.5 W at the same position as in the first simulation and 4 W at the other end of the liner. The total heating power is chosen in such a way that the temperature at the cryocooler is reproduced. The lower total heating power and the distribution to both ends of the liner leads to a lower average liner temperature, but it is still about 1 K higher than in the measurement. The maximum temperature is reduced by 1.6 K and therefore the highest measured temperature can not be reproduced. Also the lowest temperature of 15 K close to the center of the liner does not fit to the simulation.

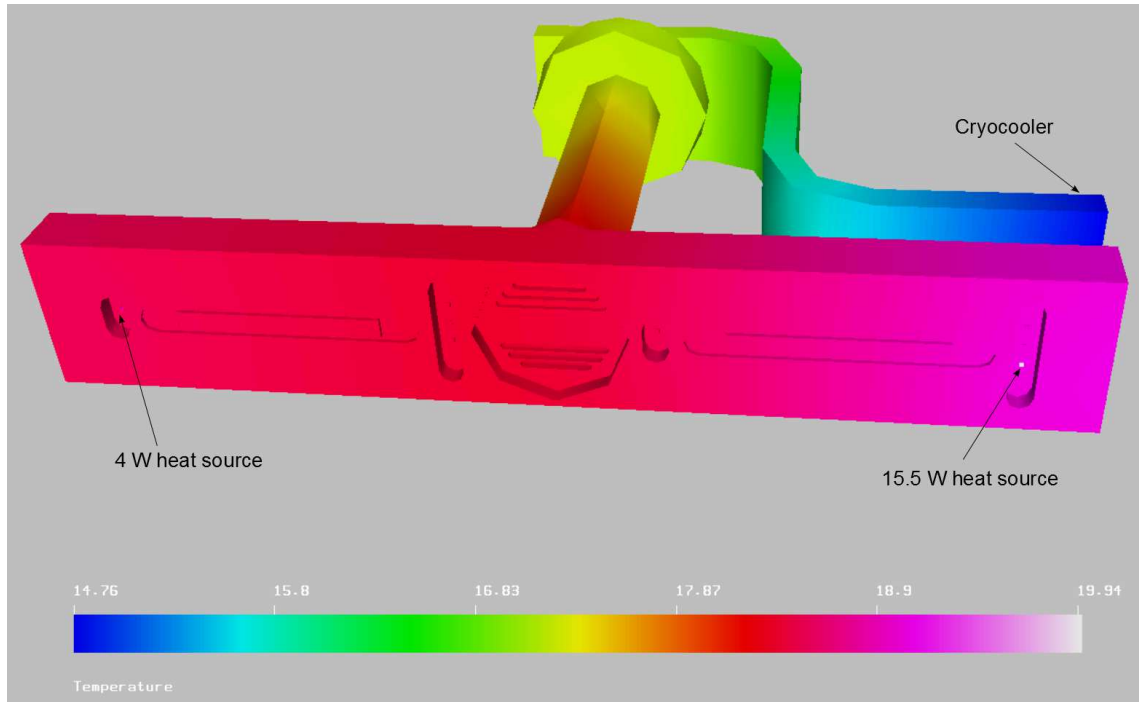


Figure 4.36: Simulation of the temperature distribution on the cold liner with a 15.5 W heat source at one end of the liner and a 4 W heat source at the other end.

In conclusion the simulations show that the observed temperature distribution on the cold liner can not be explained by heat deposited at the inner surface of the liner, because the good heat conductivity of copper prevents large enough temperature gradients over such small distances.

A possible explanation for the temperature differences is a difference in thermal contact between temperature sensor and liner. Additionally at high beam currents noise seems to affect the reading of the temperature sensors.

4.6 Summary

The measurements in this chapter show that the beam heat load to the cold liner is much larger than expected from resistive wall heating, but the dependence on the beam parameters is compatible with this effect. No correlation is observed between total pressure and beam heat load, and also the gas composition does not change with beam. Therefore direct synchrotron radiation can be excluded as a beam heat load source. Heating due to electron or ion bombardment could not be verified by the RFA measurements. The beam position only has a small effect on the beam heat load in extreme cases, and the observed temperature distribution on the liner cannot be explained by heat transfer simulations. In the next chapter the longitudinal beam coupling impedance is studied as another possible beam heat load source.

CHAPTER 5

Impedance measurements

In this chapter the impedance measurements on the COLDDIAG structure and on reference setups presented in Section 3.3 will be analysed, complementing the results of the beam heat load measurements taken at the Diamond Light Source in the previous chapter.

All measurements are done in the frequency range between 1 MHz and 14 GHz. The measurement procedure is not possible for frequencies above the beam pipe cut-off, which is at around 15 GHz for the elliptical cross section. Additionally the capacitive coupling of the inner conductor to the pin connectors, which is required to be weak for the measurement method, is getting stronger approaching the beam pipe cut-off. This effect has to be taken into account for the interpretation of the results above around 12 GHz.

The transmission S_{21} has been measured in a 16 MHz window centered at each resonance, giving a frequency resolution of 1 kHz. For each peak the transmission S_{21} and the frequency f_{res} at the maximum is determined, as well as the full width half maximum. From these values the real part of the longitudinal impedance $\text{Re}(Z)$ is calculated according to the procedure described in Section 2.3.4. For each device it is multiplied by its length, giving $\text{Re}(Z)$ in Ω as an impedance per device. Regarding the characteristic impedance Z_L , the chambers with an elliptic cross section are approximated by parallel plates, adding a factor 1.27 in the logarithm ($Z_L = 60 \Omega \cdot \ln(1.27 \cdot D/d)$).

The measurement accuracy of the impedance $\text{Re}(Z)$ is mainly affected by the accuracy of the transmission S_{21} , which is about 0.1 dB or 1 %, and by the determination of the resonance width, which is estimated conservatively to be 1 % as well. The center frequency of a resonance peak can be determined very precisely ($< 10^{-4}$) and is assumed to be without error in the analysis. The use of the parallel plate approximation for the elliptical cross section in the calculation of α_w can lead to a systematic error of the impedance, which is not considered for the calculation of the impedance error. Instead reference measurements

on a straight copper pipe and on an eroded ellipse are used to identify systematic errors. The impedance measurement on the eroded ellipse is used to measure the contribution from the skin effect for the elliptical cross section in COLDDIAG. The inner conductor is always made from a drawn copper rod with the diameter being precise to a few μm and is therefore assumed to be ideal.

Errors introduced by misalignment of the inner conductor are studied by shifting the inner conductor off-center (next section). Closely related to this are errors introduced by unequal coupling. In the measurement procedure the coupling of the inner conductor to the connector pins is assumed to be equally strong at both ends. At low frequencies this is the case, because the reflection is close to 0 dB. At higher frequencies around 10 GHz to 12 GHz a significant part of the power is transmitted through the device. As a result the reflection, and therefore the coupling, can become unequal.

The effect of unequal coupling on the measured impedance is studied in Figure 5.1. A measurement of the reflection at each end of the device (red and blue points) shows that the coupling is not equal for all frequencies. In a second measurement the reflection has been matched at each frequency by shifting the inner conductor towards the pin connector with the lower coupling (black points). While with unequal coupling the measured impedance is not always the same from both directions (S21 and S12), the measured impedance with equal coupling is independent of the direction, as it is expected for a passive device, and deviates up to 20% from the unmatched measurement.

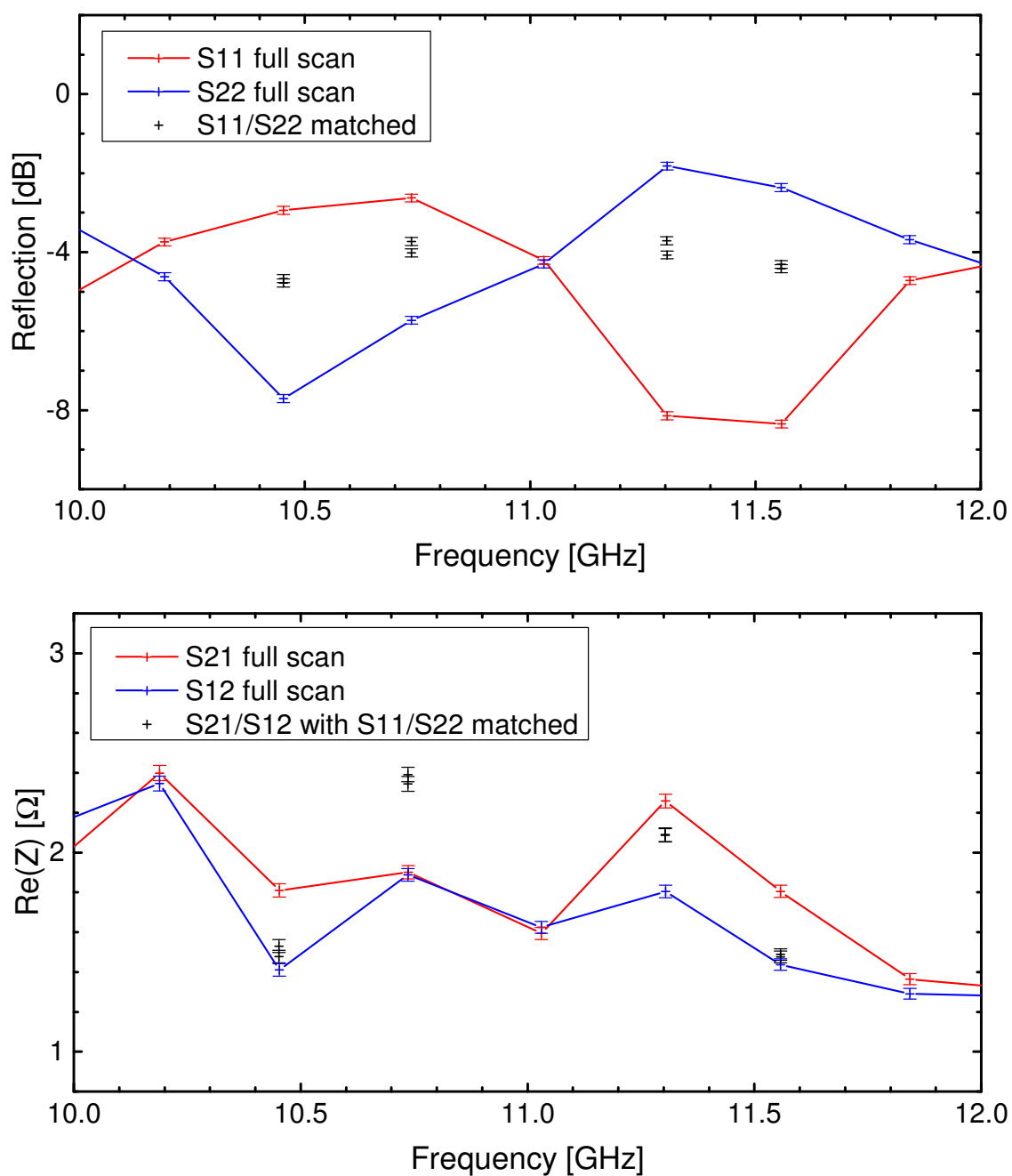


Figure 5.1: Impedance measurements at room temperature on the COLDDIAG cold part including thermal transitions. The black points represent single measurements with the reflection from both sides matched to the same value. Top: reflection at each transmission resonance. Bottom: real part of the longitudinal impedance at each transmission resonance.

5.1 Reference measurements

The first reference measurement is done on a 503 mm long drawn, straight copper pipe with an inner diameter of 10.26 mm, which typically has a small surface roughness of about 1 μm . Figure 5.2 shows the transmission S_{21} at the top, from which the impedance at the bottom is determined. The red points indicate the calculated impedance due to the skin effect on a surface with the resistivity of bulk copper ($1.7 \times 10^{-8} \Omega \text{m}$) and no surface roughness.

The measured impedance is enhanced by a factor of about 1.5 compared to the value predicted by the skin effect, which is calculated with Equations 2.19 and 2.21:

$$\text{Re}(Z)(f) = \frac{L}{\pi D} \cdot \sqrt{\pi \mu f \rho} \quad (5.1)$$

This can be attributed to the finite surface roughness in the sense that the surface corrugations can increase the effective length of the pipe by a factor of about 1.5 [19, 51]. Also a systematic error in α_w , which is not considered for the impedance error, can explain this discrepancy. At higher frequencies some additional contributions are present, presumably caused by capacitive coupling at the ends.

The second reference measurement is done on an eroded ellipse that resembles a COLDDIAG warm part without slots. The measured impedance is larger by a factor of about 2 compared to the impedance predicted for the skin effect in Equation 5.1 (see Figure 5.3). This can be explained by the larger surface roughness, because the eroded ellipse has been machined with a surface roughness of 3.6 μm compared to about 1 μm for the drawn copper pipe. The steep rise of the impedance above 13 GHz is similar in all measurements with an elliptical cross section, because the coupling increases stronger than for the round pipe, when approaching the cut-off frequency.

The effect of the inner conductor alignment on the measured impedance is shown in Figure 5.4 for the 270 mm long COLDDIAG warm part. A measurement with a centered inner conductor is compared to two cases of exaggerated misalignment. In one case the inner conductor is shifted along the beam axis by 0.5 mm, creating an uneven coupling to the pin connectors at the ends. In the other case the inner conductor is rotated in the horizontal plane, displacing its ends by 5 mm. For frequencies below 6 GHz the misalignment has no impact on the impedance measurement. At higher frequencies some deviations are visible. Above 12 GHz the three measurements are considerably different. The reason for this can be found in the different coupling. While the diagonal misalignment leads to a smaller coupling compared to the centered case, because of the greater distance to the pin, the displacement in beam direction leads to a larger coupling at one end and a smaller coupling at the other end, which do not compensate for each other.

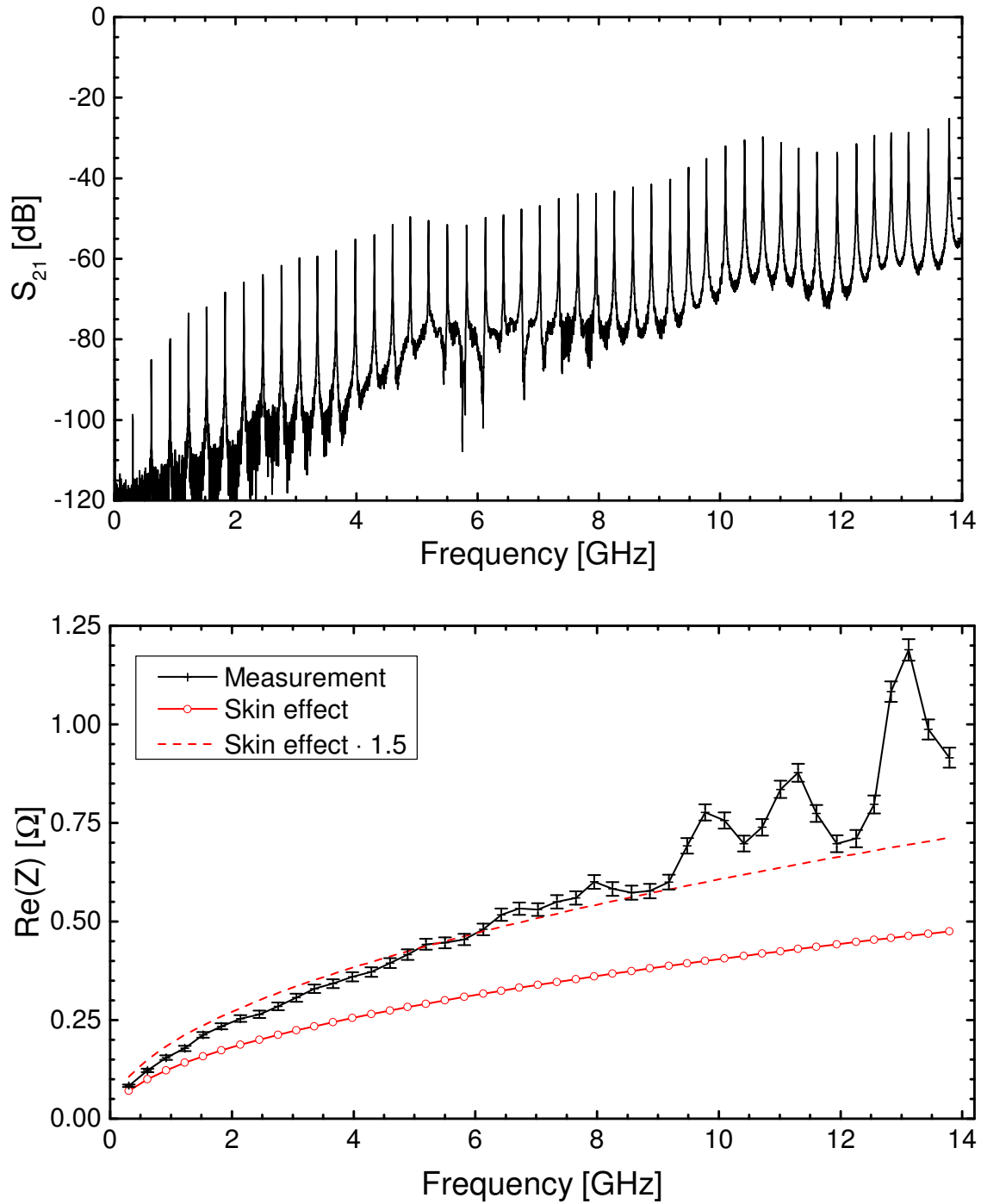


Figure 5.2: Impedance measurement at room temperature of a 503 mm long copper pipe with an inner diameter of 10.26 mm. Top: transmission measurement. Bottom: real part of the longitudinal impedance at each transmission resonance, compared to the impedance predicted from skin effect (solid line: ideal (Equation 5.1), dashed line: scaled by factor 1.5).

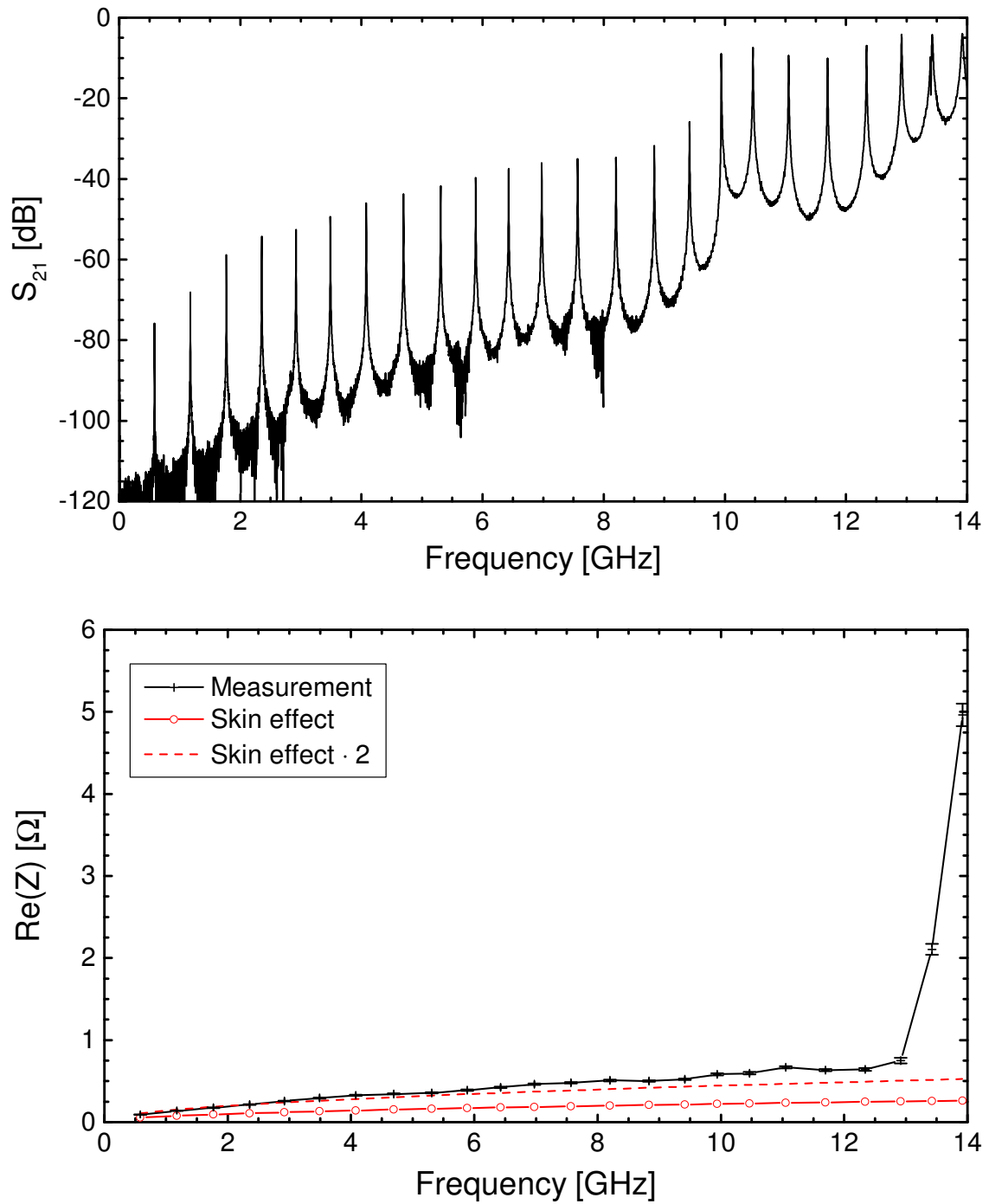


Figure 5.3: Impedance measurement at room temperature of a 270 mm long eroded ellipse with a major axis of 60 mm and a minor axis of 10 mm. Top: transmission measurement. Bottom: real part of the longitudinal impedance at each transmission resonance, compared to the impedance predicted from skin effect (solid line: ideal (Equation 5.1), dashed line: scaled by factor 2).

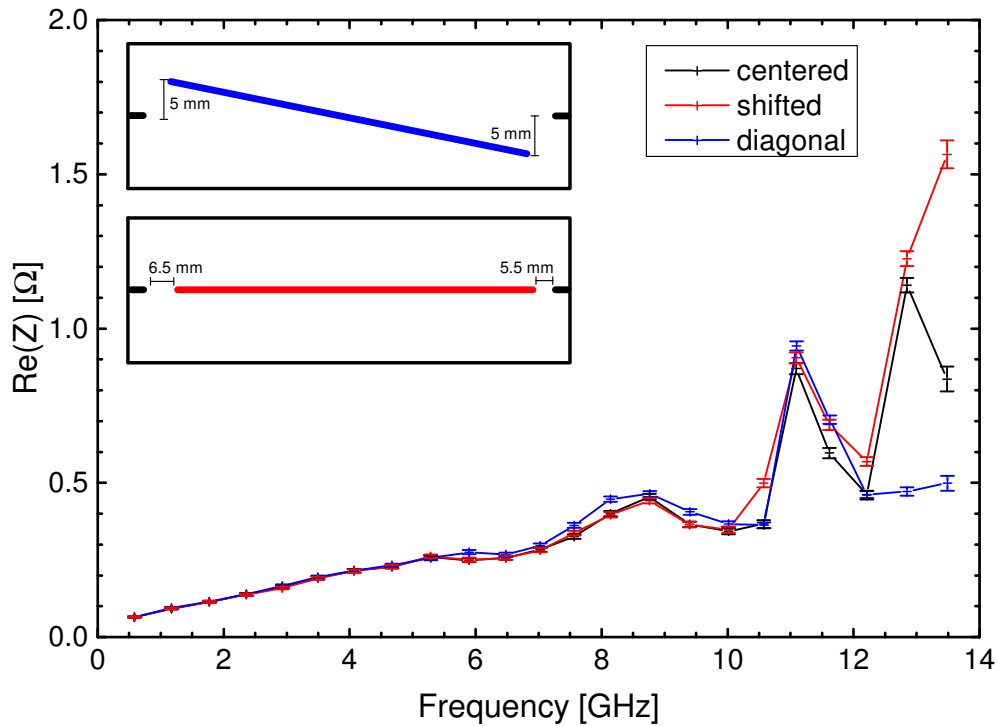


Figure 5.4: Effect of misalignment of the inner conductor on the measured impedance at room temperature of the 270 mm long COLDDIAG warm part. Inset: sketch of the two cases of misalignment in the horizontal plane, rotated (top) and shifted towards one pin (bottom).

5.2 COLDDIAG warm part

By measuring the impedance of a COLDDIAG warm part and comparing it to the eroded ellipse with the same length the effect of the diagnostic port slots on the impedance can be determined. Figure 5.5 shows the measured transmission of a COLDDIAG warm part and its corresponding impedance at the resonance peaks. Compared to the eroded ellipse the baseline of the impedance is closer to the skin effect, indicating a smaller surface roughness. This is in agreement with the surface roughness measurement performed on a test sample for the COLDDIAG liner [18], showing average peak heights of about $1\ \mu\text{m}$ with an average distance of $30\ \mu\text{m}$ to $40\ \mu\text{m}$ between them. At higher frequencies additional, irregular contributions to the impedance are visible. The centered measurement in the misalignment test in Figure 5.4 has also been done on the COLDDIAG warm part, but shows much less additional contributions at higher frequencies, indicating that the reproducibility of the measurement is limited, when the setup is reassembled, probably due to a change in the coupling. Additional contributions can in principle also be attributed to coupling to the diagnostic port slots. However, theoretical predictions do not foresee a measurable contribution from the slots [18] and the comparison with the measurement on the eroded ellipse does not show major differences below 10 GHz that can not be explained by the different surface roughness.

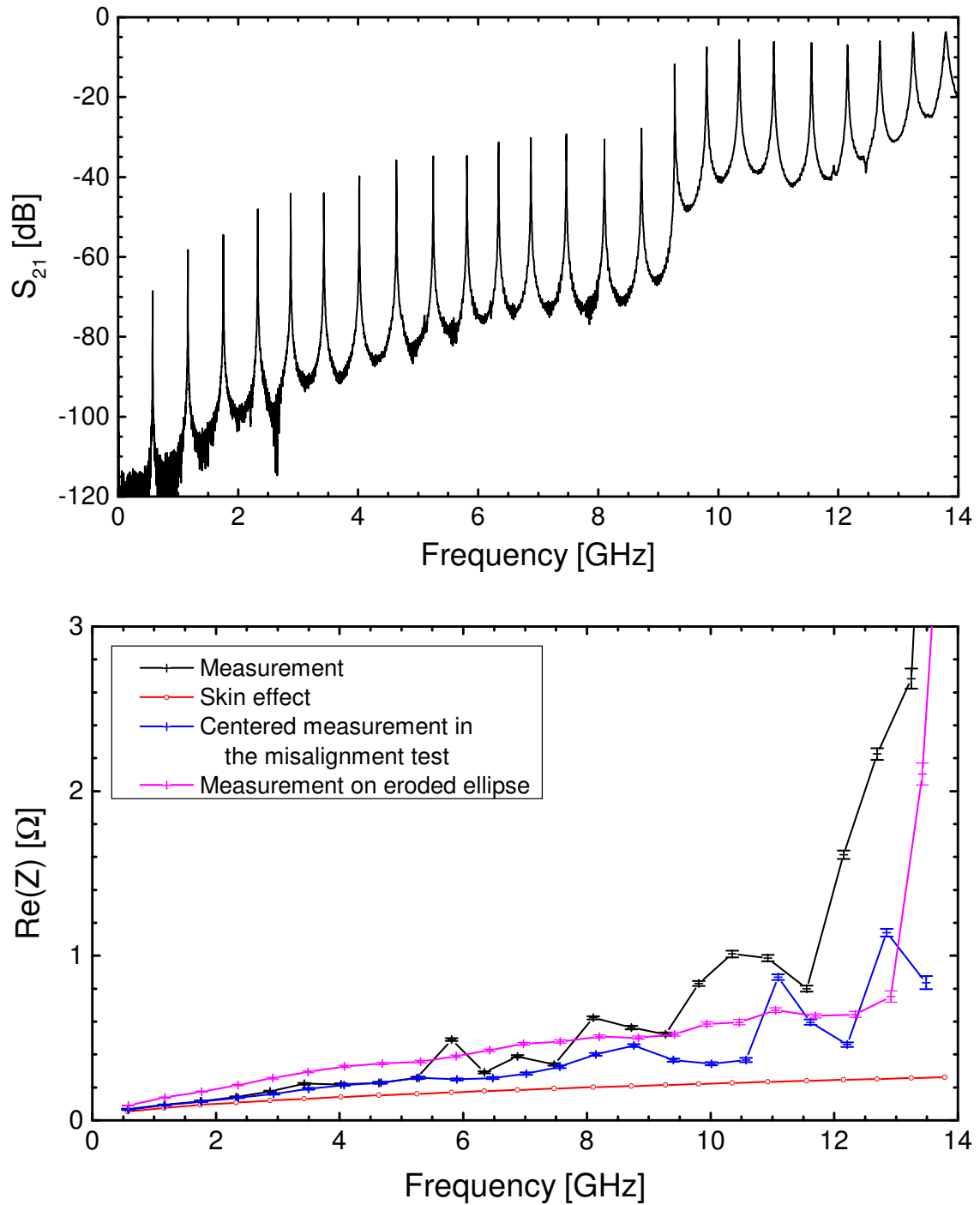


Figure 5.5: Impedance measurement at room temperature of the 270 mm long COLDDIAG warm section (elliptic cross section with a major axis of 60 mm and a minor axis of 10 mm). Top: transmission measurement. Bottom: real part of the longitudinal impedance at each transmission resonance, compared to the impedance predicted from skin effect, to the centered measurement in the misalignment test in Figure 5.4 and to the measurement on the eroded ellipse in Figure 5.3.

5.3 COLDDIAG cold part and thermal transitions

The cold section of COLDDIAG is studied in three steps, allowing to differentiate between the impedance generated by the liner itself, the thermal transitions from the cold liner to the 50 K shield and the finger bellows from the 50 K shield to the warm sections (see Figure 5.6).

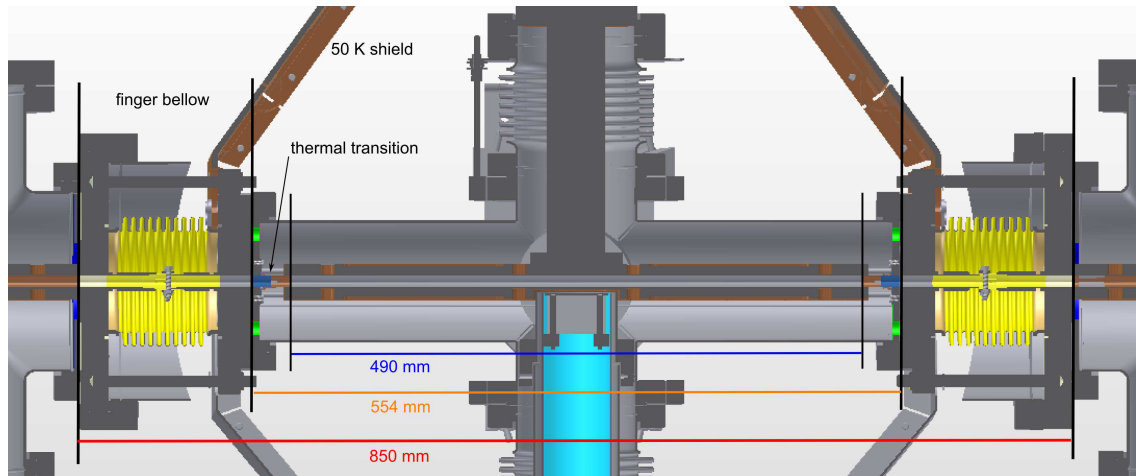


Figure 5.6: Cut through the COLDDIAG cold part. Indicated are the three sections on which impedance measurements were performed.

The first measurement is taken on the 850 mm long cold section including all transitions, i.e. measured between the two flanges connecting to the warm sections. Since the copper end plates were integrated into end flanges (see Section 3.3.4) for this measurement, the cryostat could be cooled down to 4 K. To be comparable to the beam heat load measurements the liner temperature was adjusted to 20 K using the heaters on the liner. The measured transmission and the corresponding impedance at the resonance peaks is shown in Figure 5.7 with the liner temperature set to 20 K and at room temperature.

In both cases the impedance shows resonances across the whole frequency range, large compared to the resistive wall impedance. Since the distance between two measurement points is fixed by the length of the device, it is not possible to determine the exact height and shape of the resonances. The measured impedance changes with liner temperature. At 20 K the peaks at lower frequencies are higher and the peaks at higher frequencies are lower. An explanation for this behaviour could be thermal shrinking, which slightly changes the geometry in the transitions and bellows, as well as the coupling to the pin connectors.

Because the finger bellows between the 50 K shield and the warm section are likely to be the main source of impedance and have no direct impact on the heat load to the cold section, a second measurement was done on the 554 mm long cold section between the two flanges connecting to the 50 K shield, including the liner of the cold section and the two thermal transitions between the liner and the 50 K shield. The measured transmission and the corresponding impedance at the resonance peaks is shown in Figure 5.8. This

measurement was taken only at room temperature, because of the missing bellows. The measured impedance shows a large peak at around 3 GHz, smaller peaks at 2 GHz, 5 GHz and 10 GHz and a broad contribution at high frequencies centered at around 9 GHz.

To confirm that the source of the impedance measured for the 554 mm long cold section are the thermal transitions, a third measurement was done on the 490 mm long liner in the cold section, which is basically a longer warm section (diagnostic port slots and elliptic cross section). The measured transmission and the corresponding impedance at the resonance peaks are shown in Figure 5.9.

In addition to the resistive wall impedance a small peak at 5 GHz and two larger peaks at 8 GHz and 11.5 GHz are visible. The resonances are larger than in the warm section. The resonance at 8 GHz seems to be relatively narrow and might have been missed in the measurement of the warm section, because of the different length of the sections.

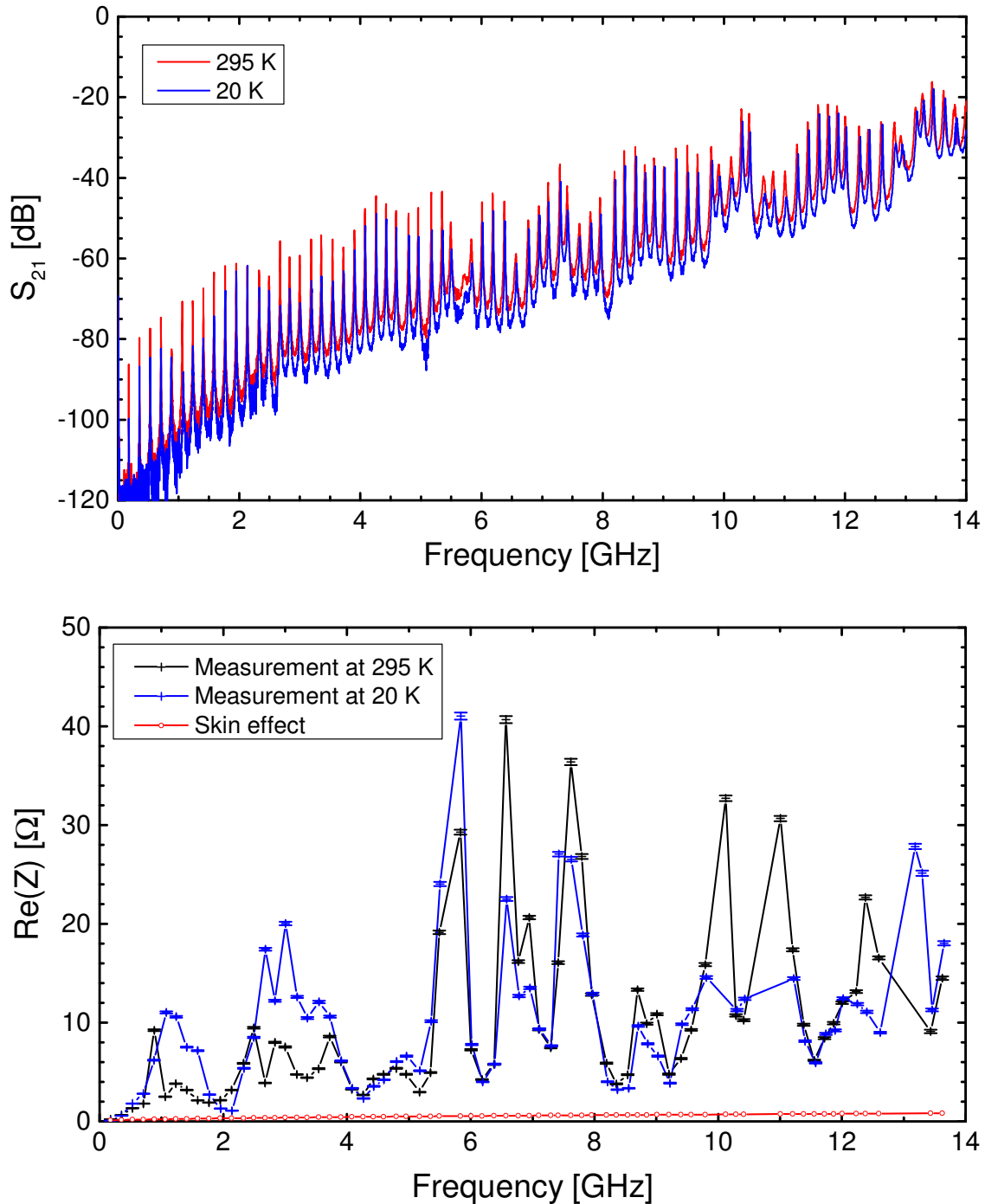


Figure 5.7: Impedance measurement of the 850 mm long COLDDIAG cold section including thermal transitions and bellows with the liner temperature at 20 K and at room temperature. Top: transmission measurement. Bottom: real part of the longitudinal impedance at each transmission resonance, compared to the impedance predicted from skin effect at room temperature for a continuous elliptical cross section with a major axis of 60 mm and a minor axis of 10 mm.

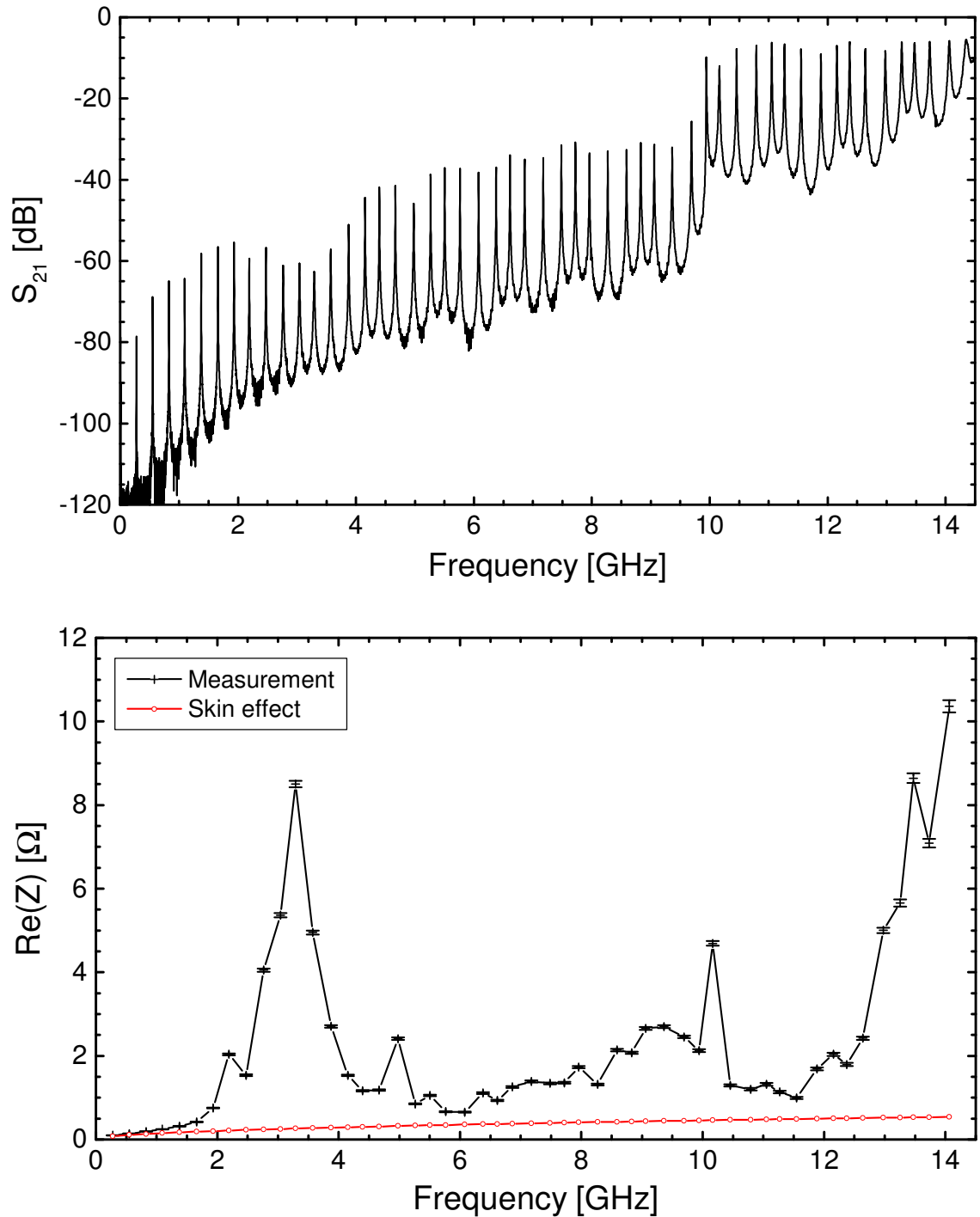


Figure 5.8: Impedance measurement of the 554 mm long COLDDIAG cold section including thermal transitions with the liner at room temperature. Top: transmission measurement. Bottom: real part of the longitudinal impedance at each transmission resonance, compared to the impedance predicted from skin effect at room temperature for a continuous elliptical cross section with a major axis of 60 mm and a minor axis of 10 mm.

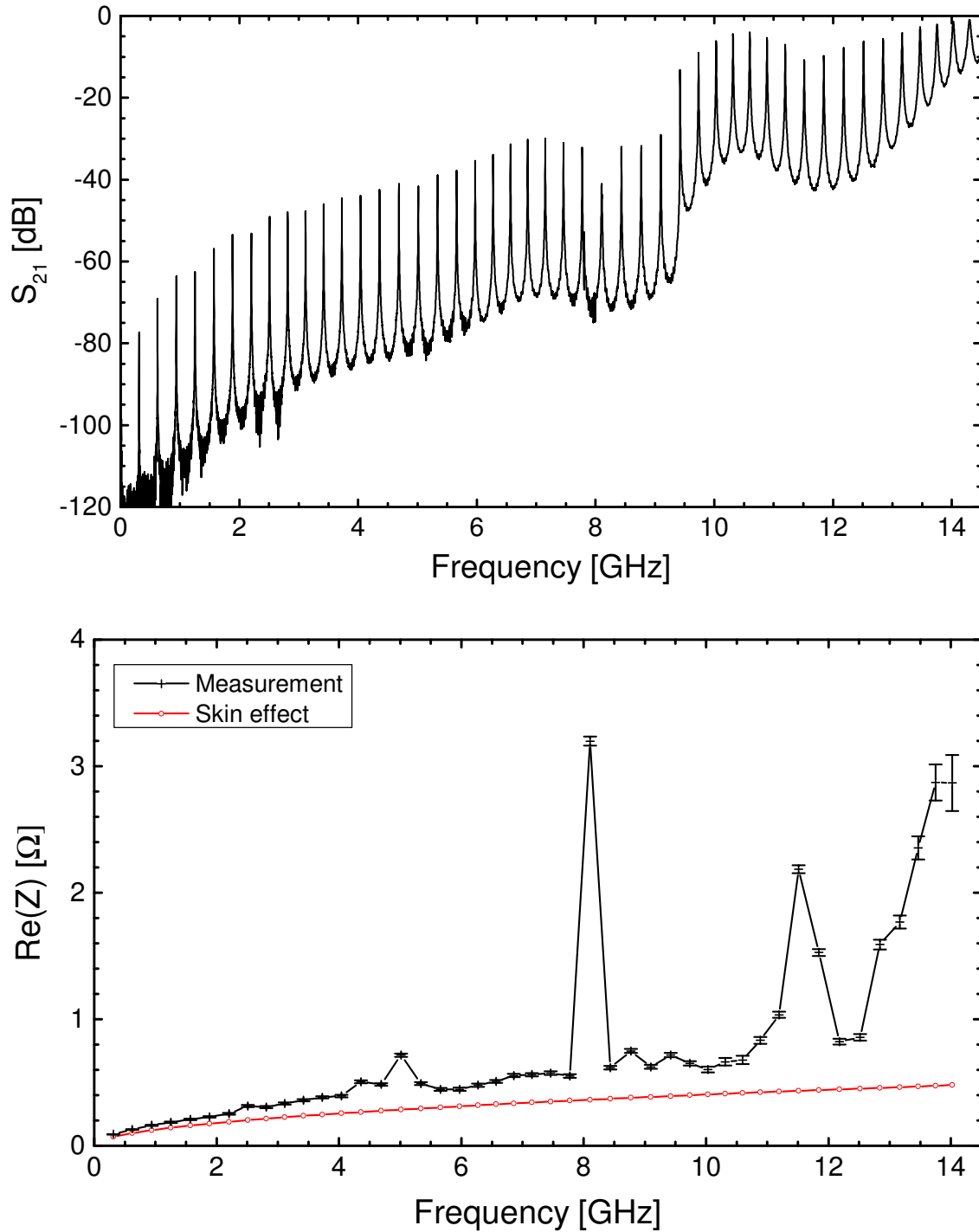


Figure 5.9: Impedance measurement of the 490 mm long COLDDIAG cold liner at room temperature. Top: transmission measurement. Bottom: real part of the longitudinal impedance at each transmission resonance, compared to the impedance predicted from skin effect at room temperature for a continuous elliptical cross section with a major axis of 60 mm and a minor axis of 10 mm.

5.4 RF power and beam heat load

Figure 5.10 shows a comparison between all impedance measurements, as well as the theoretical prediction for the impedance due to the skin effect in the 503 mm copper pipe and the single bunch spectrum for 300 mA in 900 bunches. The impedance axis is in a logarithmic scale to better visualise the differences at low impedances.

As stated before the rise of the impedance above 12 GHz for the measurements with an elliptical cross section is assumed to come from the increased coupling. However the effect on the power lost by the beam is limited, because the single bunch spectrum is already below 30 % of its maximum value for those frequencies.

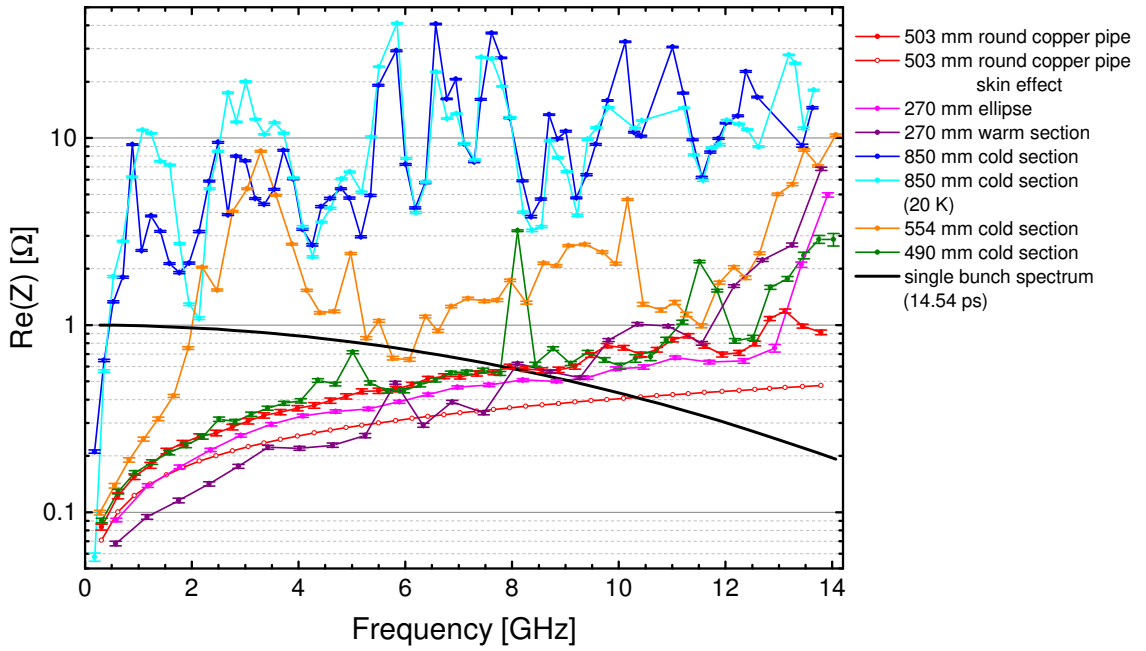


Figure 5.10: Comparison between the impedance measurements on COLDDIAG and on the reference chambers. The black line shows the normalised single bunch spectrum for 300 mA beam current in 900 bunches with a bunch duration of $\sigma_t = 14.54$ ps.

The measured impedance can be used to calculate the power P_{loss} that the electron beam loses according to Equation 2.10:

$$P_{loss} = \frac{I^2}{Nf_0} \cdot \frac{1}{\pi} \int_0^{f_c} \text{Re}(Z)(\omega) S^2(\omega) d\omega = \frac{I^2}{Nf_0} \cdot 2 \int_0^{f_c} \text{Re}(Z)(f) S^2(f) df \quad , \quad (5.2)$$

where f_c is the frequency up to which the impedance has been measured. Because in the original formula the upper limit of the integral is ∞ , the result gives a lower limit.

Additionally the fixed length of the measured devices allows only impedance measurements at specific frequencies, resulting in a finite frequency resolution of the measured impedance. For the integrated power loss this means that the interpolation between two consecutive measurement points leads to an integration error that is difficult to estimate, especially if sharp resonances are present.

The integrated power loss for the measured impedances in Figure 5.10 with a linear interpolation between the single measurement points is shown in Figure 5.11. For the filling pattern, the typical user operation mode at the Diamond Light Source (300 mA, 900 bunches, 14.54 ps bunch duration) is used. The measured beam heat load in the cold section for that filling pattern is $4.26 \text{ W} \pm 0.1 \text{ W}$ and indicated by the dashed red line. In Equation 5.2 the bunches are assumed to be equally spaced.

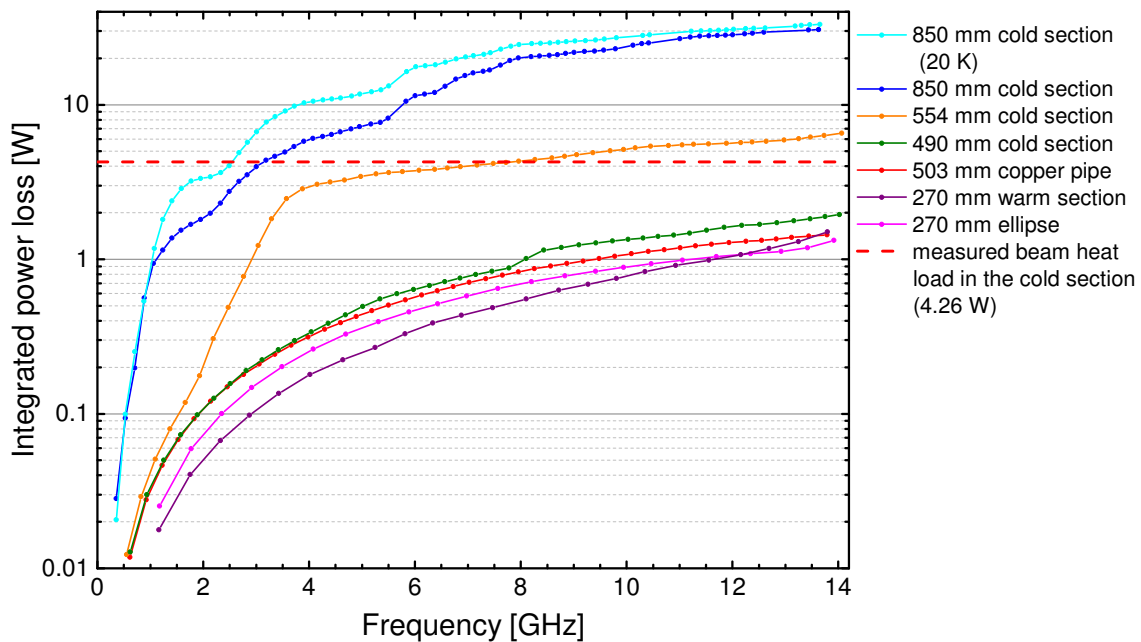


Figure 5.11: Integrated power loss for the impedances in Figure 5.10, assuming a 300 mA electron beam with 900 bunches and a bunch length of 14.54 ps.

The integrated power loss for the 850 mm cold section, including thermal transitions and finger bellows, is about 30 W. The part of this heat that is generated in the finger bellows is intercepted by the 50 K shield, which is connected to the first stage of the cryocooler. The remaining heat is taken by the second stage of the cryocooler.

The integrated power loss for the 554 mm cold section does not include the finger bellows and therefore only contains heat that is taken by the second stage of the cryocooler, equivalent to a hypothetical beam heat load measurement at room temperature, because the impedance was measured at room temperature. Considering the measured impedance up to 12 GHz (due to the coupling problems at higher frequencies) the power loss is about 5.6 W.

The integrated power loss for the 490 mm cold section (without thermal transitions) is

about 1.6 W and close to the reference measurement on the copper pipe. It can therefore be explained by the skin effect in combination with surface roughness. Since the impedance measurement was performed at room temperature, the integrated power loss in the cold device would be smaller than the measured value due to the lower resistivity of copper at cryogenic temperatures.

In conclusion the impedance measurements suggest that for standard user beam conditions at the Diamond Light Source about 4 W of beam heat load is generated in the thermal transitions between the 50 K shield and the cold liner, and less than 1 W is generated on the cold liner due to resistive wall heating. This is consistent with the measured beam heat load of $4.26 \text{ W} \pm 0.1 \text{ W}$ and the theoretical prediction for resistive wall heating on the cold liner of 0.36 W (assuming $RRR = 10$).

In the same way the measured impedance in Figure 5.8 can be used to calculate the expected beam heat load for other filling patterns by inserting the corresponding beam current, number of bunches and single bunch spectrum in Equation 5.2. In Figure 5.12 this is shown for filling patterns with 900 bunches and different bunch lengths and beam currents. Additionally the power loss has been corrected by the difference between resistive wall heating at room temperature and at cryogenic temperatures (blue points, assuming $RRR = 10$), in order to account for the temperature difference between impedance measurement at room temperature and beam heat load measurement at 20 K.

As a function of bunch length the corrected power loss is higher than the measured beam heat load for bunch lengths above 17 ps and lower for bunch lengths below 15 ps. An explanation for this behaviour is that for smaller bunch lengths the single bunch spectrum gives a larger contribution at high frequencies. Because the impedance is only considered up to 12 GHz, this leads to an underestimation of the power loss compared to larger bunch lengths, for which the neglected contribution above 12 GHz is smaller.

As a function of beam current the corrected power loss is in agreement with the measured beam heat load up to 200 mA. For higher beam currents the measured beam heat load is smaller than the one estimated by the corrected power loss. This deviation can be explained by the limited resolution of the measured impedance, because the linear interpolation between the single points of the impedance measurement can overestimate the actual impedance.

Besides the limited frequency resolution, the resonator method for impedance determination is very powerful for beam heat load investigations, as it allows measure small impedances in a reliable way. Considering the uncertainties in the determination of the power loss, the agreement between the impedance measurements and the beam heat load measurements with a maximum difference of 0.8 W is very good and offers an explanation of the observed beam heat load for the first time.

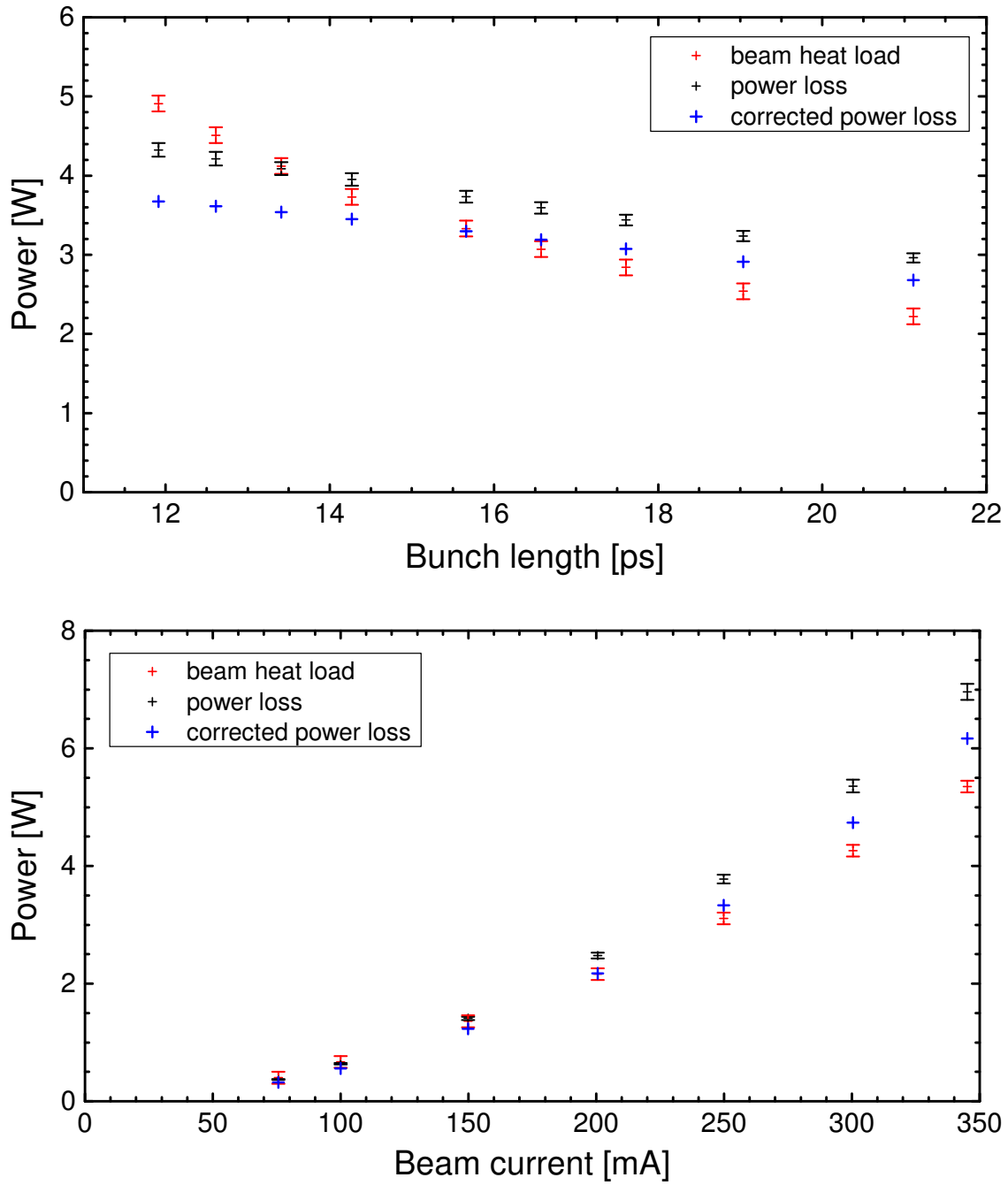


Figure 5.12: Comparison between calculated RF power loss due to the impedance up to 12 GHz in Figure 5.8 and measured beam heat load for 250 mA beam current and 900 bunches with different bunch lengths (top) and a beam current ramp with 900 bunches (bottom). The blue points are corrected by the difference between normal and anomalous skin effect ($RRR = 10$).

CHAPTER 6

Summary

The development of superconducting insertion devices is an important step towards increasing the performance of third and fourth generation synchrotron light sources. One of the limiting factors is the knowledge of the beam heat load to the cold vacuum chamber. In the past a much higher beam heat load than predicted from theory was observed in several devices. In order to precisely measure the beam heat load to a cold vacuum chamber and investigate the underlying mechanisms, COLDDIAG has been built. It is equipped with diagnostics to measure the beam heat load, the total pressure and residual gas content, as well as the total flux and energy spectrum of low energy charged particles hitting the chamber walls.

COLDDIAG was installed in the electron storage ring of the Diamond Light Source from September 2012 to August 2013. Within this thesis, measurements have been done for a wide range of machine parameters during that time. The measurement procedure has been optimised to allow for measurements at a constant liner temperature by implementing a PID control of the liner heaters, making it possible to measure the beam heat load at different liner temperatures. From the machine side it was possible to run with a wide variety of beam parameters, investigating the influence of bunch length, bunch spacing and bunch charge. The resulting data were analysed in detail after an offline calibration of the beam heat load measurements, that was necessary to calibrate the heat intake over the thermal transitions from the 50 K shield to the cold liner.

The beam heat load measured with COLDDIAG at the DLS is about one order of magnitude higher than expected from calculations of resistive wall heating and simulations of geometric impedances, that have been carried out on a full model of the COLDDIAG structure. At the same time the dependence on the beam parameters, especially the bunch length, suggests a combination of resistive wall heating and geometric impedance as the heat source. Heating from direct synchrotron radiation can be excluded due to the absence of a linear dependence of pressure and heat load on the beam current. Also no indication was found for electron multipacting or an influence from the cryosorbed gas layer on the

beam heat load, although a relatively high base pressure and geometrical dependencies limit the conclusiveness of these results.

The next step towards finding the source of the observed beam heat load were measurements of the real part of the longitudinal beam coupling impedance, which describes resistive losses due to geometric and resistive wall impedance. A wire measurement technique was applied and the resonator method was chosen in order to be sensitive to small impedances. Different parts of the COLDDIAG structure were transformed into a TEM resonator by introducing a centered inner conductor and closing the two ends with capacitive coupling. The transmission resonances could be used to measure the impedance at discrete frequencies and a comparison between the measurements allowed to locate impedance sources. While for the cold liner itself no significant contribution besides resistive wall impedance was found, the thermal transitions from the 50 K shield to the cold liner showed a large impedance mainly at around 3 GHz.

The heat load generated by this impedance is not taken into account by the calibration of the beam heat load measurement, since the calibration only considers heat generated at the warmer side of the transition and not at the transition itself. The accuracy of the impedance measurement is limited by the fact that the connectors for coupling into the resonator can not be included in the calibration of the network analyser. Moreover, the resonant method has the intrinsic drawback that the resolution of the impedance measurement is determined by the length of the structure. For the determination of the impedance of the cold liner it is not possible to resolve resonances sharper than $c/2L = 0.3$ GHz. But for a longer device, like a superconducting insertion device, the resolution improves. Even if this method can underestimate the geometrical and resistive wall impedance by missing sharp resonances, it has proven to be very powerful in the case of COLDDIAG and shows extremely good agreement with the beam heat load measurements. This is the first time that the beam heat load can be explained by theory.

These results lead to important implications for the cryogenic design of superconducting undulators. For direct beam heat load to the cold liner a conservative calculation of resistive wall heating is sufficient, taking into account the effect of surface roughness. Besides introducing heat from higher temperature regions, the thermal transitions can be the source of additional heat due to imperfections in the geometric design. In order to reduce the beam heat load to the cold liner, care has to be taken in the design of the thermal transitions. It is crucial to move them to the 50 K region at the warm side of the thermal shield in order to intercept the heat from steps and tapers before the cold section.

Bibliography

1. ELDER, F. R., A. M. GUREWITSCH, R. V. LANGMUIR, and H. C. POLLOCK: ‘Radiation from Electrons in a Synchrotron’. *Physical Review* (June 1947), vol. 71: pp. 829–830 (cit. on p. 1).
2. WALLEN, E. and G. LEBLANC: ‘Cryogenic system of the MAX-Wiggler’. *Cryogenics* (2004), vol. 44: pp. 879–893 (cit. on pp. 1, 50).
3. CASALBUONI, S. et al.: ‘Beam heat load and pressure rise in a cold vacuum chamber’. *Phys. Rev. ST Accel. Beams* (2007), vol. 10: p. 093202 (cit. on p. 1).
4. SCHOUTEN, J.C. and E.C.M. RIAL: ‘Electron Beam Heating and Operation of the Cryogenic Undulator and Superconducting Wiggles at Diamond’. *Proceedings of IPAC2011, San Sebastián, Spain* (cit. on p. 2).
5. IVANYUSHENKOV, Y. et al.: ‘Development and operating experience of a short-period superconducting undulator at the Advanced Photon Source’. *Physical Review Special Topics Accelerators and Beams* (Apr. 2015), vol. 18(4), 040703: p. 040703 (cit. on p. 2).
6. CASALBUONI, S. et al.: ‘Design of a Cold Vacuum Chamber for Diagnostics’. *Proceedings of EPAC08, Genoa, Italy* (cit. on pp. 2, 29).
7. GERSTL, S. et al.: ‘Factory Acceptance Test of COLDDIAG: a Cold Vacuum Chamber for Diagnostics’. *Proceedings of IPAC2011, San Sebastián, Spain* (cit. on pp. 2, 29).
8. CUI, J. et al.: ‘Development of a Cryogenic Calorimeter for Investigating Beam-Based Heat Load of Superconducting Undulators’. *Applied Superconductivity, IEEE Transactions on* (June 2014), vol. 24(3) (cit. on p. 2).
9. MOBILIO, S., F. BOSCHERINI, and C. MENEGHINI: *Synchrotron Radiation - Basics, Methods and Applications*. Springer Berlin Heidelberg, 2015 (cit. on pp. 3, 5).
10. WILLE, K.: *Physik der Teilchenbeschleuniger und Synchrotronstrahlungsquellen*. Teubner Stuttgart, 1996 (cit. on p. 3).
11. CLARKE, J.A.: *The Science and Technology of Undulators and Wigglers*. Oxford Science Publications, 2004 (cit. on pp. 6, 7).

12. CASALBUONI, S. et al.: ‘Test of Short Mockups for Optimization of Superconducting Undulator Coils’. *Applied Superconductivity, IEEE Transactions on* (June 2014), vol. 24(3) (cit. on p. 9).
13. ONUKI, H and P ELLEAUME: *Undulators, Wigglers and their Applications*. CRC Press, 2002 (cit. on p. 10).
14. FURMAN, M., H. LEE, and B. ZOTTER: ‘Energy Loss of Bunched Beams in RF Cavities’. (1986), vol. (SCC Central Design Group Lawrence Berkeley Laboratory) (cit. on p. 11).
15. WOLFRAM RESEARCH, INC.: *Wolfram Mathematica online integrator*. 2015. URL: <http://integrals.wolfram.com/index.jsp> (cit. on p. 13).
16. PALUMBO, L., V. G. VACCARO, and M. ZOBOV: ‘Wake Fields and Impedance’. *ArXiv Physics e-prints* (Sept. 2003), vol. (cit. on pp. 14, 17).
17. CST. URL: <http://www.cst.com/> (cit. on p. 15).
18. CASALBUONI, S, M MIGLIORATI, A MOSTACCI, L PALUMBO, and B SPATARO: ‘Beam heat load due to geometrical and resistive wall impedance in COLDDIAG’. *Journal of Instrumentation* (2012), vol. 7(11): P11008 (cit. on pp. 15, 18, 93).
19. CHOU, W and F RUGGIERO: *Anomalous Skin Effect and Resistive Wall Heating*. Tech. rep. LHC-Project-Note-2. Geneva: CERN, Aug. 1995 (cit. on pp. 16, 90).
20. DRUDE, P.: ‘Zur Elektronentheorie der Metalle’. *Annalen der Physik* (1900), vol. 306(3): pp. 566–613 (cit. on p. 16).
21. SAEZ DE JAUREGUI, D. et al.: ‘Characterization of Vacuum Chamber Samples for Superconducting Insertion Devices’. *Proceedings of IPAC2012, New Orleans, Louisiana, USA* (cit. on p. 17).
22. GRÖBNER, O: ‘Beam induced multipacting’. *Proceedings of PAC 1997* (cit. on p. 19).
23. BAGLIN, V and B JENNINGER: ‘Pressure and Heat Load in a LHC Type Cryogenic Vacuum System Subjected to Electron Cloud’. (July 2004), vol. (LHC-Project-Report-721. CERN-LHC-Project-Report-721): 16 p (cit. on p. 20).
24. WALLÉN, E.: ‘Adsorption isotherms of H₂ and mixtures of H₂, CH₄, CO, and CO₂ on copper plated stainless steel at 4.2 K’. *Journal of Vacuum Science & Technology A* (1996), vol. 14(5): pp. 2916–2929 (cit. on p. 20).
25. POZAR, DAVID M.: *Microwave Engineering*. 4th ed. Hoboken, NJ: Wiley, 2011 (cit. on p. 20).
26. CHAO, ALEXANDER WU and MAURY TIGNER: *Handbook of Accelerator Physics and Engineering*. Singapore: World Scientific, 1999 (cit. on pp. 21, 26).
27. BRAY, J.R. and L. ROY: ‘Measuring the unloaded, loaded, and external quality factors of one- and two-port resonators using scattering-parameter magnitudes at fractional power levels’. *Microwaves, Antennas and Propagation, IEE Proceedings* (Aug. 2004), vol. 151(4): pp. 345–350 (cit. on p. 22).

28. KROYER, T, FRIEDHELM CASPERS, and E GAXIOLA: *Longitudinal and Transverse Wire Measurements for the Evaluation of Impedance Reduction Measures on the MKE Extraction Kickers*. Tech. rep. AB-Note-2007-028. CERN-AB-Note-2007-028. Geneva: CERN, July 2007 (cit. on pp. 23, 39).
29. HAHN, H.: ‘Validity of coupling impedance bench measurements’. *Phys. Rev. ST Accel. Beams* (12 Dec. 2000), vol. 3: p. 122001 (cit. on p. 23).
30. MARTIN, IAN: *DLS machine*. 2015. URL: <http://www.diamond.ac.uk/Science/Machine.html> (visited on 05/21/2015) (cit. on p. 26).
31. REHM, G., A. MORGAN, and C. THOMAS: ‘Beam Diagnostics Systems for the Diamond Synchrotron Light Source’. *Proceedings of EPAC2004, Lucerne, Switzerland* (cit. on p. 26).
32. REHM, G.: ‘Beam Diagnostics at Diamond Light Source’. *1st DITANET school on Diagnostics, April 2009* (cit. on p. 26).
33. GERSTL, STEFAN: ‘A COLD Vacuum Chamber for Beam Heat Load DIAGNOSTICS (COLDDIAG)’. PhD thesis. Karlsruhe Institute of Technology, 2013 (cit. on pp. 29, 33, 66).
34. BAGLIN, V., I.R. COLLINS, and B. JENNINGER: ‘Performance of a cryogenic vacuum system (COLDEX) with an {LHC} type beam’. *Vacuum* (2004), vol. 73(2). Proceedings of the European Vacuum Congress Berlin 2003, 23-26 June 2003, featuring the 8th European Vacuum Conference, 2nd Annual Conference of the German Vacuum Society: pp. 201–206 (cit. on p. 30).
35. GROUP, SHI CRYOGENICS: *RDK-415D 4K Cryocooler Series*. 2015. URL: <http://www.shicryogenics.com/products/4k-cryocoolers/rdk-415d-4k-cryocooler-series/> (visited on 07/29/2015) (cit. on pp. 30, 84).
36. GERSTL, S., R. VOUTTA, S. CASALBUONI, A. W. GRAU, T. HOLUBEK, D. SAEZ de JAUREGUI, R. BARTOLINI, M. P. COX, E. C. LONGHI, G. REHM, J. C. SCHOUTEN, R. P. WALKER, G. SIKLER, M. MIGLIORATI, and B. SPATARO: ‘Cold vacuum chamber for diagnostics: Instrumentation and first results’. *Phys. Rev. ST Accel. Beams* (10 Oct. 2014), vol. 17: p. 103201 (cit. on pp. 32, 34).
37. LAKE SHORE CRYOTRONICS, INC. URL: <http://www.lakeshore.com/products/Cryogenic-Temperature-Sensors/Cernox/Models/Pages/Specifications.aspx> (visited on 10/20/2015) (cit. on p. 33).
38. ZIEGLER, J.G. and N.B. NICHOLS: ‘Optimum Settings for Automatic controllers’. *Transactions of the A.S.M.E.* (1942), vol. 64 (cit. on p. 35).
39. CASPERS, F.: ‘Beam Impedance Measurement by the Wire Method Using a Synthetic Pulse Technique’. *IEEE Trans. Nucl. Sci. NS-32* (1985), vol. 1914 (cit. on p. 39).
40. HAHN, H. and F. PEDERSEN: ‘ON COAXIAL WIRE MEASUREMENTS OF THE LONGITUDINAL COUPLING IMPEDANCE’. (1978), vol. (cit. on p. 39).

41. CASPERS, FRIEDHELM and T SCHOLZ: ‘Resonator method for impedance determination’. *Part. Accel.* (Apr. 1995), vol. 50(CERN-PS-95-09-AR): 125–132. 8 p (cit. on p. 39).
42. INSTRUMENTS, MKS. URL: <http://www.mksinst.com/docs/UR/423-specifications.aspx> (visited on 10/06/2015) (cit. on pp. 56, 57, 59, 60).
43. *PrismaPlus QMG 220 Operating Instructions*. Pfeiffer Vacuum GmbH, 2007 (cit. on p. 61).
44. BERNHARDT, K.: *Vacuum Technology Compendium*. Pfeiffer Vacuum GmbH, 2013 (cit. on p. 60).
45. BAGLIN, V.: ‘Cold / sticky system’. *CERN Accelerator School, Platja d’Aro, 2006* (cit. on p. 62).
46. INC., KEITHLEY INSTRUMENTS. URL: <http://www.keithley.de> (visited on 10/12/2015) (cit. on p. 67).
47. RIEGEL, J., W. MAYER, and Y. van HAVRE: *FreeCAD 0.14*. URL: <http://freecadweb.org/> (cit. on p. 84).
48. GEUZAINÉ, C. and J.-F. REMACLE: *gmsh 2.8.5*. URL: <http://geuz.org/gmsh/> (cit. on p. 84).
49. CSC - IT CENTER FOR SCIENCE LTD.: *Elmer*. URL: <https://www.csc.fi/web/elmer/> (cit. on p. 84).
50. NIST CRYOGENIC TECHNOLOGIES GROUP: *Material Properties: OFHC Copper (UNS C10100/C10200)*. URL: http://cryogenics.nist.gov/MPropsMAY/OFHC%20Copper/OFHC_Copper_rev1.htm (cit. on p. 84).
51. GOUDKET, P. et al.: ‘Surface Resistance RF Measurements of Materials used for Accelerator Vacuum Chambers’. *Proceedings of IPAC2015, Richmond, Virginia, USA* (cit. on p. 90).

Danksagung

Ich möchte mich bei allen bedanken, die zum Gelingen meiner Arbeit beigetragen haben. Mein besonderer Dank gilt hierbei:

- Prof. T. Baumbach für die Möglichkeit diese Arbeit an seinem Institut anzufertigen.
- Prof. A.-S. Müller für das Interesse an meiner Arbeit und die Übernahme des Korreferats.
- Sara für die freundliche Betreuung und die zahlreichen Diskussionen im Laufe der Arbeit.
- Stefan für die ausführliche Einarbeitung in England und die hervorragende Zusammenarbeit, bei der ich sehr viel gelernt habe.
- Matthew Cox and Richard Walker for supporting the COLDDIAG project at Diamond.
- Günther Rehm, Riccardo Bartolini and everyone else who contributed to the COLDDIAG meetings.
- The Diamond vacuum group for their help with the installation, deinstallation and any problems in between.
- Hugo, Sol and Andy for the excellent atmosphere in the office during my stay at Diamond.
- Bruno Spataro, Andrea Mostacci and Mauro Migliorati for the impedance calculations and useful discussions.
- Nicole und der Institutswerkstatt für die Spezialteile für meine Experimente.
- David und Andreas für ihr stets offenes Ohr für meine Fragen.

